THE DYNAMIC BIOMECHANICAL REGULATION OF MORPHOGENESIS

by

Lowell Taylor Edgar

A dissertation submitted to the faculty of
The University of Utah
in partial fulfillment of the requirements for the degree of

Doctor of Philosophy

Department of Bioengineering

The University of Utah

August 2015

The University of Utah Graduate School

STATEMENT OF DISSERTATION APPROVAL

The following faculty members served as the supervisory committee chair and members for the dissertation of **Lowell Taylor Edgar**.

Dates at right indicate the members' approval of the dissertation.

Jeffrey A. Weiss	, Chair	**2/17/2015** Date Approved
Vladimir Hlady	, Member	**2/17/2015** Date Approved
James E. Guilkey	, Member	**2/17/2015** Date Approved
Yan-Ting E. Shiu	, Member	**2/17/2015** Date Approved
Robert W. Hitchcock	, Member	**2/17/2015** Date Approved

The dissertation has also been approved by **Patrick A. Tresco**

Chair of the Department/School/College of **Bioengineering**

and by David B. Kieda, Dean of The Graduate School.

ABSTRACT

Angiogenesis is the process by which new blood vessels sprout from existing vessels, enabling new vascular elements to be added to an existing vasculature network. Mechanical interactions during angiogenesis, i.e., traction forces applied by neovessels and the corresponding deformation of the extracellular matrix (ECM), are important regulators of growth and neovascularization. However, the dynamic relationship between cell-generated forces, the deformation of the ECM, and the topology of the emerging vascular network are poorly understood. The goal of this research was to develop, implement, and validate a computational framework that simulates the dynamic mechanical interaction between angiogenic neovessels and the ECM. This dissertation presents a novel continuous-discrete finite element (FE) model with angiogenic growth coupled with matrix deformation. Angiogenesis was simulated using a discrete growth model. This model uses properties of the ECM, represented by a continuous FE mesh, to regulate angiogenic growth and branching and was capable of accurately predicting vascular morphometric data when simulating growth in various matrix conditions. To couple growth with matrix deformation, sprout forces were applied to the mesh and the corresponding deformation of the matrix was determined using the nonlinear FE software FEBio. This deformation was then used to update the ECM into the current configuration before calculating the next growth step. Data from

vascularized gel experiments were used to both calibrate mechanisms within the model during implementation and compare with computational simulations to assess the validity of the simulations. In simulations of experiments involving vascularized collagen gels subjected to various mechanical boundary constraints, this coupled framework accurately predicted gel contraction and microvessel alignment for each condition. The primary mechanism for alignment occurs as microvessels passively align while moving with the deformation of the surrounding matrix. These results demonstrate how biomechanical cellular activity at the microscale during morphogenic processes such as angiogenesis can influence the macroenvironment and induce patterns and organization. These methods provide a flexible computational platform to investigate the mechanisms by which the biomechanical interaction between cells and the ECM regulates the structure and composition of the emerging tissue during morphogenesis.

TABLE OF CONTENTS

ABSTRACT iii

ACKNOWLEDGEMENTS vii

CHAPTERS

1. INTRODUCTION 1

    1.1 Motivation 1
    1.2 Research Goals 3
    1.3 Chapter Summary 4
    1.4 References 4

2. BACKGROUND 8

    2.1 The Formation of Microvascular Networks 8
    2.2 Cell Culture Models of Angiogenesis 10
    2.3 Organ Culture Models of Angiogenesis 11
    2.4 Angiogenic Neovessels Remodel the ECM 12
    2.5 Effects of Mechanical Boundary Conditions on Vascular Alignment 17
    2.6 References 24

3. A COMPUTATIONAL MODEL OF IN VITRO ANGIOGENESIS BASED ON EXTRACELLULAR MATRIX FIBER ORIENTATION 33

    3.1 Abstract 33
    3.2 Introduction 34
    3.3 Methods 37
    3.4 Results 49
    3.5 Discussion 56
    3.6 References 63

4. EXTRACELLULAR MATRIX DENSITY REGULATES THE RATE OF NEOVESSEL GROWTH AND BRANCHING IN SPROUTING ANGIOGENESIS 67

4.1 Abstract..... 67
4.2 Introduction..... 68
4.3 Methods..... 70
4.4 Results..... 80
4.5 Discussion..... 87
4.6 References..... 98

5. A COUPLED MODEL OF NEOVESSEL GROWTH AND MATRIX MECHANICS DESCRIBES AND PREDICTS ANGIOGENESIS IN VITRO..... 104

5.1 Abstract..... 104
5.2 Introduction..... 105
5.3 Methods..... 109
5.4 Results..... 132
5.5 Discussion..... 141
5.6 References..... 149

6. DISCUSSION..... 154

6.1 Summary..... 154
6.2 Matrix Remodeling and the Mechanical Regulation of Angiogenesis..... 156
6.3 Live Two-Photon Imaging of Angiogenic Neovessels..... 158
6.4 Limitations and Future Work..... 161
6.5 Conclusion..... 165
6.6 References..... 165

ACKNOWLEDGEMENTS

I would like to acknowledge the numerous people for their involvement in my education including Dr. David Shreiber at Rutgers University, Dr. Paul Schueler at Raritan Valley Community College, Dr. Meng Deng at Ethicon Inc., and Dr. Rebecca Brannon at the University at Utah.

I would like to thank my advisor, Dr. Jeffrey Weiss, and the members of my dissertation advisory committee: Drs. Vladimir Hlady, Jim Guilkey, Yan-Ting Shiu, and Bob Hitchcock. Additionally, our collaborators Dr. Jay Hoying at the University of Louisville and Dr. Urs Utzinger at the University of Arizona have provided valuable insight and experience during this research. I would also like to acknowledge my numerous colleagues from the Musculoskeletal Research Laboratory who have been exceptional colleagues and friends including Dr. Corinne Henak, Steve Maas, Dr. Shawn Reese, and Dr. Clay Underwood.

Financial support for this work was provided by generous grants from the National Institute of Health: R01HL077683 and R01GM083925.

CHAPTER 1

INTRODUCTION

1.1 Motivation

Angiogenesis is the process by which new blood vessels sprout from existing blood vessels, enabling the addition of new vascular elements to an existing vasculature network. Angiogenesis is an important aspect associated with numerous issues and applications within medicine and bioengineering. Within the medical field, diseases including cancer and atherosclerosis involve uncontrolled blood vessel growth, while scarring and poor wound healing involve insufficient vessel growth [1-3]. Bioengineers are also concerned with angiogenesis as a means of promoting neovascularization of scaffolds for engineered tissue implants [4-6]. Therefore, there has been increasing research interest into the regulatory mechanisms behind angiogenesis, with the hope of developing new treatments and techniques to either promote or inhibit angiogenic outgrowth depending on the application. Angiogenesis is highly sensitive to both the chemical and mechanical microenvironment [1,7-10]. Although extensive research has been performed regarding the chemical regulation of angiogenesis, the mechanical factors that regulate angiogenesis remain poorly understood. In particular, very little is known about how the mechanical properties of the extracellular matrix (ECM) such as

structure, composition, and boundary conditions modulate angiogenic outgrowth.

There have been several efforts to provide *in vitro* environments that induce cells to assemble into tissue engineered devices capable of clinical use [6,11-17]. However, the size of these constructs has been limited to the scale of effective diffusive transport as cells within these constructs do not have access to a functional vasculature [4,5,18]. Successful neovascularization of engineered tissue implants requires that the topology of the new vascular network meets the specific perfusion and functional requirements for that tissue [19]. For example, the generation of proper vascular alignment is a critical step in tendon healing and repair [20] and functional innervation [21]. Therefore, the successful fabrication of complex 3D vasculatures within engineering tissue implants requires an understanding behind the factors regulating vascular morphogenesis and the knowledge to control these factors and direct growth towards the required vascular solution.

During angiogenesis, sprouting endothelial cells within the parent vessel take on an invasive phenotype, releasing proteolytic enzymes to degrade the basement membrane, thus allowing their expansion into the ECM. The motility, metabolism, proliferation and differentiation of anchorage-dependent cells such as endothelial cells and pericytes are highly regulated by mechanical stimuli received by cells via mechanotransduction through the ECM [22-29]. This causes angiogenic neovessels to respond to the mechanical properties of the ECM. However, neovessels remodel the ECM during growth through a combination of applied traction forces, proteolytic activity and generation of new cell-matrix adhesions, changing the properties that regulate growth. This creates a dynamic feedback loop in which angiogenesis is coupled with

deformation and remodeling of the matrix. This feedback loop is an example of the spatially and temporally complexity frequently seen in morphogenesis. Common experimental techniques often do not possess the spatial and temporal resolution to study the dynamic interaction between angiogenic neovessels and the ECM at the microscale as well as examine how these interactions integrate and generate organization and alignment under macroscale conditions such as boundary constraint. Therefore, computational modeling is often used to supplement experimental efforts when investigating morphogenesis.

1.2 Research Goals

This dissertation discusses my research efforts to investigate the role of cell-matrix mechanics during angiogenesis as neovessels respond to the mechanical properties of the ECM, as well as how cells dynamically apply traction and remodel matrix properties during growth. Computational simulations allow investigators to test and compare hypotheses in a systematic manner without performing the necessary experiments, which may be exceedingly difficult or impossible using available culture techniques. The goal of this research was to develop, implement, and validate a computational framework that simulates the dynamic mechanical interaction between angiogenic neovessels and the ECM in order to supplement and enhance the interpretation of our experimental efforts. In this novel framework, a growth model of angiogenic neovessels is coupled with the finite element method to solve for the deformation produced by cellular remodeling of the ECM and provide dynamic feedback back to the vessels during growth. This dissertation will demonstrate that this framework is

capable at accurately predicting vascular organization, topology, and alignment under changes in three matrix conditions: fibril alignment (Chapter 3), density (Chapter 4), and boundary conditions (Chapter 5).

1.3 Chapter Summary

Chapter 2 provides the necessary background in angiogenesis including current experimental and computational techniques. Chapter 3 presents the growth model, which uses ECM fibril orientation at the neovessel sprout to determine the direction of growth. In Chapter 4 the growth model is modified to regulate the rate of neovessel growth and branching relative to local matrix density. Matrix fibril orientation and density are properties of the matrix that change during culture as neovessels remodel the matrix. Chapter 5 covers the methods and implementation of the coupling between the growth model and the nonlinear finite element software FEBio. Chapters 3-5 each present validation of the modeling framework by comparing predictions to experimental results. Chapter 6 summarizes and discusses the results of the previous chapters, the role the findings play in the field of angiogenesis research, and the limitations and future work for the computational framework.

1.4 References

[1] Folkman, J. (1997) "Angiogenesis and angiogenesis inhibition: An overview," Exp Supp 79:1-8.

[2] Carmeliet, P. (2004) "Manipulating angiogenesis in medicine," J Int Med 255:538-61.

[3] Ellis, L.M., Rosen, L. and Gordon, M.S. (2006) "Overview of anti-VEGF therapy and angiogenesis. Part 1: Angiogenesis inhibition in solid tumor malignancies," Clinic Adv Hematol Oncol 4.

[4] Phelps, E.A. and Garcia, A.J. (2010) "Engineering more than a cell: Vascularization strategies in tissue engineering," Curr Opin Biotech 21:704-9.

[5] Novosel, E.C., Kleinhans, C. and Kluger, P.J. (2011) "Vascularization is the key challenge in tissue engineering," Adv Drug Deliv Rev 63:300-11.

[6] Bouhadir, K.H. and Mooney, D.J. (2001) "Promoting angiogenesis in engineered tissues," J Drug Target 9:397-406.

[7] Conway, E.M., Collen, D. and Carmeliet, P. (2001) "Molecular mechanisms of blood vessel growth," Cardiovasc Res 49:507-21.

[8] Ingber, D.E. (2002) "Mechanical signaling and the cellular response to extracellular matrix in angiogenesis and cardiovascular physiology," Circ Res 91:877-87.

[9] Li, S., Huang, N.F. and Hsu, S. (2005) "Mechanotransduction in endothelial cell migration," J Cell Biochem 96:1110-26.

[10] Shiu, Y.T., Weiss, J.A., Hoying, J.B., Iwamoto, M.N., Joung, I.S. and Quam, C.T. (2005) "The role of mechanical stresses in angiogenesis," Crit Rev Biomed Engng 33:431-510.

[11] Mann, B.K. and West, J.L. (2001) "Tissue engineering in the cardiovascular system: Progress toward a tissue engineered heart," Anat Rec 263:367-71.

[12] Garvin, J., Qi, J., Maloney, M. and Banes, A.J. (2003) "Novel system for engineering bioartificial tendons and application of mechanical load," Tissue Engng 9:967-79.

[13] Andreadis, S.T. (2004) "Gene transfer to epidermal stem cells: Implications for tissue engineering," Expert Opin Biol Ther 4:783-800.

[14] Hattori, K., Joraku, A., Miyagawa, T., Kawai, K., Oyasu, R. and Akaza, H. (2006) "Bladder reconstruction using a collagen patch prefabricated within the omentum," Int J Urol 13:529-37.

[15] Yamamoto, Y., Ito, A., Kato, M., Kawabe, Y., Shimizu, K., Fujita, H., Nagamori, E. and Kamihira, M. (2009) "Preparation of artificial skeletal muscle tissues by a magnetic force-based tissue engineering technique," J Biosci Bioeng 108:538-43.

[16] Yang, D., Guo, T., Nie, C. and Morris, S.F. (2009) "Tissue-engineered blood vessel graft produced by self-derived cells and allogenic acellular matrix:A functional performance and histologic study," Ann Plast Surg 62:297-303.

[17] Evers, R., Khait, L. and Birla, R.K. (2011) "Fabrication of functional cardiac, skeletal, and smooth muscle pumps in vitro," Artif Organs 35:69-74.

[18] Obradovic, B., Carrier, R.L., Vunjak-Novakovic, G. and Freed, L.E. (1999) "Gas exchange is essential for bioreactor cultivation of tissue engineered cartilage," Biotechnol Bioeng 63:197-205.

[19] Pries, A.R. and Secomb, T.W. (2005) "Control of blood vessel structure: Insights from theoretical models," Am J Physiol Heart Circ Physiol 288:H1010-5.

[20] James, R., Kesturu, G., Balian, G. and Chhabra, A.B. (2008) "Tendon: Biology, biomechanics, repair, growth factors, and evolving treatment options," J Hand Surg Am 33:102-12.

[21] Larrivee, B., Freitas, C., Suchting, S., Brunet, I. and Eichmann, A. (2009) "Guidance of vascular development: Lessons from the nervous system," Circ Res 104:428-41.

[22] Ives, C.L., Eskin, S.G. and McIntire, L.V. (1986) "Mechanical effects on endothelial cell morphology: In vitro assessment," In Vitro Cell Develop Biol 22:500-7.

[23] Carosi, J.A., Eskin, S.G. and McIntire, L.V. (1992) "Cyclical strain effects on production of vasoactive materials in cultured endothelial cells," J Cell Physiol 151:29-36.

[24] Patrick, C.W., Jr. and McIntire, L.V. (1995) "Shear stress and cyclic strain modulation of gene expression in vascular endothelial cells," Blood Purif 13:112-24.

[25] Chien, S., Li, S. and Shyy, Y.J. (1998) "Effects of mechanical forces on signal transduction and gene expression in endothelial cells," Hypertension 31:162-9.

[26] Vernon, R.B. and Sage, E.H. (1999) "A novel, quantitative model for study of endothelial cell migration and sprout formation within three-dimensional collagen matrices," Microvasc Res 57:118-33.

[27] Deroanne, C.F., Lapiere, C.M. and Nusgens, B.V. (2001) "In vitro tubulogenesis of endothelial cells by relaxation of the coupling extracellular matrix-cytoskeleton," Cardiovasc Res 49:647-58.

[28] McCormick, S.M., Frye, S.R., Eskin, S.G., Teng, C.L., Lu, C.M., Russell, C.G., Chittur, K.K. and McIntire, L.V. (2003) "Microarray analysis of shear stressed endothelial cells," Biorheology 40:5-11.

[29] Joung, I.S., Iwamoto, M.N., Shiu, Y.T. and Quam, C.T. (2006) "Cyclic strain modulates tubulogenesis of endothelial cells in a 3D tissue culture model," Microvasc Res 71:1-11.

CHAPTER 2

BACKGROUND

2.1 The Formation of Microvascular Networks

Angiogenesis refers to the process by which new blood vessels sprout and grow from existing vasculature. The function of vascular networks is to facilitate the delivery of oxygen and other nutrients and the removal of wastes. The three primary types of blood vessels are arteries, veins, and capillaries. Capillaries consist of an endothelium and a single layer of stromal cells (pericytes) and provide the diffusion gradients that cells require for transport. Networks of capillaries are often referred to as microcirculation or microvasculature. In both embryonic and adult tissue, new blood vessels are generated from pre-existing vasculature via neovessel sprouting [1-3]. Sprouting angiogenesis involves the following events: 1) degradation of basement membrane and detachment and migration of pericytes into the ECM, 2) migration of vascular endothelial cells into the extracellular matrix (ECM) and formation of the neovessel sprout, 3) elongation of the sprout as endothelial cells lagging behind tip cells proliferation. Neovessel maturation involves the formation of lumen, recruitment of pericytes within the ECM to the surface of the neovessels, and formation of a new basement membrane. The formation of a functional neovascularization requires

neovessels to form new vascular connection by fusing with other vessels (i.e., anastomosis) which increases the interconnectivity of the vascular network.

The ECM facilitates signaling across the extracellular space and provides both mechanical and biochemical regulatory signaling for cells [4-7]. A variety of stimuli from the ECM integrate to influence angiogenic growth during vascular morphogenesis. Many pro-angiogenic factors such as vascular endothelial growth factor (VEGF), fibroblast growth factor (FGF), and transforming growth factor-β (TGF-β) are embedded within the ECM and can be released about ECM degradation and remodeling [8-10]. Additionally, angiogenic vascular cells mechanically interact with the ECM through the secretion of proteolytic enzymes, generation of new integrin binding, application of traction forces and migration. The influence that individual neovessel sprouts exert on the matrix can cause signaling in other neovessels via mechanotransduction. *In vitro* models of angiogenesis are often used to systematically isolate and study individual components within this complex assortment of factors, offering a more controlled environment compared to *in vivo* models.

This chapter discusses common *in vitro* models of angiogenesis and provides background on recent experimental findings related to this dissertation. Section 2.2 discusses cell culture models of angiogenesis, while Section 2.3 discusses organ culture models. Section 2.4 outlines the changes angiogenic sprouts cause within the matrix during growth and remodeling. Section 2.5 discusses the findings demonstrating the regulation of vascular organization and alignment via mechanical boundary conditions during angiogenesis.

2.2 Cell Culture Models of Angiogenesis

The majority of experimental investigations into angiogenesis and vascular assembly involved cultures of isolated vascular or prevascular cells. The simplest models used in these studies were endothelial cell migration assays [11-24]. During angiogenesis, endothelial cells within neovessel sprouts migrate into the ECM. These experiments involved single endothelial cells migrating on an ECM surface. This model is commonly used in the study of chemotaxis during migration. An increase in overall cell motility can be an indication of increased neovessel invasion, which is a component of angiogenic activity. Other studies into the regulation of angiogenesis have utilized endothelial cell differentiation assays [25-36]. In these experiments, endothelial cells are plated onto or into a matrix such as collagen which stimulates the migration, differentiation, and formation of tubule structures that resemble neovessels. These assays, also referred to as tubulogenesis assays, involve endothelial cells assembling into vessel-like structures rather than neovessel sprouting. The formation of tubules *in vitro* depends on numbers factors including cell density, matrix composition and density, and soluble growth factors.

Capillary sprouting assays are similar to tubulogenesis assays but in these experiments tubules sprout from an endothelial monolayer and offer a more realistic representation of angiogenesis *in vivo*. A common approach is to culture vascular cells on the surface of microcarrier beads embedded within an ECM environment that promotes assembly and sprouting into capillary-like structures such as collagen, fibrin, or Matrigel [37-50]. In these cultures, vascular cells grow out as chains from the bead surface into the ECM. These cultures almost always involve vascular endothelial cells,

such as HUVECs (human umbilical vascular endothelial cells), and some experiments included vascular smooth muscle cells and pericytes. These experiments have provided useful insight into the regulation of capillary sprouting by growth factors [37,50], cell-cell interactions [38,42,48], ECM composition and density [39,41,43,46], and matrix proteolysis through MMPs (matrix metalloproteinases) [40,44,49]. Although useful *in vitro* assays of angiogenesis, these isolated cell systems lack the multicellular organization and signaling found in microvessels *in vivo*. For this reason, many investigators have turned to systems that involve isolated vessels rather than cells to study angiogenesis.

2.3 Organ Culture Models of Angiogenesis

While cell culture models of angiogenesis are useful models for studying angiogenic outgrowth and capillary sprouting, vascular cells in these models do not form new vascular connections and do not offer insight into the morphogenesis of vascular networks. Isolated vessel systems utilize an organ culture of native vascular elements rather than isolated cells. These models involve the migration of endothelial cells and pericytes from neovessel sprouts that form at the excised ends of parent vessel segments. In past studies, parent vessel fragments have been obtained from macrovessels, such as the aortic ring [51-59] or inferior vena cava [60], or microvessels from epididymal fat pads [61-73]. Numerous studies investigating the mechanical regulation of sprouting angiogenesis have been performed using organ cultures of microvessel fragments seeded within 3D collagen gels [64,65,69-73]. In these experiments, parent vessel fragments contain associated perivascular cells and retain

their basement membrane after initial harvest and seeding. Sprouts elongate as patent tubes, branching and fusing with other vessels, and forming a new vascular network that ultimately fills the construct. Neovessel constructs form a functional vascular tree when implanted, rapidly inosculating with the recipient host circulation after implantation and carrying blood [74].

The methodology for creating these cultures was developed by Hoying et al. [61]. Rat microvessel fragments were isolated from minced rat epididymal fat pads and suspended in liquid type-I collagen. The collagen solution was poured into custom rectangular Teflon molds prior to polymerization. In certain experiments, a sterilized stainless steel mesh was inserted into the gel prior to polymerization to constrain displacement during growth. Microvessels were cultured in serum-free growth media. Neovessel sprouting typically began around Day 3, and well-established vascular networks formed by Day 6 (Figure 2.1). On the sixth day of culture, the constructs were fixed and endothelial cells were labeled and imaged using confocal microscopy. Volumetric datasets were processed and skeletonized and morphometric data describing the vascular network was collected using a custom software application. In some studies, confocal reflection microscopy was performed to visualize collagen fibril orientation within the construct.

2.4 Angiogenic Neovessels Remodel the ECM

Angiogenic neovessels within these organ cultures extensively remodel the ECM [64,75]. Neovessel sprouts from initial microvessel fragments extend into the matrix, applying traction and contracting the matrix inward. By Day 10 of culture, the cross-

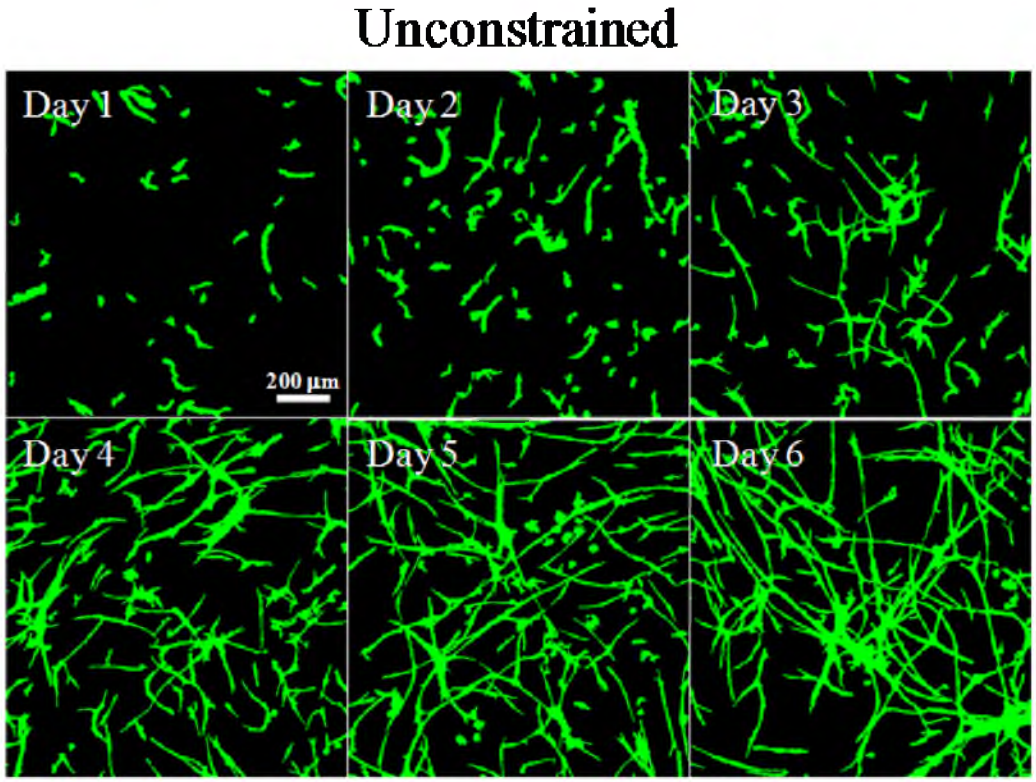

Figure 2.1: Angiogenic growth within an unconstrained vascularized construct, showing images of different cultures at different time points of growth after initial seeding. Unconstrained gels were free-floating and allowed to contract in all directions. Neovessel sprouting typically began at Day 3 of culture and well-established vascular networks with no preferred orientation formed by Day 6. Scale bar 200 µm.

sectional area of rectangular vascularized constructs reached ~20% of avascular control gels (Figure 2.2 A). The combined effects of matrilysis, cell adhesion, and the contraction and reorientation of ECM fibrils resulted in drastic changes to the material properties of the constructs. mRNA expression levels for MMPs were increased at Day 6 of growth compared to Day 0 (Figure 2.2 B), and this increased proteolytic activity coincided with a decrease in the dynamic stiffness of the construct (Figure 2.2 C). The angiogenic phenotype in endothelial cells is marked by increased proteolytic activity, and a primary function of MMPs is collagen cleavage, a prerequisite for endothelial cells invasion and angiogenesis [76,77]. However, by Day 10, the dynamic stiffness was increased compared to the stiffness of initial cultures, even though proteolytic mRNA expression remained high (Figure 2.2 B, C). As neovessels applied traction and contracted the matrix, the cells compacted the collagen fibrils, condensing and reorienting fibrils toward the neovessel tip (Figure 2.3 A). This contraction resulted in exudation of water from the matrix and increased fibril density, increasing the stiffness of the vascularized constructs. Additionally, mRNA expression for matrix molecules that promote the angiogenic phenotype such as fibronectin (FN), decorin (DCN), and tenascin C (TNC) increased during growth [78-83], while levels of the angiogenesis-inhibiting molecule hyaluronan (HAS) decreased (Figure 2.3 B) [84]. The creation of new cell-matrix adhesions through these matrix molecules likely contributed to the increased stiffness in the constructs. Neovessel and ECM fibril alignment induced by cell-generated contraction likely contributes to this stiffness increase as well. In summary, these experiments demonstrated that the process of angiogenic growth causes dramatic changes in the material properties of the ECM, suggesting a finely regulated

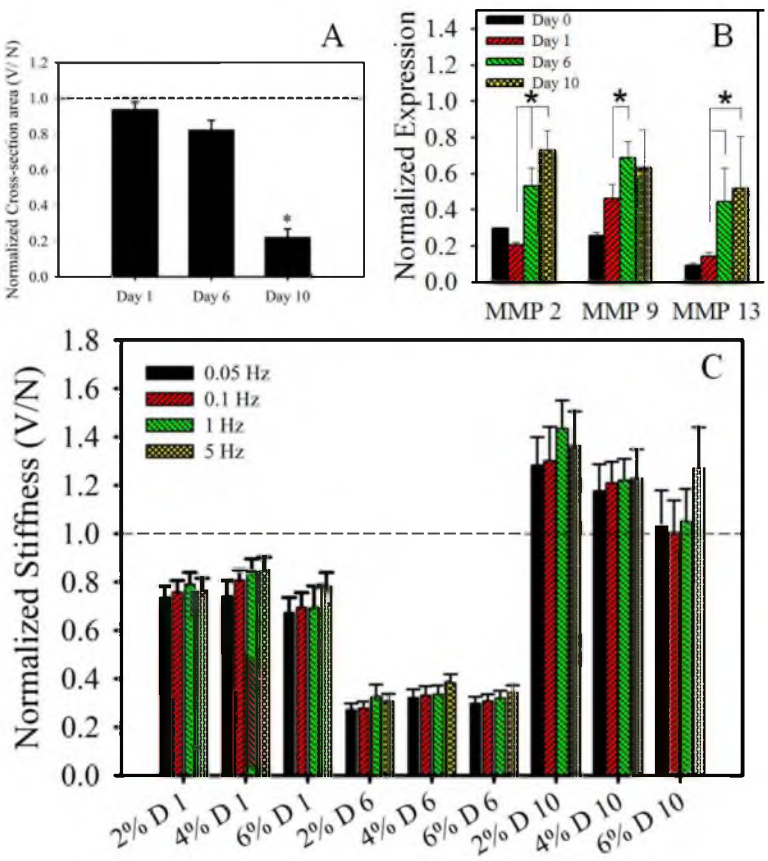

Figure 2.2: Angiogenic neovessels remodel the extracellular matrix (ECM) during growth. (A) Normalized cross-sectional area of the rectangular gels at Day 1, Day 6 and Day 10 of growth. The cross-sectional area of the gel significantly decreased over time as microvessels applied traction and contracted the matrix inward. (B) Normalized levels of mRNA expression for proteolytic matrix metalloproteases (MMPs) at Day 0, Day 1, Day 6 and Day 10. Expression of these proteolytic enzymes significantly increased over culture time. (C) Harmonic oscillation viscoelastic testing was used to measure the dynamic stiffness of the vascularized constructs at Day 1, Day 6 and Day 10. The cultures were tested at equilibrium strain levels of 2%, 4% and 10% at frequencies of 0.05, 0.1, 1.0 and 5.0 Hz. Increased MMP expression during growth reduced the dynamic stiffness of the cultures by Day 6. However, by Day 10 the dynamic stiffness was increased compared to the stiffness of initial cultures, even though proteolytic mRNA expression remained high. This was likely due to compaction of the matrix, reducing the fluid phase of the constructs.

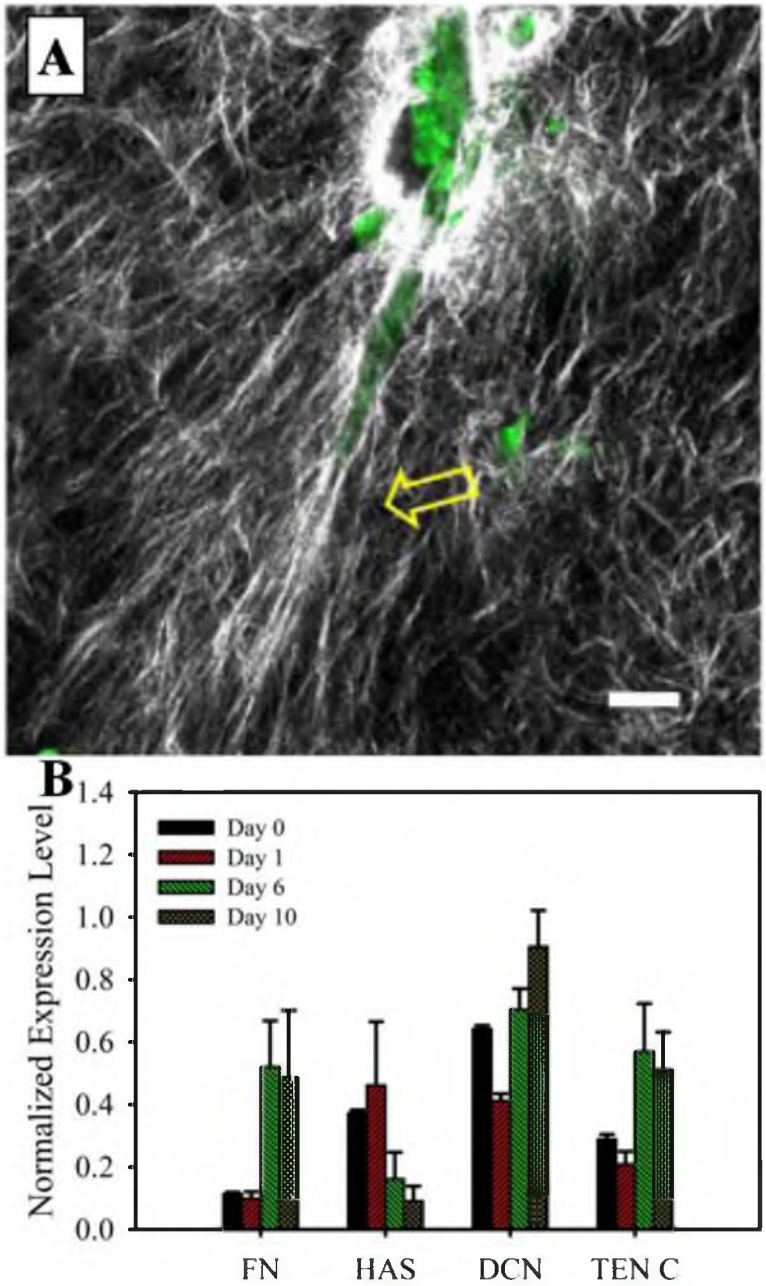

Figure 2.3: Angiogenic neovessels apply traction to the ECM and create new cell-matrix adhesions during growth. (A) Two-photon image of a neovessel sprout, indicated by the yellow arrow. Vessels were imaged using autofluorescence (green) and the collagen matrix was imaged using second-harmonic generation (white). As neovessels apply traction and contract the matrix, they draw collagen fibrils closer, condensing and re-orientating ECM fibrils toward the neovessel tip. Scale bar 20 μm. (B) Normalized expression for matrix molecules fibronectin (FN), decorin (DCN), tenascin C (TNC), and hyaluronan (HAS) at Day 0, Day 1, Day 6 and Day 10 of growth. During angiogenesis, expression of matrix molecules that promote angiogenesis increased (FN, DCN, TEN C) while expression for the angiogenesis-inhibiting molecule HAS decreased.

relationship between angiogenesis, the forces generated by neovessels during growth, and the mechanical properties of the ECM.

2.5 Effects of Mechanical Boundary Conditions on Vascular Alignment

Studies revealed a tight regulation between angiogenic growth and the mechanical properties of the ECM [64]. In the next study, this regulation was further investigated by examining the effects of mechanical stretch and boundary conditions on angiogenesis [65]. Mechanical boundary conditions and loading can significantly affect the morphometry of the vascular network and induce alignment (Figure 2.4). In these experiments, microvessels were cultured in rectangular gels with a long aspect ratio measuring 20.0 mm along the long axis, 5.0 mm along the short axis, and 3.0 mm through the thickness. Vessels within unconstrained constructs (i.e., shape controls) were randomly orientated with no preferred direction. When a 6% static or cyclic stretch was applied along the long-axis of the rectangular constructs, microvessels were found highly aligned along the direction of applied stretch. However, simply constraining the long-axis of the construct and with no applied stretch resulted in the same amount of vascular alignment, and applying load did not produce additional alignment over simply anchoring the culture. Additionally, collagen fibers were aligned along the long-axis in both the constrained cultures (no stretch) as well as the static and cyclically stretched cultures [65]. When these loading scenarios were replicated using avascular constructs, fibers were only oriented in the static and cyclic stretching cases [65]. These results indicate that while externally applied mechanical loads are capable of aligning collagen fibrils, internal traction generated by neovessels in the constrained

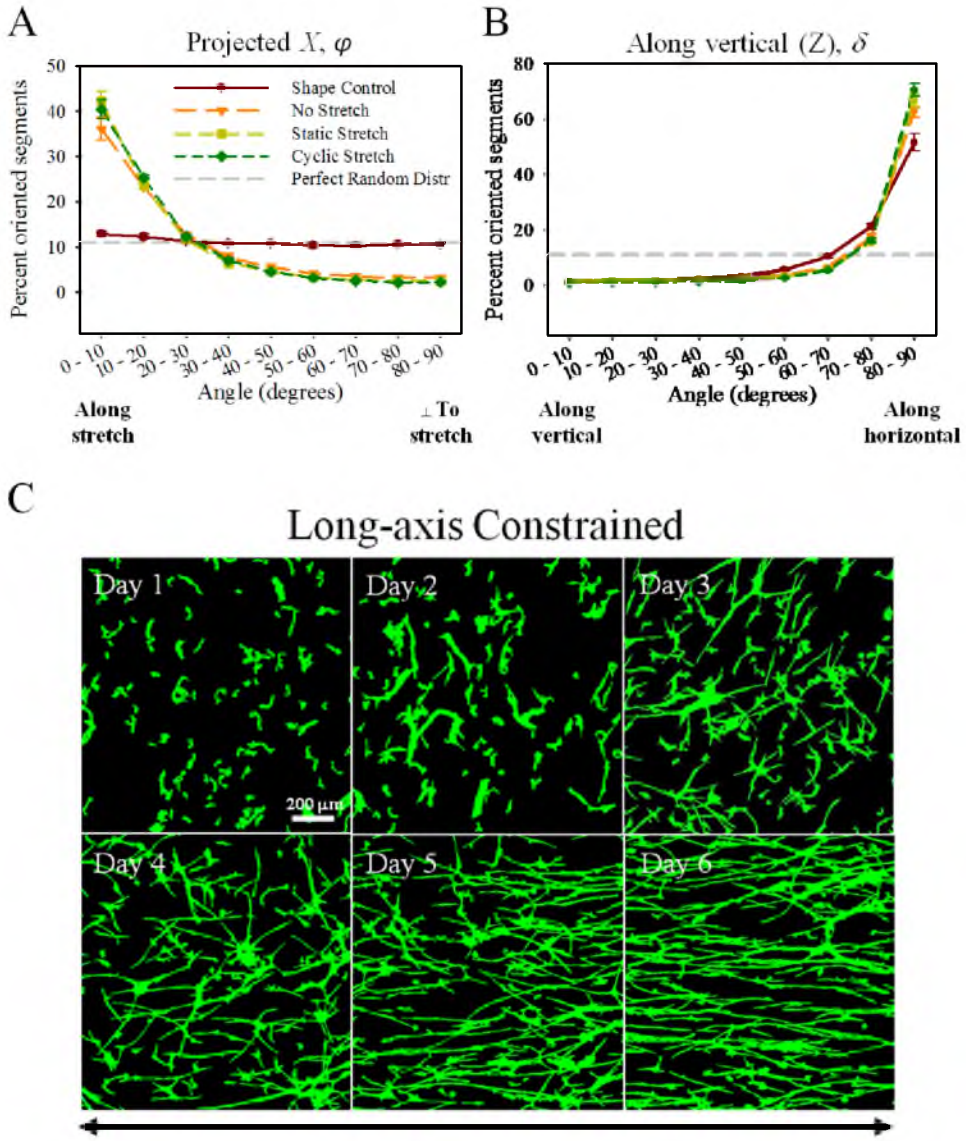

Figure 2.4: Applied load and mechanical boundary conditions affect the topology of the vascular network and induce alignment. (A) Microvessels in shape control constructs exhibited no preference in φ, while vessels within the no stretch, static stretch, and cyclic stretch groups were significantly aligned along the long-axis (x-axis). (B) Microvessels in all the experimental conditions exhibited preferential alignment within the horizontal plane, as indicated by the large percentage of vessels oriented perpendicular to the vertical axis (*z*-axis). (C) Angiogenic growth within a no stretch (long-axis constrained) vascularized construct, showing images of different cultures at different time points of growth after initial seeding. These gels were constrained along the long axis, indicated by the horizontal double arrow, using a stainless steel mesh. At Day 6 of growth, microvessels were highly aligned the constrained axis. Scale bar 200 µm.

cultures were sufficient to induce fibril alignment. Neovessels align with these fibrils via contact guidance, causing a positive feedback loop which results in the alignment of both microvessels and collagen fibrils along the constrained axis. Applying strain to the gels did not significantly increase alignment past the levels induced by the boundary constraint alone.

In a separate study, the implantation of pre-aligned vascularized constructs into immunocompromised mice was examined to determine the role of pre-existing vascular organization on subsequent neovessel growth and alignment (Figure 2.5) [69]. Rectangular constructs were grown *in vitro* within a stainless steel frame to constrain contraction along the long-axis. As a result, microvessels were highly aligned along the constrained long-axis prior to implantation at Day 7. During implantation, constructs were either cut away from the frame (unframed) or implanted with the frame (framed). At Day 30, microvessels within the unframed constructs had lost the initial pre-alignment and had no preferred directions, while vessels within the framed constructs remained highly aligned along the constrained axis (Figure 2.5 A). These results demonstrate that pre-alignment of microvascular precursors does not significantly influence the final topology of the microvascular network. Rather, the displacement constraint in the framed implants caused these constructs to maintain their prepatterned orientation. Computational simulations demonstrated that the difference in the 3D deformation pattern between the unframed and framed constructs during growth and remodeling was sufficient to explain these results (Figure 2.5 B). Finite element (FE) models were used to simulate the contraction of a construct, and nodal displacement from the simulation was interpolated to a skeletonized collection of

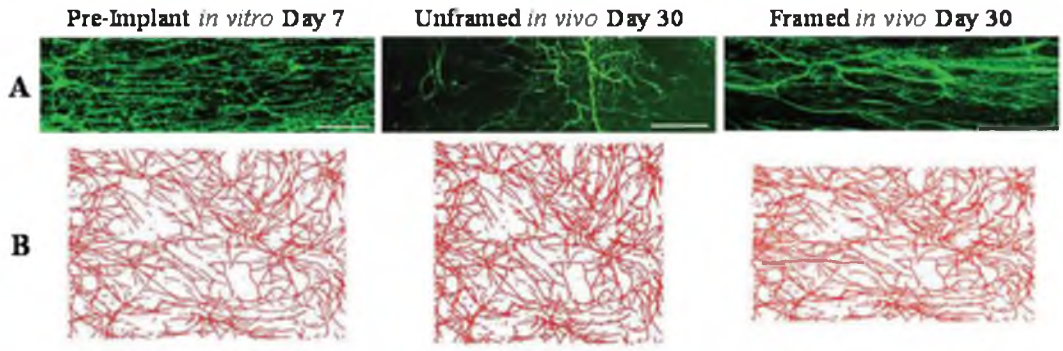

Figure 2.5: Implantation of pre-aligned vascularized constructs into immunocompromised mice demonstrates that pre-existing vascular organization has no effect on subsequent vascular alignment. (A) Confocal images of pre-aligned vascularized constructs at Day 7, prior to implantation (pre-implant, left). Constructs were pre-aligned by constraining the long-axis of the rectangular gels with a stainless steel mesh. Prior to implantation, constructs were either cut from the frame (unframed, middle) or left within the stainless steel frame (framed, right). Implants were removed and imaged at Day 30, revealing that microvessels within the unframed constructs had lost the initial pre-alignment and had no preferred direction, while vessels within the framed constructs remained highly aligned. (B) The deformation field from the finite element models was interpolated to a skeletonized dataset of randomly-orientated microvessels in order to determine how the deformation would affect vascular alignment. In the pre-implant simulation, microvessels were preferentially aligned along the long-axis of the construct. However, removal of the boundary condition in the unframed simulation caused microvessels to lose this alignment. Vessels in the framed simulation were subject to the boundary condition during the entire simulation and as a result were more highly aligned than vessels prior to implantation.

randomly-orientated microvessels. Once the boundary condition was removed, the unframed constructs began to contract isotropically rather than anistropically, and as a result, microvessels lost pre-alignment and became randomly oriented. These results demonstrate that constraining the ends of the culture to prevent contraction along the long-axis is sufficient to cause and maintain vascular alignment, and pre-organized microvasculature cannot maintain alignment without the displacement constraint.

These studies demonstrated the effects of deformation due to cell-generated traction forces and boundary conditions on vascular alignment, but the mechanisms behind these effects remained unclear. For example, do neovessels orient along tension along the constrained axis of the culture? Or, do microvessels become aligned along the direction of highest effective stiffness (i.e., the constrained axis) as the culture contracts laterally along the unconstrained directions? To further investigate the mechanisms by which boundary conditions induce vascular alignment, rectangular vascularized constructs were subjected to different mechanical conditions [73]. Changing the boundary conditions on the culture changes the directions of stress and strain during angiogenic growth. Four different sets of boundary conditions on the vascularized constructs were investigated in this study (ordered from least to most constrained): unconstrained (UNC), long-axis constrained (LAC), short-axis constrained (SAC), and long-short-axis constrained (LSAC) (Figure 2.6 A). In these experiments, altering the boundary conditions of the construct had significant effects on the length, branching, and orientation of the vascular network (Figure 2.6 B-D). Growth and branching decreased as the constructs became more constrained (Figure 2.6 B, C). The constrained directions can be thought of as presenting a very stiff resistance to traction forces

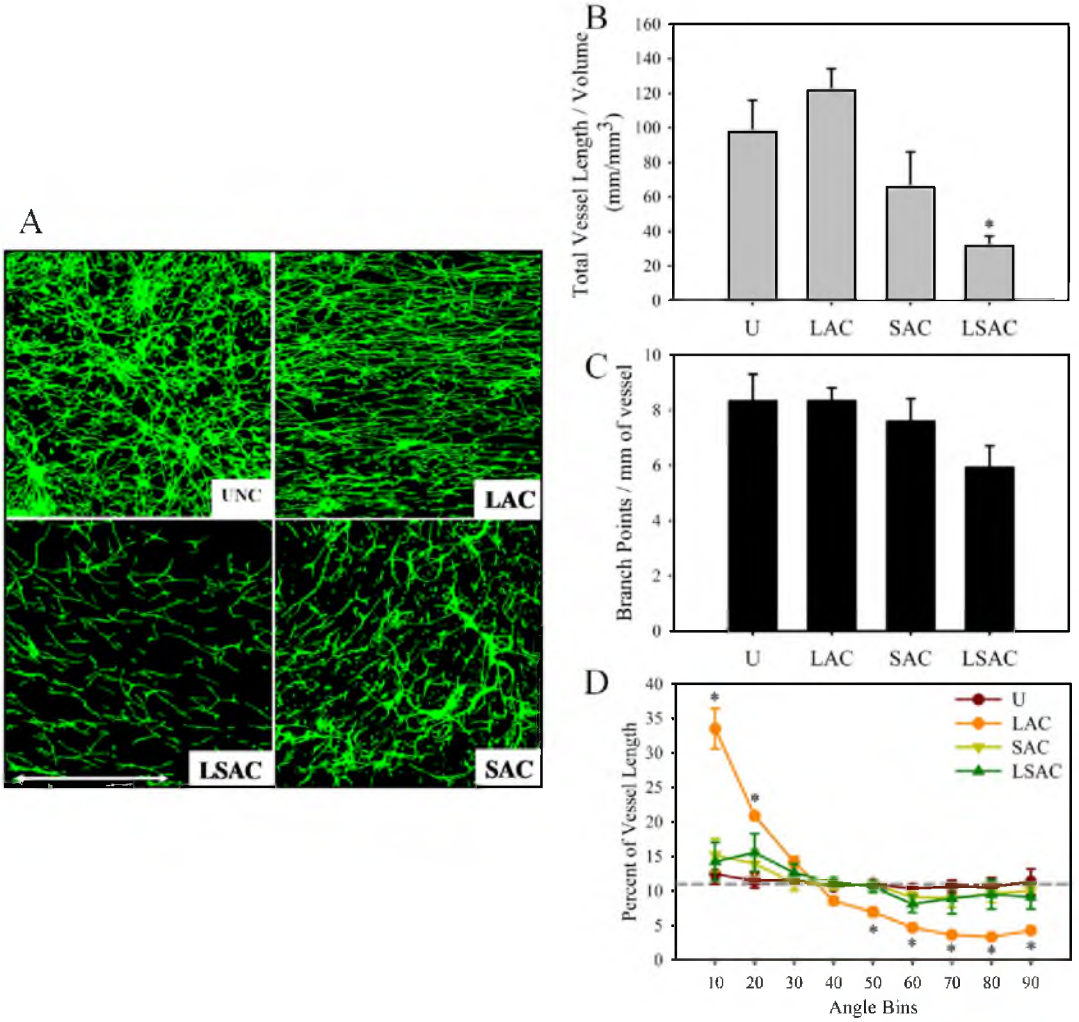

Figure 2.6: Mechanical boundary conditions regulate the topology of the emerging vascular network. (A) Vascularized gel cultures subjected to various mechanical boundary conditions (in order from least to most constrained): unconstrained (U, top left), long-axis constrained (LAC, top right), short-axis constrained (SAC, bottom right), and long-short-axis constrained (LSAC, bottom left). Altering the boundary conditions of the gel had significant effects on the length, branching, and orientation of the vascular network during angiogenesis. (B) The total length of the vascular network per unit of gel volume was measured in each of the boundary condition cases. No significant difference in total vascular length could be detected between U and LAC cultures, but there was a trend of reduced vascular length in the SAC and LSAC cultures, with length in the LSAC experiments significantly reduced. (C) The number of branching points per unit of vessel length decreased as the constructs became more constrained. (D) Microvessel orientation was measured in each boundary condition case by collected the distribution of vessel orientation angles with respect of the long-axis of the culture. Microvessels in the LAC cultures were highly aligned along the long-axis, while vessels within the U, SAC, and LSAC exhibited no preference.

applied by neovessels, and they are unable to condense the matrix and contract the construct along the constrained direction. As a result, tension (stress) develops along this direction. The trend of decreased growth and branching seen in the more constrained constructs suggests that raising the effective stiffness of the matrix through boundary constraint, thereby impeding the ability of neovessels to deform and remodel the matrix, reduces angiogenesis.

Microvessels in the UNC constructs were oriented randomly, while vessels in the LAC constructs were highly aligned along the constrained long-axis (Figure 2.6 D). However, in the SAC and LSAC cases, microvessels did not orient with respect to either the long- or short-axis of the constructs. In the constrained construct experiments, tension developed along the constrained directions as neovessel attempt to contract the matrix. The finding that microvessels in SAC constructs did not orient along the short-axis suggests that neovessels do not align along tension during growth. Furthermore, independent experiments demonstrated that elastic stress does not accumulate within these constructs. In experiments involving LAC constructs treated with Cytochalsin D to prevent cellular force generation, there was no measureable retraction once the construct was cut away from the boundary constraint. These results suggest that significant elastic stresses do not accumulate within the matrix due to the viscoelastic nature of collagen hydrogels, as stress is dissipated at a rate faster than they accumulate. The constrained gel experiments demonstrate that the deformation of the gel in response to cell-generated forces and remodeling is sufficient to cause microvascular alignment. In the LAC gels, the gel was free to deform lateral to the long-axis causing microvessels to align along the constrained axis. The SAC gels can

be thought of as a strip biaxial test: the short-axis was constrained, and the long-axis had a high effective stiffness as well due the aspect ratio of the gel. This prevented contraction along both the long- and short-axes of the gel during the culture, and as a result neovessels in these gels had no preferred alignment within the long-short plane.

Although these experiments have demonstrated that macroscale conditions such as gel boundary constraint can induce organization and alignment during angiogenesis, current experimental techniques lack the spatial and temporal resolution to determine the mechanisms behind these phenomena. The constrained vascularized gel experiments do not provide information about the state of stress and/or strain at the cellular level (microscale) and how changes to gel boundary conditions affects microscale mechanics and therefore matrix deformation and growth. Additionally, data from these experiments are limited to a single time-point so the experiments provide very little insight into the dynamics of the process. Computational modeling provides the means to supplement these experiments and provide insight into the mechanisms behind the biomechanical regulation of angiogenesis.

2.6 References

[1] Conway, E.M., Collen, D. and Carmeliet, P. (2001) "Molecular mechanisms of blood vessel growth," Cardiovasc Res 49:507-21.

[2] Carmeliet, P. (2004) "Manipulating angiogenesis in medicine," J Intern Med 255:538-61.

[3] Stevens, T., Rosenberg, R., Aird, W., Quertermous, T., Johnson, F.L., Garcia, J.G., Hebbel, R.P., Tuder, R.M. and Garfinkel, S. (2001) "NHLBI workshop report: Endothelial cell phenotypes in heart, lung, and blood diseases," Am J Physiol Cell Physiol 281:C1422-33.

[4] Adams, J.C. and Watt, F.M. (1993) "Regulation of development and differentiation by the extracellular matrix," Development 117:1183-98.

[5] Juliano, R.L. and Haskill, S. (1993) "Signal transduction from the extracellular matrix," J Cell Biol 120:577-85.

[6] Lukashev, M.E. and Werb, Z. (1998) "ECM signalling: Orchestrating cell behaviour and misbehaviour," Trends Cell Biol 8:437-41.

[7] Kim, S.H., Turnbull, J. and Guimond, S. (2011) "Extracellular matrix and cell signalling: The dynamic cooperation of integrin, proteoglycan and growth factor receptor," J Endocrinol 209:139-51.

[8] Saksela, O. and Rifkin, D.B. (1990) "Release of basic fibroblast growth factor-heparan sulfate complexes from endothelial cells by plasminogen activator-mediated proteolytic activity," J Cell Biol 110:767-75.

[9] Pepper, M.S. (2001) "Extracellular proteolysis and angiogenesis," Thromb Haemost 86:346-55.

[10] Stupack, D.G. and Cheresh, D.A. (2002) "ECM remodeling regulates angiogenesis: Endothelial integrins look for new ligands," STKE 7.

[11] Albrecht-Buehler, G. (1977) "Phagokinetic tracks of 3T3 cells: Parallels between the orientation of track segments and of cellular structures which contain actin or tubulin," Cell 12:333-9.

[12] Alessandri, G., Raju, K. and Gullino, P.M. (1983) "Mobilization of capillary endothelium in vitro induced by effectors of angiogenesis in vivo," Cancer Res 43:1790-7.

[13] Wong, M.K. and Gotlieb, A.I. (1984) "In vitro reendothelialization of a single-cell wound. Role of microfilament bundles in rapid lamellipodia-mediated wound closure," Lab Invest 51:75-81.

[14] Zetter, B.R. (1987) "Assay of capillary endothelial cell migration," Methods Enzymol 147:135-44.

[15] Pepper, M.S., Belin, D., Montesano, R., Orci, L. and Vassalli, J.D. (1990) "Transforming growth factor-beta 1 modulates basic fibroblast growth factor-induced proteolytic and angiogenic properties of endothelial cells in vitro," J Cell Biol 111:743-55.

[16] Taraboletti, G., Roberts, D., Liotta, L.A. and Giavazzi, R. (1990) "Platelet thrombospondin modulates endothelial cell adhesion, motility, and growth: A

potential angiogenesis regulatory factor," J Cell Biol 111:765-72.

[17] Klemke, R.L., Leng, J., Molander, R., Brooks, P.C., Vuori, K. and Cheresh, D.A. (1998) "CAS/Crk coupling serves as a "molecular switch" for induction of cell migration," J Cell Biol 140:961-72.

[18] Lampugnani, M.G. (1999) "Cell migration into a wounded area in vitro," Methods Mol Biol 96:177-82.

[19] Cai, G., Lian, J., Shapiro, S.S. and Beacham, D.A. (2000) "Evaluation of endothelial cell migration with a novel in vitro assay system," Methods Cell Sci 22:107-14.

[20] Goukassian, D., Diez-Juan, A., Asahara, T., Schratzberger, P., Silver, M., Murayama, T., Isner, J.M. and Andres, V. (2001) "Overexpression of p27(Kip1) by doxycycline-regulated adenoviral vectors inhibits endothelial cell proliferation and migration and impairs angiogenesis," Faseb J 15:1877-85.

[21] Santiago, A. and Erickson, C.A. (2002) "Ephrin-B ligands play a dual role in the control of neural crest cell migration," Development 129:3621-32.

[22] Auerbach, R., Lewis, R., Shinners, B., Kubai, L. and Akhtar, N. (2003) "Angiogenesis assays: A critical overview," Clin Chem 49:32-40.

[23] Albini, A., Benelli, R., Noonan, D.M. and Brigati, C. (2004) "The 'chemoinvasion assay': A tool to study tumor and endothelial cell invasion of basement membranes," Int J Dev Biol 48:563-71.

[24] Smith, J.T., Tomfohr, J.K., Wells, M.C., Beebe, T.P., Jr., Kepler, T.B. and Reichert, W.M. (2004) "Measurement of cell migration on surface-bound fibronectin gradients," Langmuir 20:8279-86.

[25] Madri, J.A. and Williams, S.K. (1983) "Capillary endothelial cell cultures: Phenotypic modulation by matrix components," J Cell Biol 97:153-65.

[26] Lawley, T.J. and Kubota, Y. (1989) "Induction of morphologic differentiation of endothelial cells in culture," J Invest Dermatol 93:59S- 61S.

[27] Bikfalvi, A., Sauzeau, C., Moukadiri, H., Maclouf, J., Busso, N., Bryckaert, M., Plouet, J. and Tobelem, G. (1991) "Interaction of vasculotropin/vascular endothelial cell growth factor with human umbilical vein endothelial cells: Binding, internalization, degradation, and biological effects." J Cell Physiol 149:50-9.

[28] Bikfalvi, A., Cramer, E.M., Tenza, D. and Tobelem, G. (1991) "Phenotypic modulations of human umbilical vein endothelial cells and human dermal fibroblasts using two angiogenic assays," Biol Cell 72:275-8.

[29] Grant, D.S., Lelkes, P.I., Fukuda, K. and Kleinman, H.K. (1991) "Intracellular mechanisms involved in basement membrane induced blood vessel differentiation in vitro," In Vitro Cell Develop Biol 27A:327-36.

[30] Kanzawa, S., Endo, H. and Shioya, N. (1993) "Improved in vitro angiogenesis model by collagen density reduction and the use of type III collagen," Ann Plast Surg 30:244-51.

[31] Zimrin, A.B., Villeponteau, B. and Maciag, T. (1995) "Models of in vitro angiogenesis: Endothelial cell differentiation on fibrin but not matrigel is transcriptionally dependent," Biochem Biophys Res Commun 213:630-8.

[32] Cockerill, G.W., Varcoe, L., Meyer, G.T., Vadas, M.A. and Gamble, J.R. (1998) "Early events in angiogenesis: cloning an alpha-prolyl 4-hydroxylase-like gene," Int J Oncol 13:595-600.

[33] Connolly, J.O., Simpson, N., Hewlett, L. and Hall, A. (2002) "Rac regulates endothelial morphogenesis and capillary assembly," Mol Biol Cell 13:2474-85.

[34] Gagnon, E., Cattaruzzi, P., Griffith, M., Muzakare, L., LeFlao, K., Faure, R., Beliveau, R., Hussain, S.N., Koutsilieris, M. and Doillon, C.J. (2002) "Human vascular endothelial cells with extended life spans: In vitro cell response, protein expression, and angiogenesis," Angiogenesis 5:21-33.

[35] Liu, J., Wang, X.B., Park, D.S. and Lisanti, M.P. (2002) "Caveolin-1 expression enhances endothelial capillary tubule formation," J Biol Chem 277:10661-8.

[36] Segura, I., Serrano, A., De Buitrago, G.G., Gonzalez, M.A., Abad, J.L., Claveria, C., Gomez, L., Bernad, A., Martinez, A.C. and Riese, H.H. (2002) "Inhibition of programmed cell death impairs in vitro vascular-like structure formation and reduces in vivo angiogenesi," Faseb J 16:833-41.

[37] Sun, X.T., Ding, Y.T., Yan, X.G., Wu, L.Y., Li, Q., Cheng, N., Qiu, Y.D. and Zhang, M.Y. (2004) "Angiogenic synergistic effect of basic fibroblast growth factor and vascular endothelial growth factor in an in vitro quantitative microcarrier-based three-dimensional fibrin angiogenesis system," World J Gastroenterol 10:2524-8.

[38] Bagley, R.G., Weber, W., Rouleau, C. and Teicher, B.A. (2005) "Pericytes and endothelial precursor cells: Cellular interactions and contributions to malignancy," Cancer Res 65:9741-50.

[39] Dietrich, F. and Lelkes, P.I. (2006) "Fine-tuning of a three-dimensional microcarrier-based angiogenesis assay for the analysis of endothelial-mesenchymal cell co-cultures in fibrin and collagen gels," Angiogenesis 9:111-25.

[40] Ghajar, C.M., Blevins, K.S., Hughes, C.C., George, S.C. and Putnam, A.J. (2006) "Mesenchymal stem cells enhance angiogenesis in mechanically viable prevascularized tissues via early matrix metalloproteinase upregulation," Tissue Eng 12:2875-88.

[41] Crabtree, B. and Subramanian, V. (2007) "Behavior of endothelial cells on Matrigel and development of a method for a rapid and reproducible in vitro angiogenesis assay," In Vitro Cell Dev Biol Anim 43:87-94.

[42] Frerich, B., Zuckmantel, K., Winter, K., Muller-Durwald, S. and Hemprich, A. (2008) "Maturation of capillary-like structures in a tube-like construct in perfusion and rotation culture," Int J Oral Maxillofac Surg 37:459-66.

[43] Ghajar, C.M., Chen, X., Harris, J.W., Suresh, V., Hughes, C.C., Jeon, N.L., Putnam, A.J. and George, S.C. (2008) "The effect of matrix density on the regulation of 3-D capillary morphogenesis," Biophys J 94:1930-41.

[44] Ghajar, C.M., George, S.C. and Putnam, A.J. (2008) "Matrix metalloproteinase control of capillary morphogenesis," Crit Rev Eukaryot Gene Expr 18:251-78.

[45] Churchman, A.T. and Siow, R.C. (2009) "Isolation, culture and characterisation of vascular smooth muscle cells," Methods Mol Biol 467:127-38.

[46] Kniazeva, E. and Putnam, A.J. (2009) "Endothelial cell traction and ECM density influence both capillary morphogenesis and maintenance in 3-D," Am J Physiol Cell Physiol 297:C179-87.

[47] Thakar, R.G., Cheng, Q., Patel, S., Chu, J., Nasir, M., Liepmann, D., Komvopoulos, K. and Li, S. (2009) "Cell-shape regulation of smooth muscle cell proliferation," Biophys J 96:3423-32.

[48] Fleming, P.A., Argraves, W.S., Gentile, C., Neagu, A., Forgacs, G. and Drake, C.J. (2010) "Fusion of uniluminal vascular spheroids: A model for assembly of blood vessels," Dev Dyn 239:398-406.

[49] Ghajar, C.M., Kachgal, S., Kniazeva, E., Mori, H., Costes, S.V., George, S.C. and Putnam, A.J. (2010) "Mesenchymal cells stimulate capillary morphogenesis via distinct proteolytic mechanisms," Exp Cell Res 316:813-25.

[50] Wang, M., Su, Y., Sun, H., Wang, T., Yan, G., Ran, X., Wang, F., Cheng,T and

Zou, Z. (2010) "Induced endothelial differentiation of cells from a murine embryonic mesenchymal cell line C3H/10T1/2 by angiogenic factors in vitro," Differentiation 79:21-30.

[51] Nicosia, R.F., Lin, Y.J., Hazelton, D. and Qian, X. (1997) "Endogenous regulation of angiogenesis in the rat aorta model. Role of vascular endothelial growth factor," Am J Pathol 151:1379-86.

[52] Kruger, E.A., Duray, P.H., Tsokos, M.G., Venzon, D.J., Libutti, S.K., Dixon, S.C., Rudek, M.A., Pluda, J., Allegra, C. and Figg, W.D. (2000) "Endostatin inhibits microvessel formation in the ex vivo rat aortic ring angiogenesis assay," Biochem Biophys Res Commun 268:183-91.

[53] Blacher, S., Devy, L., Burbridge, M.F., Roland, G., Tucker, G., Noel, A. and Foidart, J.M. (2001) "Improved quantification of angiogenesis in the rat aortic ring assay," Angiogenesis 4:133-42.

[54] Zhu, W.H. and Nicosia, R.F. (2002) "The thin prep rat aortic ring assay: A modified method for the characterization of angiogenesis in whole mounts," Angiogenesis 5:81-6.

[55] Go, R.S. and Owen, W.G. (2003) "The rat aortic ring assay for in vitro study of angiogenesis," Methods Mol Med 85:59-64.

[56] Goodwin, A.M. (2007) "In vitro assays of angiogenesis for assessment of angiogenic and anti-angiogenic agents," Microvasc Res 74:172-83.

[57] Reed, M.J., Karres, N., Eyman, D. and Vernon, R.B. (2007) "Culture of murine aortic explants in 3-dimensional extracellular matrix: A novel, miniaturized assay of angiogenesis in vitro," Microvasc Res 73:248-52.

[58] Bellacen, K. and Lewis, E.C. (2009) "Aortic ring assay," J Vis Exp 24.

[59] Laschke, M.W., Vollmar, B. and Menger, M.D. (2009) "Inosculation: Connecting the life-sustaining pipelines," Tissue Eng Part B Rev 15:455-65.

[60] Nicosia, R.F., Zhu, W.H., Fogel, E., Howson, K.M. and Aplin, A.C. (2005) "A new ex vivo model to study venous angiogenesis and arterio-venous anastomosis formation," J Vasc Res 42:111-9.

[61] Hoying, J.B., Boswell, C.A. and Williams, S.K. (1996) "Angiogenic potential of microvessel fragments established in three-dimensional collagen gels," In Vitro Cell Dev Biol Anim 32:409-19.

[62] Shepherd, B.R., Chen, H.Y., Smith, C.M., Gruionu, G., Williams, S.K. and Hoying, J.B. (2004) "Rapid perfusion and network remodeling in a microvascular construct after implantation," Arterioscler. Thromb. Vasc. Biol. 24:898-904.

[63] Chang, C.C. and Hoying, J.B. (2006) "Directed three-dimensional growth of vascular cells and isolated microvessel fragments," Cell Transplant 15:533-540.

[64] Krishnan, L., Hoying, J.B., Nguyen, H., Song, H. and Weiss, J.A. (2007) "Interaction of angiogenic microvessels with the extracellular matrix," Am J Physiol Heart Circ Physiol 293:H3650-8.

[65] Krishnan, L., Underwood, C.J., Maas, S., Ellis, B.J., Kode, T.C., Hoying, J.B. and Weiss, J.A. (2008) "Effect of mechanical boundary conditions on orientation of angiogenic microvessels," Cardiovasc Res 78:324-32.

[66] Chang, C.C., Nunes, S.S., Sibole, S.C., Krishnan, L., Williams, S.K., Weiss, J.A. and Hoying, J.B. (2010) "Angiogenesis in a microvascular construct for transplantation depends on the method of chamber circulation," Tissue Eng. Part A 16:795-805.

[67] Nunes, S.S., Greer, K.A., Stiening, C.M., Chen, H.Y., Kidd, K.R., Schwartz, M.A., Sullivan, C.J., Rekapally, H. and Hoying, J.B. (2010) "Implanted microvessels progress through distinct neovascularization phenotypes," Microvasc. Res. 79:10-20.

[68] Nunes, S.S., Krishnan, L., Gerard, C.S., Dale, J.R., Maddie, M.A., Benton, R.L. and Hoying, J.B. (2010) "Angiogenic potential of microvessel fragments is independent of the tissue of origin and can be influenced by the cellular composition of the implants," Microcirc 17:557-567.

[69] Chang, C.C., Krishnan, L., Nunes, S.S., Church, K.H., Edgar, L.T., Boland, E.D., Weiss, J.A., Williams, S.K. and Hoying, J.B. (2012) "Determinants of microvascular network topologies in implanted neovasculatures," Arterioscler Thromb Vasc Biol 32:5-14.

[70] Edgar, L.T., Maas, S.A., Guilkey, J.E. and Weiss, J.A. (2014) "A continuous-discrete finite element model of sprouting angiogenesis that couples neovessel growth with matrix deformation," Biomech Model Mechanobiol, in press.

[71] Edgar, L.T., Sibole, S.C., Underwood, C.J., Guilkey, J.E. and Weiss, J.A. (2013) "A computational model of in vitro angiogenesis based on extracellular matrix fibre orientation," Comput Methods Biomech Biomed Engng 16:790-801.

[72] Edgar, L.T., Underwood, C.J., Guilkey, J.E., Hoying, J.B. and Weiss, J.A. (2014) "Extracellular matrix density and compliance regulate the rate of neovessel growth and branching in sprouting angiogenesis," PLoS One 9.

[73] Underwood, C.J., Edgar, L.T., Hoying, J.B. and Weiss, J.A. (2013) "Cell-generated forces and the resulting matrix deformation cause microvascular alignment in vascularized collagen gels," Am J Physiol Heart Circ Physiol, 307: H152-64.

[74] Shepherd, B.R., Chen, H.Y., Smith, C.M., Gruionu, G., Williams, S.K. and Hoying, J.B. (2004) "Rapid perfusion and network remodeling in a microvascular construct after implantation," Arterioscler Thromb Vasc Biol 24:898-904.

[75] Kirkpatrick, N.D., Andreou, S., Hoying, J.B. and Utzinger, U. (2007) "Live imaging of collagen remodeling during angiogenesis," Am J Physiol Heart Circ Physiol 292:H3198-206.

[76] Burbridge, M.F., Coge, F., Galizzi, J.P., Boutin, J.A., West, D.C. and Tucker, G.C. (2002) "The role of the matrix metalloproteinases during in vitro vessel formation," Angiogenesis 5:215-26.

[77] Stupack, D.G. and Cheresh, D.A. (2002) "ECM remodeling regulates angiogenesis: Endothelial integrins look for new ligands," STKE 7.

[78] Davies Cde, L., Melder, R.J., Munn, L.L., Mouta-Carreira, C., Jain, R.K. and Boucher, Y. (2001) "Decorin inhibits endothelial migration and tube-like structure formation: Role of thrombospondin-1," Microvasc Res 62:26-42.

[79] Kim, C.H., Bak, K.H., Kim, Y.S., Kim, J.M., Ko, Y., Oh, S.J., Kim, K.M. and Hong, E.K. (2000) "Expression of tenascin-C in astrocytic tumors: Its relevance to proliferation and angiogenesis," Surg Neurol 54:235-40.

[80] Schonherr, E., O'Connell, B.C., Schittny, J., Robenek, H., Fastermann, D., Fisher, L.W., Plenz, G., Vischer, P., Young, M.F. and Kresse, H. (1999) "Paracrine or virus-mediated induction of decorin expression by endothelial cells contributes to tube formation and prevention of apoptosis in collagen lattices," Eur J Cell Biol 78:44-55.

[81] Schonherr, E., Sunderkotter, C., Schaefer, L., Thanos, S., Grassel, S., Oldberg, A., Iozzo, R.V., Young, M.F. and Kresse, H. (2004) "Decorin deficiency leads to impaired angiogenesis in injured mouse cornea," J Vasc Res 41:499-508.

[82] Spring, J., Beck, K. and Chiquet-Ehrismann, R. (1989) "Two contrary functions of tenascin: Dissection of the active sites by recombinant tenascin fragments,"

Cell 59:325-34.

[83] Zagzag, D., Shiff, B., Jallo, G.I., Greco, M.A., Blanco, C., Cohen, H., Hukin, J., Allen, J.C. and Friedlander, D.R. (2002) "Tenascin-C promotes microvascular cell migration and phosphorylation of focal adhesion kinase," Cancer Res 62:2660-8.

[84] Tempel, C., Gilead, A. and Neeman, M. (2000) "Hyaluronic acid as an anti-angiogenic shield in the preovulatory rat follicle," Biol Reprod 63:134-140.

CHAPTER 3

A COMPUTATIONAL MODEL OF IN VITRO ANGIOGENESIS BASED ON EXTRACELLULAR MATRIX FIBER ORIENTATION*

3.1 Abstract

Recent interest in the process of vascularization within the biomedical community has motivated numerous new research efforts focusing on the process of angiogenesis. Although the role of chemical factors during angiogenesis has been well documented, the role of mechanical factors, such as the interaction between angiogenic vessels and the extracellular matrix, remains poorly understood. *In vitro* methods for studying angiogenesis exist, however, measurements available using such techniques often suffer from limited spatial and temporal resolution. For this reason, computational models have been extensively employed to investigate various aspects of angiogenesis. This manuscript outlines the formulation and validation of a simple and robust computational model developed to accurately simulate angiogenesis based on length, branching, and orientation morphometrics collected from vascularized tissue constructs. Microvessels were represented as a series of connected line segments. The morphology of the vessels

*Reprinted with permission, Edgar, L.T., Sibole, S.C., Underwood, C.J., Guilkey, J.E., and J.A. Weiss, "A computational model of in vitro angiogenesis based on extracellular matrix fibre orientation," *Computer Methods in Biomechanics and Biomedical Engineering*, 2013.

was determined by a linear combination of the collagen fiber orientation, the vessel density gradient, and a random walk component. Excellent agreement was observed between computational and experimental morphometric data over time. Computational predictions of microvessel orientation within an anisotropic matrix correlated well with experimental data. The accuracy of this modeling approach makes it a valuable platform for investigating the role of mechanical interactions during angiogenesis.

3.2 Introduction

Angiogenesis, the process by which new blood vessels sprout off from existing vasculature, is highly sensitive to both the chemical and the mechanical microenvironment [1 - 4]. During angiogenesis, endothelial cells within existing blood vessels detach from the basement membrane, migrate into the ECM, and form sprouts that elongate and eventually mature into new vasculature. Externally applied and cell-generated traction forces affect motility, metabolism, proliferation and differentiation of all anchorage-dependent cells, including endothelial cells and pericytes that participate in angiogenesis [5 - 11]. Mechanical stimuli received by cells via mechanotransduction depends on the structure and composition of the extracellular matrix (ECM) [12, 13] and on cell receptor structures bound to ECM components [14].

The mechanism as to how mechanical forces, 3D boundary conditions and ECM structure/composition influence neovessel growth during angiogenesis is poorly understood. Investigating this mechanism is difficult as the ECM is constantly remodeled and reorganized during angiogenesis through protease activity, formation of new cell-matrix adhesions, and cellular force generation [15, 16]. Overcoming these

challenges and characterizing the mechanical interactions between angiogenic microvessels and the ECM would not only provide new insight into the driving forces behind morphogenic processes, but would also lead to new design considerations for engineering patterned microvasculature.

The role of mechanical factors during angiogenesis has been previously investigated *in vitro* using a novel 3D culture method [3, 16 - 19]. Using this method, sprouting occurs within microvessel fragments in a spontaneous and consistent manner. Sprouts elongate as patent tubes, branching and forming anastomoses with other vessels [20, 21]. In free floating constructs, microvascular networks were found to have no preferred orientation. When the vascularized constructs were subject to an applied strain or a boundary constraint, microvessels and collagen fibers were found aligned along the constrained axis [3]. It is unclear if this alignment arises from microvessel growth being directed along aligned collagen fibers, from microvessels being reoriented due to contraction of the matrix and internal remodeling, or from some combination of both mechanisms.

Computational models can be utilized to supplement experimental efforts, often providing investigators with the ability to view systems at time points not sampled during the experiment or test hypotheses in ways not possible in the lab. Growth models have proven useful to investigators studying angiogenesis [22 – 27]. Computational frameworks can be categorized into different classes depending on how the system of interest is represented. Continuous models are typically governed by differential equations based on physical laws, while discrete models assemble a collection of discrete geometric units that behave according to a particular set of rules.

Continuous-discrete models, or hybrid models, combine both approaches, often through determining the behavior of discrete units by solving a problem governed by physical laws. A computational model capable of simulating the interaction between microvessels and the ECM during angiogenesis would be a valuable platform for studying the role of mechanical forces, matrix boundary conditions, and ECM composition.

Vascular geometry can be captured in two ways: Imaging data from vascularized constructs (specimen-specific data) or from computational predictions of microvessel growth. Since geometry obtained using the first method is constrained to the time point at which the culture was imaged, the second method was chosen as it provides a generalized description of microvascular geometry at any desired point in time. This manuscript proposes such a computational model of vessel growth, designed to provide accurate, up-to-date microvascular geometry during *in vitro* angiogenesis. The model was designed using a continuous-discrete framework. This involves explicit representation of the microvessels as discrete structures with the ability to simulate elongation, branching, and anastomosis over a regular computational grid. The continuous component of the model is in the differential equations used to govern field variables that influence neovessel growth. The growth model will also need to accurately predict the changes in microvessel growth resulting from ECM anisotropy and imposed boundary conditions as seen in the laboratory. The objectives of this study were to develop such a growth model and to demonstrate its ability to describe experimental data on microvessel length, branching, and orientation obtained from vascularized constructs.

3.3 Methods

3.3.1 Cell culture experiments – *In vitro* model of angiogenesis

Morphometric data were collected from *in vitro* cultures of angiogenic microvessels in order to calibrate the computational growth model and to determine if predictions from the simulation framework were valid. Based on previously described methods [20], 38 microvessel cultures were prepared from 5 separate dissections. Microvessel fragments were isolated from epydidimal fat pads harvested from retired breeder Sprague-Dawley rats while conforming to the University of Utah Institutional Animal Care and Use Committee (IACUC). The fat pads were minced, digested with enzymes and subjected to sequential filtration. The filtration step allows the removal of large clumps of tissue as well as single cells from the suspension. The remaining filtrate was spun down in a centrifuge, and the resulting pellet consisted of microvessel fragments. Sterile rat tail type I collagen (BD Biosciences, Franklin Lakes, NJ) was mixed with concentrated Dulbecco's modified Eagle medium (DMEM, GIBCO-Invitrogen, Carlsbad, CA) to a density of 3.0 mg/ml collagen in 1X DMEM. The pellet of microvessel fragments was resuspended in the collagen/DMEM solution at a density of 15,000 fragments/ml, and the solution was transferred to circular culture wells (diam. ~ 15mm). The collagen was allowed to polymerize at 37°C, 95% humidity for 30 minutes. Constructs were incubated in serum-free media [32] supplemented with rhVEGF (10 ng/ml, VEGF 165, PeproTech, Rocky Hill, NJ). The constructs cast within the circular culture wells were free-floating with no applied stretch or imposed boundary conditions, which created collagen fibers with no preferred orientation (random) (Figure 3.1 A, B). Constructs were incubated at 37°C and 95% humidity for 7 days, after which the microvascular

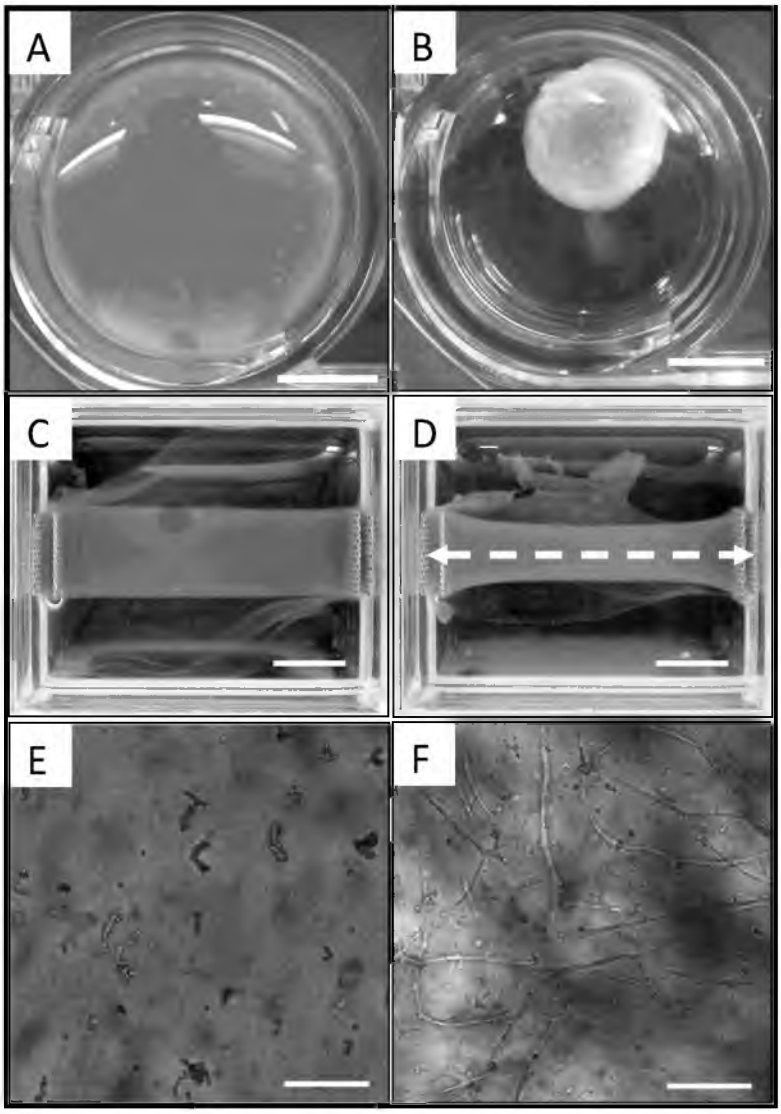

Figure 3.1: Microvessel cultures provided an *in vitro* model of angiogenesis used for validating the computational model. Collagen gels serving as the ECM were subjected to two different boundary conditions. (A) Round, free-floating culture at Day 0. (B) After 6 days, free-floating gels were uniformly contracted by cellular traction forces. Scale bar = 5 mm. (C) Rectangular collagen gel with the long axis constrained at Day 0. (D) After 6 days, the fixed-edge constructs contracted along the short axis, with the most contraction found at the center of the gel (furthest point away from the boundary conditions). Microvessels and collagen fibers within these constructs were found predominately orientated along the constrained axis, shown as a white dashed line. Scale bar = 5 mm. (E) A 10X light micrograph displaying initial microvessel fragments within a free-floating collagen gel at Day 0. (F) Representative growth profile seen within a free-floating vascularized construct after 6 days of culture. Scale bar = 200 μm.

network within each construct was imaged using confocal microscopy.

To create the anisotropic ECM condition, 5 rectangular vascularized constructs were also prepared. These constructs were subjected to fixed-edge boundary conditions by allowing the collagen to polymerize within a stainless steel mesh, preventing contraction of the collagen gel along the long axis but leaving the rest of the gel free to contract (Figure 3.1 C, D). This boundary condition produces microvessel and collagen fibril alignment along the long axis of the constructs [3]. Microvessel orientation data were collected after 6 days of growth to compare with the simulation results. Collagen fiber orientation data were also collected to provide the fiber orientation information for the model when simulating the anisotropic matrix condition.

3.3.2 Image acquisition and processing

At the end of each culture period, the vascularized constructs were fixed with 4% formaldehyde overnight and then washed with phosphate-buffered saline (PBS) containing 0.1% Triton-X-100. Endothelial cells were stained with a 2 μg/ml solution of Isolectin IB4-Alexa 488 conjugate (Invitrogen, Carlsbad, CA). 3D image datasets of the stained microvessels were obtained using laser scanning confocal microscopy (Olympus FV1000 CLSM) utilizing a 488 nm excitation laser and a 10X objective. Six adjacent fields (1.27x1.27 mm) were acquired about the construct center through a depth of 300 μm from the bottom surface of the gel with a 2.5 μm z-step interval. Individual image stacks were acquired at a resolution of 512 x 512 x 300 voxels.

The image stacks for the 6 adjacent fields were stitched together using custom software. Unless specified, all other image processing was performed through Amira™

(Mercury Computer Systems, Carlsbad, CA). A blind deconvolution (10 iterations) was performed on image stacks using a point spread function based on the numerical aperture (NA = 0.4, 10X – air), wavelength of light (λ = 520 nm), and an estimate of the refractive index of the collagen gel (n = 1.35, [33]) to eliminate out-of-plane blur. Volume data were filtered to remove fragments smaller than 600 μm^3, as it was observed that objects below this size range were usually due to single cells, debris or noise and did not represent microvessels. Microvessel volumes were then reduced to line segments by a skeletonization algorithm as previously described [3, 16]. A custom application was used to analyze the skeletonized data and collect the total vessel length and number of branches in each culture [34]. Although it is possible that some branch points may represent anastomoses, it was assumed that all branch points represent new sprouts branching from existing vessels. This is a reasonable assumption because anastomosis requires microvessels to be within close proximity of each other and the topology of the microvascular network in this culture model primarily results from divergent growth [3, 16 - 19].

3.3.3 Morphometric data – Vascular length

A function describing microvessel growth over time was created from experimental data to define growth within the computational model. For each time point sampled, the length of all microvessels within the field was normalized by the initial number of microvessel fragments. The number of initial fragments was calculated from the seeding density used when preparing the cultures (15,000 fragments/ml). This normalization ensures that the growth mechanisms within the model are independent

from the initial microvessel seeding density. Length metric data from each experiment were averaged across each of the free-floating cultures, and these data were fit with a 4-parameter sigmoid curve:

$$g(t) = g_0 + \frac{a_1}{1 + e^{-[(t-t_{1/2})/b_1]}} \tag{3.1}$$

This function describes the total vascular length within the domain at any point in time. A sigmoid curve was chosen to describe microvessel growth, as such a curve is often used to describe population growth restricted by limited resources (carrying capacity). In Equation 3.1, g_0 is the initial microvessel length (bottom of the sigmoid curve), a_1 is the range of the function (top minus bottom), $t_{1/2}$ is the time at which $g(t)$ is halfway in between the top and bottom of the sigmoid curve, and b_1 describes the steepness of the curve. The carrying capacity of the system can be described as $g_0 + a_1$.

3.3.4 Morphometric data – Vascular branching

The computational model also required a function describing microvessel branching over time. For each time point, the number of branch points within the field were averaged together and normalized by the initial number of microvessel fragments. The branching $b(t)$ was calculated by fitting the average branching data with a 3-parameter exponential curve:

$$b(t) = b_0 + a_2 e^{b_2 t} \tag{3.2}$$

In this equation, b_0 describes the initial number of branches, a_2 scales the exponential term, and b_2 describes the rate of branch formation. An exponential function was used to describe branch formation as branching metric data taken from

experimental cultures do not appear to approach any limit during the 7 day culture period.

3.3.5 Collagen fiber orientation

The culture and imaging procedure described above was repeated for the 5 fixed-edge constructs at day 6 of culture. Measurements from these constructs included the angles for all microvessel segments relative to the constrained axis (long axis). The structural organization of the underlying collagen matrix within the fixed-edge constructs was quantified by imaging collagen fibrils using confocal reflectance microscopy with a 60X water objective and a 633 nm laser. For each construct, two stacks were acquired through a depth of 120 μm with a 1 μm z-step interval. An orientation of collagen fibers was determined from the images by employing a 2D Fourier transform technique on each image [35, 36]. The angle distributions from the 5 cultures were averaged together and fit with a Gaussian distribution. This distribution was used to seed a vector field that represents an anisotropic matrix for the computational growth model.

3.3.6 Computational model — Overview

The computational model of vessel growth during *in vitro* angiogenesis was calibrated and validated with data obtained using the methods described above. The formulation and implementation was 3D, although for simplicity the simulations presented in this manuscript were only performed in two dimensions. The simulation domain, or virtual ECM, was discretized with a regular quadrilateral mesh with an

element spacing of 31.75 μm in each direction. Local field information such as ECM collagen fibril orientation and microvessel density was specified at each of the grid nodes. At any position (x,y), the field described at the nodes could be mapped to that point via bilinear shape functions:

$$\varphi(x,y) = \sum_{i=1}^{4} S_i(x,y)\varphi_i \tag{3.3}$$

where φ was a field variable and $S_i(x,y)$ were the values of the shape functions for each of the four nodes of the cell, evaluated at the point (x,y) (Figure 3.2). This approach can be applied to include any field information deemed pertinent by the user. The dimensions of the domain were 1.27x1.27 mm for all simulations, corresponding to the 10X field of view on the confocal microscope. Periodic boundary conditions were imposed on all edges of the simulation domain.

3.3.7 Computational model – Vessel elongation

Initial microvessel fragments were represented as discrete independent line segments with lengths corresponding to the value of the sigmoid growth curve $g(t)$ at time $t = 0$ (Equation 3.1). Twenty-five fragments (average number in the field of view of a confocal image) were seeded throughout the domain, each at a random position and with a random orientation.

At each time step, microvessel growth was represented by the addition of new segments to the free ends of existing segments. A variable time step was implemented to limit the growth of any vessel segment to half a grid cell. The length of each new segment was calculated by referencing the growth curve $g(t)$ and determining the

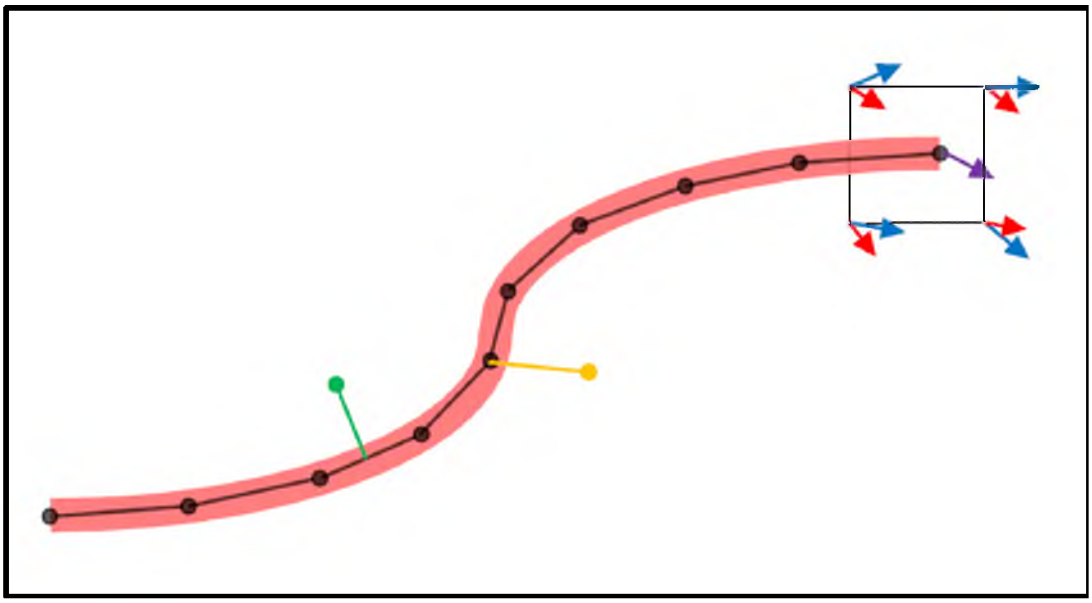

Figure 3.2: Microvessels were represented as a series of line segments. At each time step, neovessel growth occurred through the addition of a new line segment at the active tips of existing segments. The orientation of new segments was determined from information stored at the nodes of the grid cell. In this figure, the red and blue arrows represent directional cues determined by field information stored at the nodes. The red arrows are longer than the blue to represent the uneven weighting of various factors, i.e., collagen fibril direction was more influential than vessel density gradient. The direction of the new segment (purple arrow) was determined by interpolation of red and blue field variables via bilinear shape functions (Equation 2.3). At each time step, a segment formed a branch if a random number was below a branching probability parameter. The yellow segment demonstrates a branch formation. Anastomoses can form anywhere along a microvessel where an intersection occurs, as shown by the green line segment.

change in length over the time step size (Equation 3.1). With this method of vessel elongation, all vessels within the domain grow by the same amount at each time step. While this method may not accurately describe real growth of an individual neovessel, this method does provide valid predictions of microvascular topology in an averaged sense. The direction of new segments was determined by a linear combination of several directional cues. The orientation vector $\boldsymbol{v}$ for a newly created segment was found using the following expression:

$$\boldsymbol{v} = w_1\boldsymbol{\theta}_{coll} + w_2\boldsymbol{\theta}_{vdens} + w_3\boldsymbol{\theta}_{rand} \tag{3.4}$$

In Equation 3.4, the vector $\boldsymbol{\theta}_{coll}$ was along the direction of local collagen fibers, the vector $\boldsymbol{\theta}_{vdens}$ was calculated from the vessel density gradient to cause microvessels to grow away from regions of high microvessel density, and the vector $\boldsymbol{\theta}_{rand}$ was a random-walk component. The scalars w_1, w_2, and w_3 were the weights for each of these components. Each of the directional components was determined by mapping field information stored at the nodes of the grid to the position of the new segment (Equation 3.3).

3.3.8 Computational model – Branching

Microvessel branching was modeled as a stochastic process. During each time step, each segment was assigned a random number between 0 and 1. Branching occurred when a segment's random number was less than a branching probability value:

$$B_t = \frac{B_0}{t}\Delta t$$

$$\textit{if } \texttt{rand}[0,1] \le B_t, \text{ form a new branch} \tag{3.5}$$

$$\textit{else } \text{do not branch}$$

The initial branching probability, B_0, value was determined using a golden section, single variable, bounded optimization algorithm to minimize the root-mean-square (RMS) error between simulated and experimental length and branch metrics. This probability value was assigned to all initial fragments at $t = 0$ where Equation 3.5 is undefined. Multiplying by the time step Δt eliminated dependence of branching behavior on time step size. Based on Equation 3.5, the branching probability for an individual line segment decreases as time increases. This particular behavior was chosen because the rate at which new segments formed in the model would otherwise far outpace the rate at which new branches were observed to form in the experimental cultures.

3.3.9 Computational model – Anastomosis

Growth tips within close proximity to other microvessels were capable of forming anastomoses. At the end of each time step, a search for intersections between all active vessel tips and existing segments was conducted. If the intersection found was in between two segments within the same vessel, the intersection was ignored to avoid the formation of a terminal loop. If the intersecting segments were not from the same microvessel, a procedure was used to determine if they would intersect in three dimensions. This process is necessary because the model represented a 2D projection of vessels in three-dimensions. In three dimensions, a microvessel could be positioned at any point throughout the culture thickness of 300 μm. To account for the 3D geometry, a test was performed based on the probability of the two microvessels being offset by less than 1 microvessel diameter in the third spatial dimension. This involved

taking the ratio between the microvessel diameter and the culture thickness. If the random number was less than this ratio, the microvessels formed an anastomosis and cease growth; otherwise, the intersection was ignored.

3.3.10 Computational model – Optimization of branching

A golden-section line search was used to determine the optimal value of B0 within the branching mechanism (Equation 3.5) by minimizing the RMS error between simulated and experimental branching data:

$$\min \sum_{i=1}^{n} \sqrt{\frac{\left(\psi_e(t_i) - \psi_m(t_i)\right)^2}{n}} \tag{3.6}$$

Here, $\psi_e(t_i)$ was branching metric value from experimental data at a given time point, t_i, $\psi_m(t_i)$ was the branching metric from the computational simulations, and n was the number of time steps taken.

3.3.11 Computational model – ECM anisotropy

The computational model was designed with the ability to simulate microvessel growth under various matrical boundary conditions. Different boundary conditions were modeled by changing the orientation of collagen fibrils within the matrix. For simulations involving a free-floating collagen gel, a random collagen fiber orientation angle between –90° and 90° was generated at each node of the grid. When simulating angiogenesis within the anisotropic matrix condition, nodal collagen fiber orientation values were seeded using angle distributions collected from the fixed-edge constructs. The orientation of microvessels from these simulations was compared to orientation

data from the fixed-edge constructs to verify the model's ability to predict angiogenesis within an anisotropic matrix.

3.3.12 Computational model – Optimization of vessel orientation

Microvessel orientation within the model was optimized to match experimental data. A routine similar to Equation 3.6 was used to determine the optimal values of the weights describing the strength of directional cues when determining the orientation of new microvessel segments (w_1, w_2, $w3$) (Equation 3.4). These weights were adjusted to minimize the RMS error between microvessel orientation in the fixed-edge constructs on Day 6 and microvessel orientation from the anisotropic ECM simulations:

$$\min \sum_{i=1}^{n} \sqrt{\frac{\left(\phi_e(i) - \phi_m(i)\right)^2}{n}} \tag{3.7}$$

where $\phi_e(i)$ was the percentage of microvessels whose orientation angle fell into discrete angle bin i (0°-10°, 10°-20°, …, 80°-90°) measured off the constrained axis. $\phi_m(i)$ was the percentage of microvessels found in bin i from the simulations, and n was the number of discrete angle bins.

3.3.13 Computational model – Variation due to stochastic processes

While microvessel elongation within the model was a deterministically-governed process, the mechanisms for branching and anastomosis were stochastically-based. Since branch formation and anastomosis directly affect the number of active growth tips, stochastic variations between different simulations can be passed from these random mechanisms to length metric data. To eliminate stochastic variations, growth

rate was normalized by the number of active growth tips currently in the model. This adjustment ensures that the total length in each simulation will not vary too far away from the value prescribed by $g(t)$, reducing significant variation in length metric data over multiple simulations.

The seed used to initialize the random number generator algorithm prior to each simulation was varied based on the system clock. In order to assess the degree of variance across simulations caused by the stochastic processes, 50 simulations of microvessels growing within a randomly-orientated ECM were conducted, each using a unique seed. The variance in the length and branch metrics between these trials was then evaluated using a 1-way ANOVA.

Variations in the simulation results due to the stochastic components of the model prevented convergence to strict tolerances (ε = 1e-7) during the optimization routines. Therefore, a constant seed was used while optimizing individual parameters to facilitate convergence.

3.4 Results

Microvessel growth profiles were consistent across all *in vitro* experiments. Very little growth occurred before the 3-4 day mark, at which point sprouting was observed. Microvessels grew with at a high rate until Day 6-7, after which growth rate began to slow as the system neared its carrying capacity (Figure 3.3 – A). The sigmoid curve fit to the averaged length metric data ($g(t)$, Equation 3.1) resulted in an R^2 value of 0.998. The number of branch points measured in the vascularized constructs increased exponentially throughout time with no observable limit during the 7 day culture period

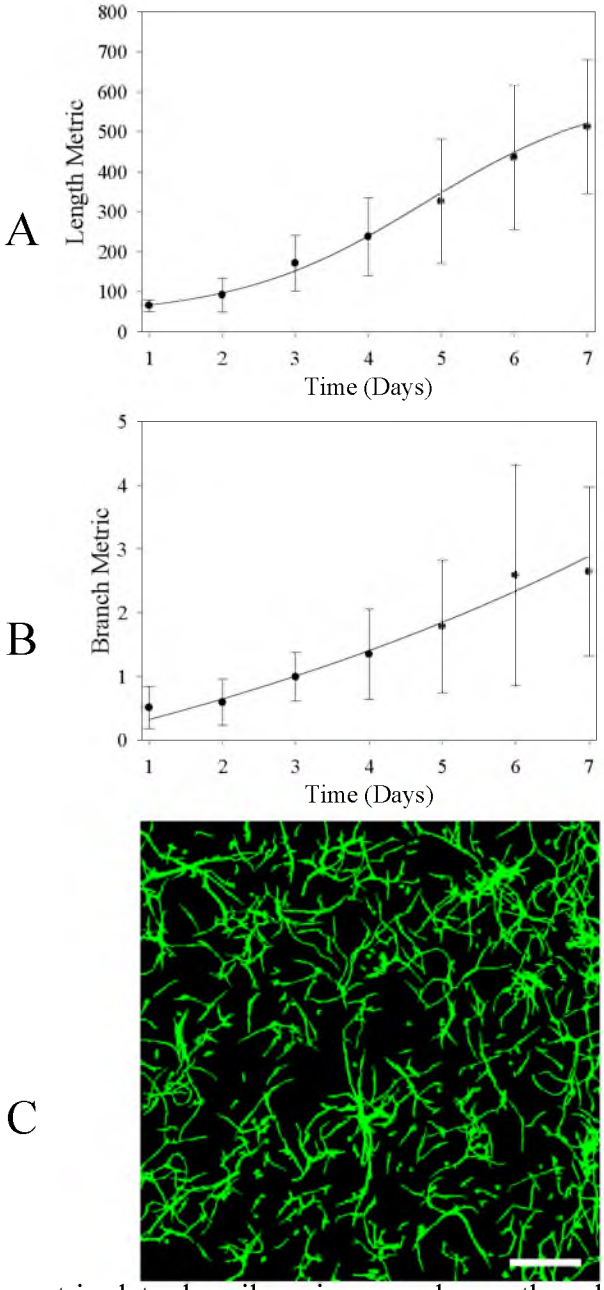

Figure 3.3: Morphometric data describe microvessel growth and branching during angiogenesis. (A) Length metric data (current vessel length/number of vessels at Day 1) versus time. The function *g(t)* was fit to this data (Equation 2.1). (B) Microvessel branch metric data (current number of branches/number of vessels at Day 1) versus time. The function *b(t)* was fit to these data (Equation 2.2). In both A and B, points represent experimental data (mean ± standard deviation) while solid curves represent regression fits. (C) Z-projection of a representative microvessel culture. Image data were collected by imaging vascularized constructs at Day 6 using a confocal microscope. Scale bar = 400 μm.

(Figure 3.3 – C). The exponential curve fit to the averaged branch metric data ($b(t)$, Equation 3.2) achieved an R^2 value of 0.968. The parameters determined from the curve fits can be found compiled in Table 3.1. Variance in length and branch metric data across *in vitro* cultures was high, with maximum standard deviations of 179.7 and 1.74, respectively.

Microvessel growth resulting from computational simulations resembled growth profiles seen *in vitro* (Figure 3.4). The length of microvascular networks from the computational simulations correlated well with experimental data, with approximately 1% normalized RMS error between computational and experimental length metric data (Figure 3.5 – A). The optimization routine used to determine the branching chance parameter returned a value of $B_0 = 0.038$ (Equation 3.5). This branching parameter minimized the normalized RMS error between computational and experimental branching metric data to roughly 6% (Figure 3.5 – B). Microvessels within the fixed-edge constructs were found preferentially aligned along the constrained axis, consistent with what has been seen in past experiments [3]. The majority of fibers in the fixed-edge constructs were found aligned along the constrained axis. The distributions of fiber angles for all 5 of the fixed-edge constructs were averaged together and fit to a Gaussian distribution which was used to generate a collagen fiber orientation at each node of the grid node (Figure 3.6).

Simulations of angiogenesis within a randomly-oriented ECM produced microvessels with no preferential alignment, similar to what has been seen in free-floating vascularized constructs [3] (data not shown). The computational model was also successful at predicting angiogenesis within an anisotropic ECM. The angle

Table 3.1: Values for the parameters in the model assigned during the simulations.

Growth function *g(t)*	
a_1	568.6
g_0	38.8
b_1	1.3
$t_{1/2}$	4.8
Branching function *b(t)*	
y_0	-2.50
a_2	2.62
b_2	0.105
Branching Probability	
B0	0.038
Strength of Directional Cues	
w_1 *Fiber Orientation*	0.508
w_2 *Vessel Density*	0.238
w_3 *Random Walk*	0.254

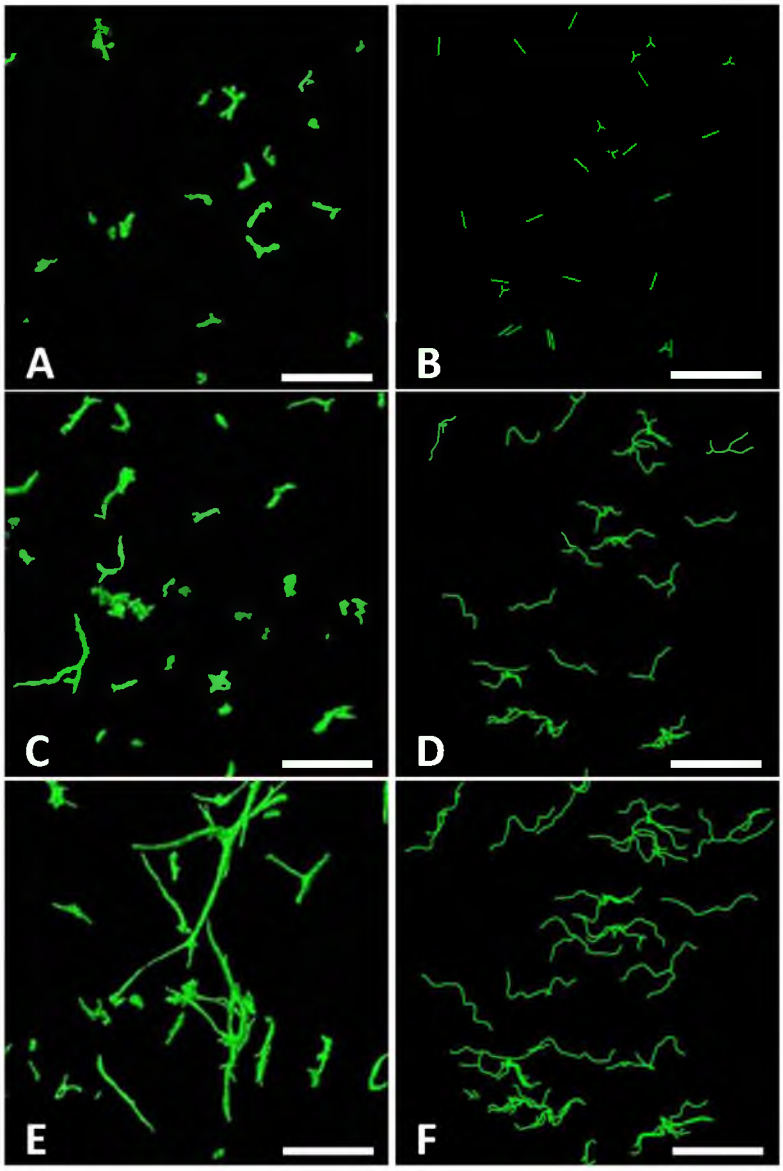

Figure 3.4: Images from computational simulations presented for comparison with experimental data. Confocal images from vascularized constructs are on the left, while data from simulations of microvessel growth can be found on the right. The time points at which these images were obtained are as follows: Day 1 (A, B), Day 4 (C, D), and Day 7 (E, F). Scale bar = 300 μm. Predictions of microvasculature from the computational model were similar to images taken from vascularized constructs. Notice that growth predicted in the simulations followed a more tortuous path compared to microvessels *in vitro*.

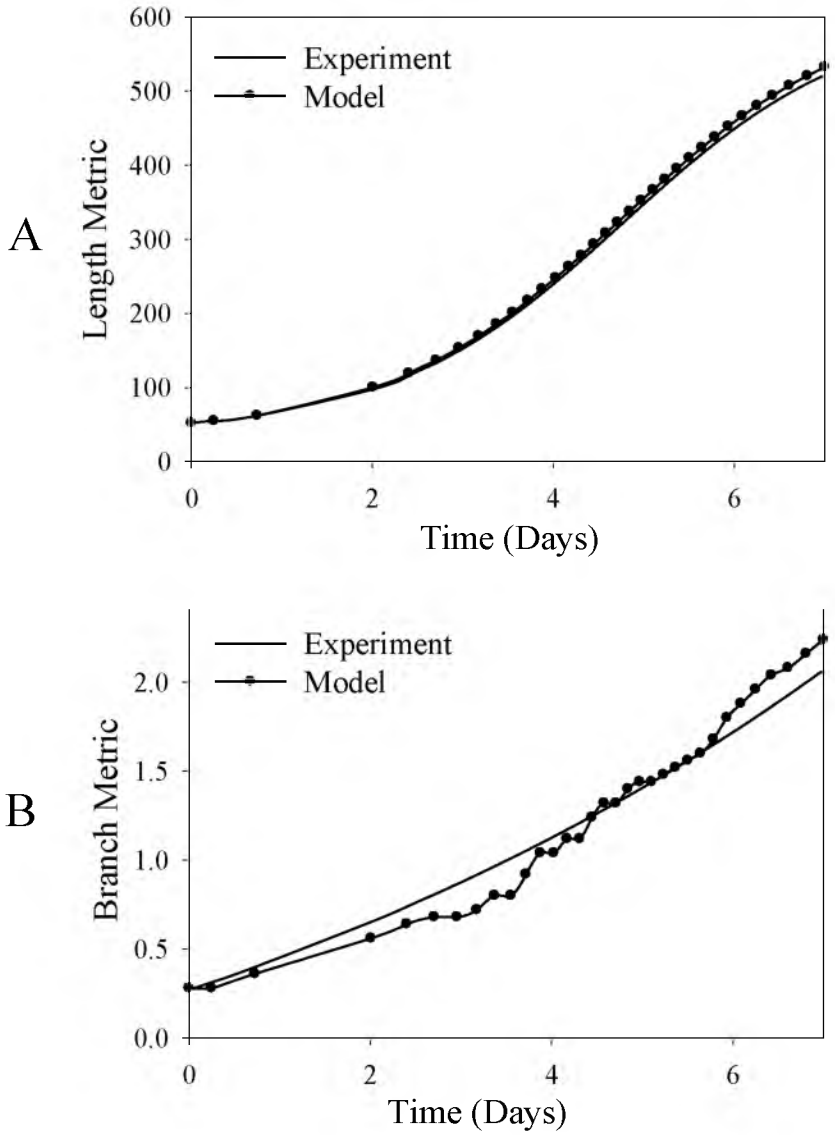

Figure 3.5: Computational simulations accurately predict experimental length and branching metric data taken from experimental cultures. (A) Comparison of computational and experimental length metric data versus time. There was a normalized RMS error of approximately 1% between the two datasets. (B) Comparison of simulated and experimental branch metric data (number of current branches divided by initial number of microvessels in culture) versus time. There was a normalized RMS error of approximately 6% between the two datasets.

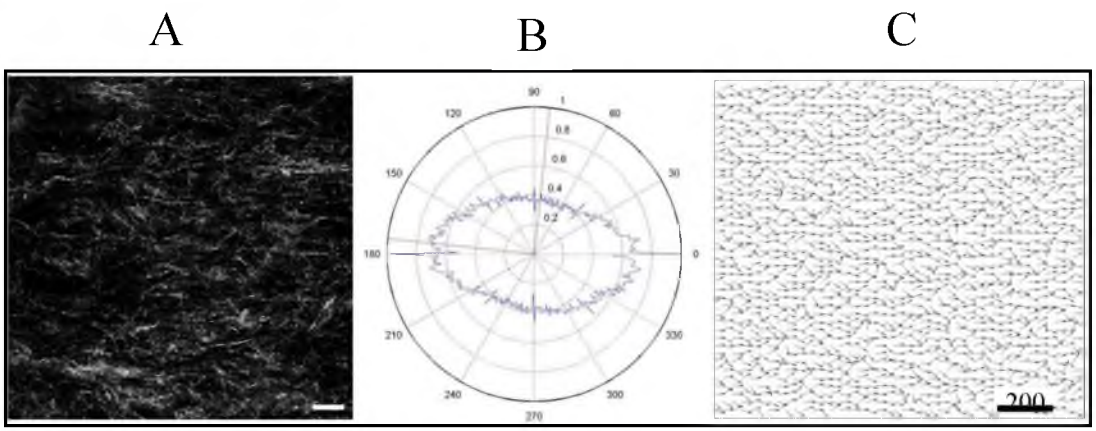

Figure 3.6: Anisotropic collagen fibril orientation was observed within the fixed-edge constructs. (A) Confocal reflection microscopy image of collagen fibrils within a representative fixed-edge construct at Day 6 *in vitro*. (B) FFT analysis of collagen fibril data from constrained gels. Collagen fibrils were found to be predominately aligned along the constrained axis (0^{o}-180^{o}). (C) A field of collagen fibril angles based on angle distribution extracted from confocal reflectance microscopy images. This vector field was stored at the nodes of the grid in simulations of angiogenesis subject to the anisotropic ECM condition. Scale bar = 200 μm.

between each microvessel and the long axis of the vascularized construct was measured from the simulations and constrained gel experiments. In both the simulations and experiments, the majority of microvessels were found aligned within 20° of the constrained axis (Figure 3.7). Although significant differences exist between computational and experimental data for some of the angle bins, the correlation coefficient between the two datasets was calculated to be $R^2 = 0.98$. The weights w_1, w_2, and w_3 of the three directional components described in Equation 3.4 were determined by optimizing the orientation of microvessel segments within the computational model (Table 3.1).

To render length data from the simulations immune to these stochastic variations, the growth function $g(t)$ was normalized by the number of active growth tips within the simulation. This method was tested by observing the final length metric value over 50 simulations. For each of the 50 simulations, the final length metric value did not significantly vary from the value prescribed by $g(t)$ (Figure 3.8 – A). In contrast, when the same test is performed for branch metric data, the number of branching points within the simulation varied significantly across 50 simulations (Figure 3.8 – B).

3.5 Discussion

The continuous-discrete framework outlined in this manuscript was successful at predicting length and branching behavior exhibited by angiogenic microvessels *in vitro*. Measurements of growth, branching, and alignment metrics provided by simulations had excellent statistical agreement with experimental data. This accuracy was obtained through optimization of only four parameters: the branching probability constant and

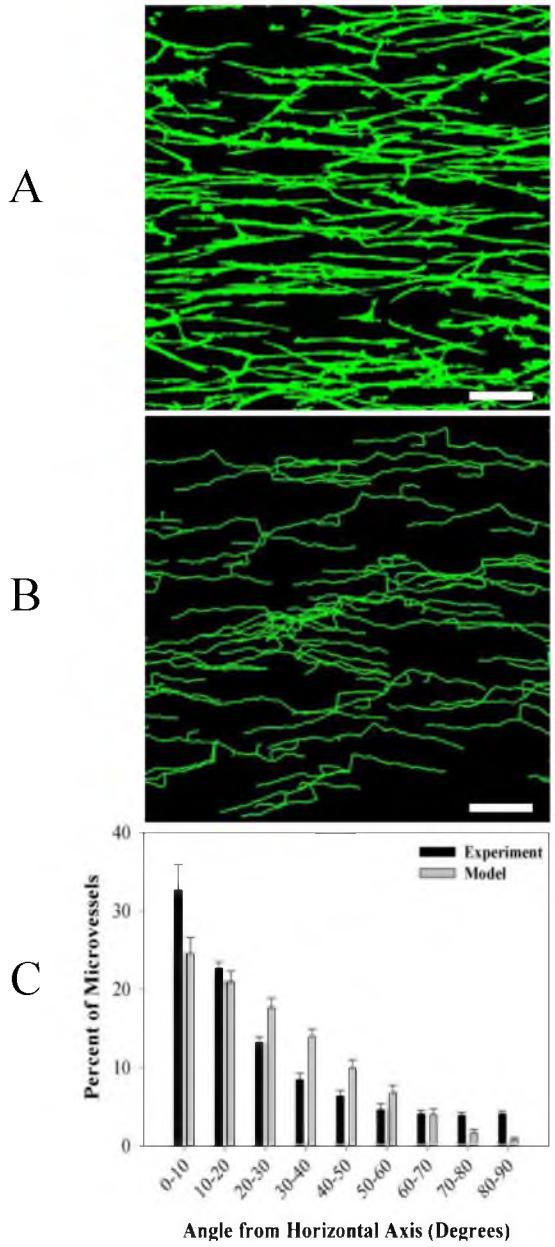

Figure 3.7: Computational simulations successfully predicted microvessel orientation within an anisotropic ECM. (A) Microvessels cultured within the fixed-edge constructs were found predominately aligned along the constrained axis. (B) Computational simulations of angiogenesis occurring with an anisotropic ECM accurately predicted experimental findings. (C) The angle between each microvessel segment and the horizontal axis was collected and sorted into discrete bins. Orientation data from the computational model correlated well with data from the fixed-edge vascularized constructs. Scale bar = 400 μm.

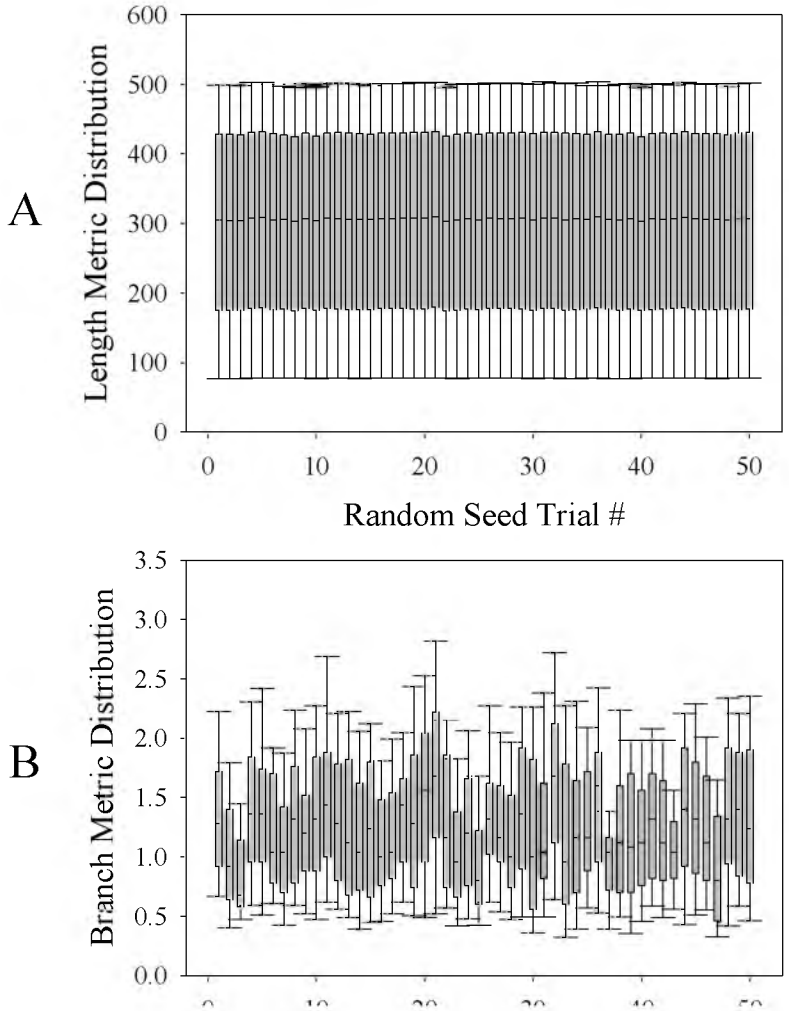

Figure 3.8: Stochastic variation within the computational simulations. Box-whisker plots of length (A) and branch (B) metric collected over 50 simulations, each with a unique P-RNG seeds. A 1-way ANOVA was performed to check for significant variance between trials. No significant variation in the length metric was seen while varying the P-RNG seed ($p = 1.0$). Branching was modeled as a stochastic process, and therefore the branch metric significantly varied between trials ($p < 0.001$).

the three weights influencing growth direction. Introducing additional parameters into the optimization routine would lead to even greater predictive performance from the model, but the simple approach employed in this work satisfied the objectives of this study.

Orientation data from simulations of the anisotropic ECM condition correlated well with microvessel orientation observed in the fixed-edge vascularized constructs. However, angle data from the simulations tended to favor the acute angle bins more than the corresponding experimental data. Approximately 90% of microvessels from the simulations were found orientated between 0° and 45° off of the constrained axis. Only 80% of microvessels within the fixed-edge constructs fell within this same range. Although this difference is seemingly trivial, it is important to account for all inconsistencies between the model and *in vitro* findings. This particular inconsistency is important since the cornerstone assumption for this simulation framework is that microvessel growth follows collagen fiber orientation. The inconsistency in microvessel orientation during simulations of the anisotropic ECM condition may be due to the assignment of an aligned ECM on Day 0 of each simulation. Within the fixed-edge constructs, angiogenesis begins in a random ECM which is remodeled during vessel growth, resulting in an aligned matrix. In future simulations, supplying a fibril orientation field that can vary over time will allow the model to capture the transition to anisotropy that results from matrix remodeling. While the growth of angiogenic microvessels may follow matrix fiber orientation through contact guidance [1, 3, 16], neovessels may also alter local fiber orientation by applying traction forces to the ECM during growth. This leads to a coupling between angiogenic growth and

matrix deformation, and it is difficult to separate these effects. In order to investigate this phenomenon, the authors plan to couple the computational model of vessel growth to a framework in solid mechanics that can predict deformation of the ECM during angiogenesis. However, the intricate nature of neovessel morphology makes it difficult to represent their geometry using traditional discretization schemes in computational solid mechanics such as the finite element (FE) method. One possible approach to deal with representing the microvessel morphology was described in a recent study, using a particle-based method known as the naterial point method (MPM) [28, 29]. With this method, particle distributions can be generated from confocal microscopy image datasets on a specimen-specific basis [30, 31]. The coupling of the growth model with simulations of solid mechanics will create a more realistic simulation of *in vitro* angiogenesis.

Although the simulations and experiments agreed statistically, there were qualitative discrepancies in the computational predictions of microvessel morphology. Simulated microvessel growth followed a more tortuous path compared to microvessels cultured in the lab. This discrepancy resulted from the mechanism used to determine the orientation of new segments within the computational model. New segments are allowed to form any angle with the parent vessel segment, leading to kinked microvessel morphology during elongation. Implementation of a persistence component into the vessel growth mechanism will make the microvessels resistant to changes in direction, ideally eliminating this morphological discrepancy.

The stochastic processes within the model led to minimal variation between simulations. Microvessel length was unaffected by the random numbers generated

during the simulations. This independence from the random processes was expected as microvessel growth rate was normalized to account for the random formation of branches and anastomoses. However, some aspects of microvascular topology were sensitive to variations in the random number generator seed. Branching was governed by a stochastic process, and branches would form at different times and in different locations after reseeding the random number generator. Likewise, the position and orientation of initial microvessel fragments would vary between random number generations as well. The conclusion is that these stochastic variations are small enough to not cause instabilities, yet pronounced enough to ensure that each simulation returns a unique microvascular network.

Future development of the computational framework will involve the replacement of stochastic components with deterministic mechanisms. For example, past mathematical models have suggested that steep gradients in collagen density local to a tip cell can induce the formation of a branch [24]. Likewise, with further analysis of confocal image data it may be possible to determine the degree of persistence involved during microvessel elongation. During the simulation, ECM collagen fibril orientation was supplied as an input parameter. Therefore, future simulations could easily predict *in vitro* angiogenesis for a given matrix orientation by simply mapping the desired fibril orientation field to the grid.

Chemical factors such as VEGF, TGF-β, and PDGF play a vital role during angiogenesis [1]. In order to isolate and study the impact of mechanical/structural stimuli during angiogenesis, the current model implementation does not include any chemotactic guidance during neovessel outgrowth. The *in vitro* system being modeled

was uniformly immersed in VEGF, leaving only local synthesis of chemical factors as a possible source of chemical inhomogeneity. Rat tail type I collagen used for the experimental model does not contain trapped cytokines that can be released upon digestion [37, 38]. Therefore, it was possible to simulate *in vitro* angiogenesis accurately without including chemotaxis since significant chemotactic gradients do not develop within the vascularized constructs.

The algorithms described in this study were highly robust and efficient, with simulations completing within seconds. The model demonstrates forward compatibility through the ability to simulate different matrical boundary conditions and simple coupling to optimization algorithms.

The growth model will provide the MPM algorithm with an accurate and current microvessel geometry that can be used to determine the state of stress/strain within microvessels and the surrounding matrix for any given point in time [30]. Information about the deformation from the MPM simulations can then be used to update important information such as matrix fiber orientation, matrix density, and vessel stretch. This information can be used to direct vessel growth in the next time step, and this process will repeat as both models step throughout time.

In summary, the simulation framework outlined in this work was capable of producing an accurate description of microvascular length, branching, and orientation metrics over time for both an isotropic and anisotropic ECM fibril orientation field. The extent of angiogenesis can be tightly controlled by adjusting the input parameters, giving the model the ability to simulate a wide range of problems. Finally, the shape functions within the grid provide a basis for expanding the model to include additional

field variables that influence neovessel growth and orientation. For example, stress/strain fields could be mapped to the nodes of the grid within the vessel growth model, effectively coupling stress and strain fields within the matrix to angiogenesis. These features allow this framework to serve as an effective platform for exploring how mechanical interactions between neovessels and the ECM regulate angiogenesis.

3.6 References

[1] Shiu, Y.T., Weiss, J.A., Hoying, J.B., Iwamoto, M.N., Joung, I.S. and Quam, C.T. (2005) "The role of mechanical stresses in angiogenesis," Crit Rev Biomed Eng 33:431-510.

[2] Ingber, D.E. (2002) "Mechanical signaling and the cellular response to extracellular matrix in angiogenesis and cardiovascular physiology," Circ Res 91:877-87.

[3] Krishnan, L., Underwood, C.J., Maas, S., Ellis, B.J., Kode, T.C., Hoying, J.B. and Weiss, J.A. (2008) "Effect of mechanical boundary conditions on orientation of angiogenic microvessels," Cardiovasc Res 78:324-32.

[4] Li, S., Huang, N.F. and Hsu, S. (2005) "Mechanotransduction in endothelial cell migration," J Cell Biochem 96:1110-26.

[5] Carosi, J.A., Eskin, S.G. and McIntire, L.V. (1992) "Cyclical strain effects on production of vasoactive materials in cultured endothelial cells," J Cell Physiol 151:29-36.

[6] Stamatas, G.N. and McIntire, L.V. (2001) "Rapid flow-induced responses in endothelial cells," Biotechnol Prog 17:383-402.

[7] McCormick, S.M., Frye, S.R., Eskin, S.G., Teng, C.L., Lu, C.M., Russell, C.G., Chittur, K.K. and McIntire, L.V. (2003) "Microarray analysis of shear stressed endothelial cells," Biorheology 40:5-11.

[8] Patrick, C.W., Jr. and McIntire, L.V. (1995) "Shear stress and cyclic strain modulation of gene expression in vascular endothelial cells," Blood Purif 13:112-24.

[9] Chien, S., Li, S. and Shyy, Y.J. (1998) "Effects of mechanical forces on signal

transduction and gene expression in endothelial cells," Hypertension 31:162-9.

[10] Joung, I.S., Iwamoto, M.N., Shiu, Y.T. and Quam, C.T. (2006) "Cyclic strain modulates tubulogenesis of endothelial cells in a 3D tissue culture model," Microvasc Res 71:1-11.

[11] Ives, C.L., Eskin, S.G. and McIntire, L.V. (1986) "Mechanical effects on endothelial cell morphology: In vitro assessment," In Vitro Cell Dev Biol 22:500-7.

[12] Deroanne, C.F., Lapiere, C.M. and Nusgens, B.V. (2001) "In vitro tubulogenesis of endothelial cells by relaxation of the coupling extracellular matrix-cytoskeleton," Cardiovasc Res 49:647-58.

[13] Vernon, R.B. and Sage, E.H. (1999) "A novel, quantitative model for study of endothelial cell migration and sprout formation within three-dimensional collagen matrices," Microvasc Res 57:118-33.

[14] Jalali, S., del Pozo, M.A., Chen, K., Miao, H., Li, Y., Schwartz, M.A., Shyy, J.Y. and Chien, S. (2001) "Integrin-mediated mechanotransduction requires its dynamic interaction with specific extracellular matrix (ECM) ligands," Proc Natl Acad Sci U S A 98:1042-6.

[15] Manoussaki, D., Lubkin, S.R., Vernon, R.B. and Murray, J.D. (1996) "A mechanical model for the formation of vascular networks in vitro," Acta biotheoretica 44:271-282.

[16] Krishnan, L., Hoying, J.B., Nguyen, H., Song, H. and Weiss, J.A. (2007) "Interaction of angiogenic microvessels with the extracellular matrix," Am J Physiol Heart Circ Physiol 293:H3650-8.

[17] Krishnan, L., Hoying, J.B., Das, R. and Weiss, J.A. (2003) "Alterations in the material properties of collagen by angiogenesis," Proc 49th Annual Orthopaedic Research Society Meeting 28:278.

[18] Krishnan, L., Ngyuen, H., Song, H., Hoying, J.B. and Weiss, J.A. (2005) "Gene expression in a three-dimensional model of angiogenesis: Relation to matrix mechanical properties," Proc ASME Summer Bioengineering Conference abstract #b0290109, Vail, CO, June 22-26.

[19] Krishnan, L., Utzinger, U., Maas, S.A., Reese, S.P., Weiss, J.A., Williams, S.K. and Hoying, J.B. (2009) "Extacellular matrix stiffness modulates microvascular morphology during early sprouting angiogenesis in vitro," Proceedings of the ASME Summer Bioengineering Conference SBC2009: 206782.

[20] Hoying, J., Boswell, C. and Williams, S. (1996) "Angiogenic potential of microvessel fragments established in three-dimensional collagen gels," In Vitro Cell Dev Biol Anim 32:409-19.

[21] Shepherd, B., Chen, H., Smith, C., Gruionu, G., Williams, S., and Hoying, J. (2004) "Rapid perfusion and network remodeling in microvascular construct after implantation," Arterioscler Throm Vasc Biol 24: 898 - 904.

[22] Chaplain, M.A. (2000) "Mathematical modelling of angiogenesis," J Neurooncol 50:37-51.

[23] Namy, P., Ohayon, J. and Tracqui, P. (2004) "Critical conditions for pattern formation and in vitro tubulogenesis driven by cellular traction fields," J Theor Biol 227:103-20.

[24] Bauer, A.L. (2007) "A cell-based model exhibiting branching and anastomosis during tumor-induced angiogenesis," Biophys J BioFAST 92:3105-3121.

[25] Capasso, V., Micheletti, A. and Morale, D. (2008) "Stochastic geometric models, and related statistical issues in tumour-induced angiogenesis," Math Biosci 214:20-31.

[26] Mantzaris, N.V., Webb, S. and Othmer, H.G. (2004) "Mathematical modeling of tumor-induced angiogenesis," J Math Biol 49:111-87.

[27] Qutub, A.A. and Popel, A.S. (2009) "Elongation, proliferation & migration differentiate endothelial cell phenotypes and determine capillary sprouting," BMC Syst Biol 3:13.

[28] Sulsky, D., Zhou, S. and Schreyer, H.L. (1995) "Application of a particle-in-cell method to solid mechanics," Computer Physics Communications 87:236-252.

[29] Sulsky, D., Chen, Z. and Schreyer, H.L. (1994) "A particle method for history dependent materials," Computer Methods in Applied Mechanics and Engineering 118:179-196.

[30] Guilkey, J.E., Hoying, J.B. and Weiss, J.A. (2006) "Computational modeling of multicellular constructs with the material point method," J Biomech 39:2074-86.

[31] Guilkey, J.E., Hoying, J.B. and Weiss, J.A. (2005) "Large-scale modeling of the mechanical behavior of multicellular constructs," Proc ASME Summer Bioengineering Conference, Vail, CO, June 22 - 26.

[32] Bottenstein, J.E. and Sato, G.H. (1979) "Growth of a rat neuroblastoma cell line in serum-free supplemented medium," Proc Natl Acad Sci U S A 76:514-7.

[33] Liu, Y., Griffith, M., Watsky, M.A., Forrester, J.V., Kuffova, L., Grant, D., Merrett, K. and Carlsson, D.J. (2006) "Properties of porcine and recombinant human collagen matrices for optically clear tissue engineering applications," Biomacromolecules 7:1819-28.

[34] WinFiber3D, available at http://mrl.sci.utah.edu/

[35] Pourdeyhimi, B., Dent, R. and Davis, H. (1997) "Measuring fiber orientation in nonwovens Part III: Fourier transform," Textile Res J 67:143-151.

[36] Sander, E.A. and Barocas, V.H. (2009) "Comparison of 2D fiber network orientation measurement methods," J Biomed Mater Res A 88:322-31.

[37] Assoian, R.K., Komoriya, A., Meyers, C.A., Miller, D.M. and Sporn, M.B. (1983) "Transforming growth factor-beta in human platelets. Identification of a major storage site, purification, and characterization," J Biol Chem 258:7155-60.

[38] Roberts, A.B., Sporn, M.B., Assoian, R.K., Smith, J.M., Roche, N.S., Wakefield, L.M., Heine, U.I., Liotta, L.A., Falanga, V., Kehrl, J.H. and et al. (1986) "Transforming growth factor type beta: Rapid induction of fibrosis and angiogenesis in vivo and stimulation of collagen formation in vitro," Proc Natl Acad Sci U S A 83:4167-71.

CHAPTER 4

EXTRACELLULAR MATRIX DENSITY REGULATES THE RATE OF NEOVESSEL GROWTH AND BRANCHING IN SPROUTING ANGIOGENESIS*

4.1 Abstract

Angiogenesis is regulated by the local microenvironment, including the mechanical interactions between neovessel sprouts and the extracellular matrix (ECM). However, the mechanisms controlling the relationship of mechanical and biophysical properties of the ECM to neovessel growth during sprouting angiogenesis are just beginning to be understood. In this research, we characterized the relationship between matrix density and microvascular topology in an *in vitro* 3D organ culture model of sprouting angiogenesis. We used these results to design and calibrate a computational growth model to demonstrate how changes in individual neovessel behavior produce the changes in vascular topology that were observed experimentally. Vascularized gels with higher collagen densities produced neovasculatures with shorter vessel lengths, less branch points, and reduced network interconnectivity. The computational model was able to predict these experimental results by scaling the rates of neovessel growth

* Accepted for publication, Edgar, L.T., Underwood, C.J., Guilkey, C.J., Hoying, J.B., and J.A. Weiss, "Extracellular matrix density regulates the rate of neovessel growth and branching in sprouting angiogenesis," *PLOS One*, 2013.

and branching according to local matrix density. As a final demonstration of utility of the modeling framework, we used our growth model to predict several scenarios of practical interest that could not be investigated experimentally using the organ culture model. Increasing the density of the ECM significantly reduced angiogenesis and network formation within a 3D organ culture model of angiogenesis. Increasing the density of the matrix increases the stiffness of the ECM, changing how neovessels are able to deform and remodel their surroundings. The computational framework outlined in this study was capable of predicting this observed experimental behavior by adjusting neovessel growth rate and branching probability according to local ECM density, demonstrating that altering the stiffness of the ECM via increasing matrix density affects neovessel behavior, thereby regulated vascular topology during angiogenesis.

4.2 Introduction

Angiogenesis is the generation of new vascular elements from existing vasculature. During angiogenesis, sprouting endothelial cells degrade the basement membrane with matrix metalloproteinases (MMPs) [1,2] and apply traction to and migrate along components of the extracellular matrix (ECM) [3], resulting in neovessel elongation. Previous studies have demonstrated that the mechanical interaction between neovessel sprouts and the ECM regulate the topology of vascular networks formed during angiogenesis [4-7]. Cellular traction forces applied to the ECM create a deformation that cells can detect [8-10]. The nature of this deformation is determined by the material properties of the matrix, such as fibril orientation and density, as well as geometry and boundary conditions. In previous studies, we explored the relationship

between angiogenesis and the mechanical properties of the ECM using a 3D organ culture model of microvessel fragments within a type-I collagen gel [11-14]. In this model of sprouting angiogenesis, neovessels sprouting from whole microvessels cultured in a 3D gel, that was free to contract in all directions, grow into a randomly oriented network [12-14]. When contraction was prevented along the long-axis of rectangular gels, neovessels and collagen fibrils were aligned parallel to the constrained axis [13,14].

In addition to the effects of mechanical boundary conditions, ECM matrix density has been shown to influence formation of capillary structures in various *in vitro* models of angiogenesis. Several studies utilizing endothelial cell-based culture models of angiogenesis have shown that increasing the density of the matrix reduces capillary outgrowth and network formation [15-20]. However, all of these studies involved models of outgrowth from isolated endothelial cells. In contrast, our microvessel organ culture model of angiogenesis is based on intact microvessels and includes multicellular interactions between vascular cells (endothelial and mural cells) and the nascent matrices (basement membrane and stroma). Additionally, previous studies only reported the effect of matrix density increase using quantitative data measured over the capillary network and as a result were only able to report global changes to the topology of the network. As a result, these studies were not able to establish a strong connection between their global experimental observations and local cellular behavior.

Experimental cell and organ culture models of angiogenesis typically provide morphometric data that are obtained by averaging information about the entire culture, at a single time point. This makes it difficult to establish a relationship between local

cellular behavior and global characteristics of the biological system. Computational models can supplement and enhance the interpretation of experimental results, and are commonly utilized within the field of angiogenesis research [21]. Recently, we developed a computational model of angiogenesis that uses the orientation of ECM fibrils to determine the direction of microvessel growth and produced validated predictions of global morphometric data when compared to *in vitro* vascular networks [22]. The goal of this research was to extend and apply this model to characterize the response of angiogenic microvessels to changes in matrix density, using a combined experimental and computational approach. First, we performed experiments using our 3D angiogenesis model with different type-I collagen densities to characterize the relationship between vascular topology and matrix density. Second, we used our experimental data to design and calibrate new features within our growth model to describe how neovessels respond to a change in matrix density. Finally, we demonstrated how this response leads to the changes in vascular topology that we found.

4.3 Methods

4.3.1 *In vitro* model of angiogenesis

3D vascularized constructs served as a model of *in vitro* angiogenesis and were prepared using methods described previously [11]. Constructs consisted of microvessel fragments isolated from rat epididymal fat pads, resuspended and polymerized in 3D collagen gels (Figure 4.1). The microvessel fragments retain the associated stromal cells and basement membrane after isolation and seeding, providing an "organ culture"

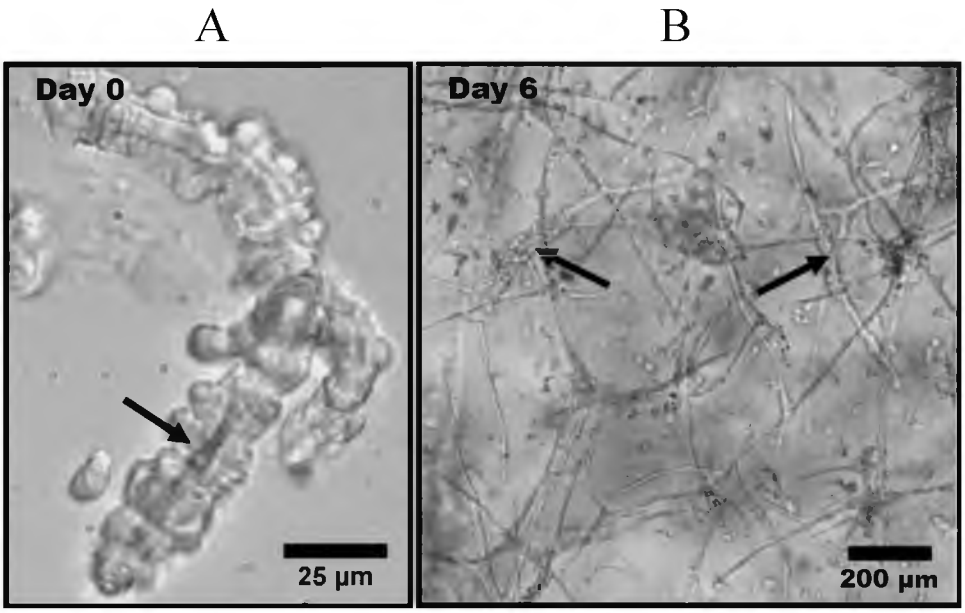

Figure 4.1: Phase contrast light micrographs of rat microvessel fragments. (A) Isolated microvessel fragment at Day 0 with a visible lumen, indicated by the arrow. (B) Angiogenic microvessel fragments within a type I collagen gel at Day 6 of growth. The thicker initial fragments are indicated by the arrows. The thinner protrusions extending from the initial fragments are neovessels formed through angiogenesis.

model of angiogenesis. Previous studies have extensively characterized angiogenesis in these vascularized constructs [11-13,23-27]. Sprouting of neovessel tips occurs spontaneously and predictably, with the first evidence of sprout tips usually observed by the second day of culture.

All reagents were obtained from Invitrogen (Carlsbad, CA) unless otherwise indicated. Epididymal fat pads were harvested from male retired breeder Sprague-Dawley rats. This protocol was approved by the University of Utah Institutional Animal Care and Use Committee (Protocol Number: 11-02018). Fat pads were minced and subjected to partial digestion with 2.0 mg/ml Clostridium collagenase (Worthington Biochemicals, Lakewood, NJ). After 4 minutes, digestion was halted by the addition of Leibowitz (L-15) media and the solution was centrifuged. The pellet was washed, resuspended in media, and filtered through 350 μm and 30 μm sterile nylon filters sequentially. The filtration step removes undigested debris, single cells, and small fragments resulting in a population of microvessel fragments within a controllable range of sizes. At 35,000 per ml, vessel fragments were suspended within liquid type-I collagen solution (BD Biosciences, Bedford, MA) prepared at concentrations of 2.0, 3.0, or 4.0 mg/ml. For each of the three collagen solutions, 0.5 ml was transferred to a circular culture well (Nunc – Thermo Fisher Scientific, Rochester, NY, diameter = 15 mm) and allowed to polymerize into a 3D gel (n = 4 gels per collagen concentration investigated, N = 12 gels total). These gels were free-floating within the culture chambers with initial dimensions of 15 mm diameter and 2.8 mm thick.

Serum-free growth media [28] was supplemented with 10.0 ng/ml rhVEGF (PeproTech, Rocky Hill, NJ) and provided to the cultures at Day 0. Media was changed

every 2 days and replaced with 0.8 ml of fresh media. After Day 6 of culture, the gels were fixed with 1.0 ml of 4% paraformaldehyde for 24 hours. Gels were then placed in a solution of 1x phosphate-buffered saline (DCF-PBS, pH 7.4) and 2.0 μg/ml Isolectin IB4-Alexa 488 to fluorescently label endothelial cells in preparation for confocal microscopy.

4.3.2 Confocal microscopy and skeletonization of vascular networks

3D image data were collected from each vascularized construct by confocal microscopy using methods described previously [12,13]. Six adjacent stacks at the geometric center of each gel were captured with an Olympus FV1000 microscope using a 10x objective and 488 nm laser. Each stack was captured at a resolution of 512 x 512 pixels and was acquired to a depth of 200 μm at 2.5 μm intervals. A 2 x 3 mosaic was created from the six stacks using a custom software application, resulting in an image dataset that represented a 3.8 x 2.5 x 0.2 mm region of the vascularized gel (Figure 4.2 A). Processing and skeletonization of 3D confocal data was performed using the Amira^{TM} software (Mercury Computer Systems, Carlsbad, CA). Mosaic stacks were subjected to a deconvolution routine to reduce out-of-plane blur through the depth of the dataset (numerical aperture = 0.4, wavelength = 520 nm, refractive index of collagen = 1.35 [29]). A threshold value was calculated by fitting a Gaussian distribution to the image histogram, and this value was used in the automated skeletonization routine within Amira to decompose images of vessels down to a collection of line segments (Figure 4.2 B). A custom software application was used to analyze the skeletonized vessel data and to collect the desired morphometric data [30]. The image data of the

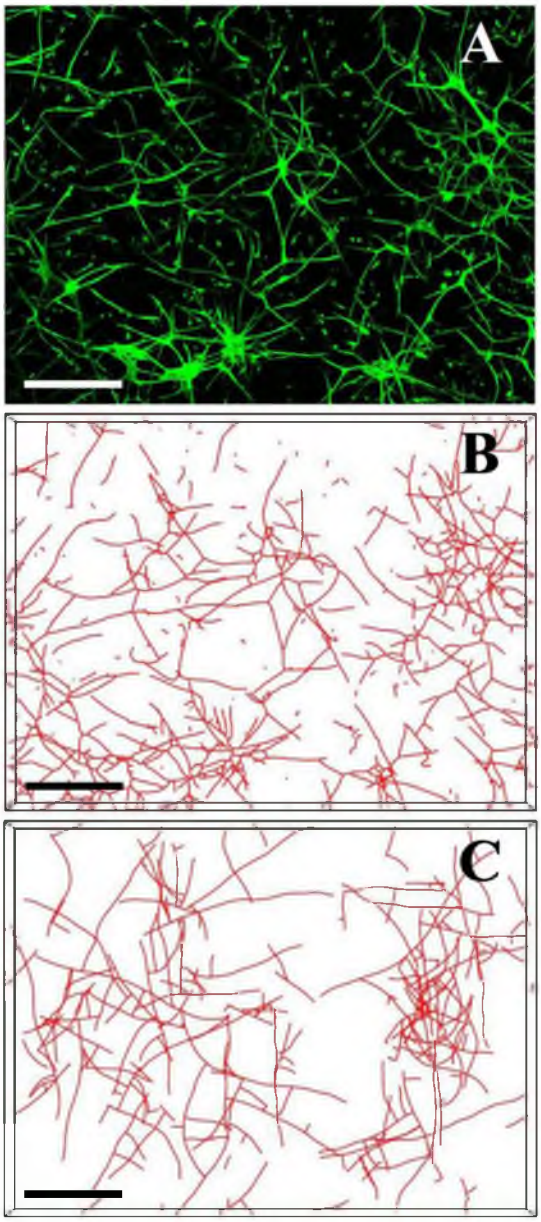

Figure 4.2: Visualization of *in vitro* experiments and simulation results. The computational model was designed to simulate angiogenic outgrowth and neovascularization within 3D organ culture of microvessel fragments with a type-I collagen gel. All images in this figure depict the 3.8 × 2.5 × 0.2 mm imaged during the experiments. (A) Z-projection mosaic of 3D confocal image data showing microvessels cultured in a 3.0 mg/ml collagen gel after Day 6 of culture. Endothelial cells within the culture were labeled with Isolectin IB4-Alexa 488 and imaged using a confocal microscope with a 10x objective. (B) Skeletonized vessel data obtained from the confocal image data of a vascularized collagen gel in Panel A. (C) Results of a simulation using the computational model. Microvessels were represented as a collection of line segments, and growth was simulated by the addition of new segments to the free ends of existing segments. (Scale bar = 350 μm).

vascularized constructs were analyzed to determine the total vascular length, the degree of network interconnectivity, the number of branching points, and the number of end points.

The collective length of all microvessels within the imaged domain was defined as the total vascular length. This morphometric measurement can also be interpreted as the contour length of the network, and it is a useful metric of overall angiogenic outgrowth during the culture period [12,13]. Neovessels sprouting from parent fragments were observed to form continuous vascular networks, with intervessel connections presumably formed through anastomosis. The network interconnectivity, or the percentage of microvessels that fused into a single continuous vascular network, was calculated by measuring the length of the longest continuous microvessel tree and normalizing by the total vascular length. A branching point was defined as a node connected to three different line segments and indicates either a new vessel sprout (branching) or two separate vessels fusing into one (anastomosis). End points were terminal ends of vessels, defined by a node that is associated with only one segment. The number of end points quantifies the amount of growth tips and characterizes the degree of branching and anastomosis occurring within the domain.

4.3.3 Computational growth model

A validated computational model of microvessel growth and 3D vessel morphology during spontaneous angiogenesis was utilized to simulate the *in vitro* experiments (Figure 4.2 C) [22]. This growth model uses information about the ECM to predict neovessel length, direction, and branching. A simulation domain corresponding to the

imaged region of each vascularized gel (3.8 × 2.5 × 0.2 mm) was fit with a regular hexahedral grid at a resolution of 6 × 6 × 2 elements. Properties of the ECM that influenced angiogenic vessel growth, such as fibril orientation and matrix density, were stored at the nodes of the grid. The model was initialized with a random collagen fibril orientation value between 0 and π radians at each node in the grid. Initial microvessel fragments were represented as line segments and were seeded at random positions and orientations throughout the domain.

At each time step, microvessel growth was simulated by creating new line segments at the positions of all active growth tips based on methods presented previously [22]. A unit vector, $\boldsymbol{\psi}_{new}$, was used to describe the direction of each new line segment. Its orientation was determined by a weighted average of the direction of the parent microvessel, represented by the unit vector $\boldsymbol{\psi}_{parent}$, and a directional component determined by the local collagen fibril orientation, represented by the unit vector $\boldsymbol{\theta}$:

$$\boldsymbol{\psi}_{new} = w_1 \boldsymbol{\psi}_{parent} + w_2 \boldsymbol{\theta}. \tag{4.1}$$

The values of w_1 = 0.91 and w_2 = 0.09 were determined based on preliminary simulations to create microvascular networks with similar morphology to those seen *in vitro*. The component of neovessel direction determined by collagen fibril guidance, $\boldsymbol{\theta}$, was interpolated using trilinear finite element shape functions through the following equation:

$$\boldsymbol{\theta}(\boldsymbol{x}) = \sum_{j=1}^{8} \boldsymbol{\theta}_j N_j(\boldsymbol{x}). \tag{4.2}$$

In Equation 4.2, $\boldsymbol{\theta}_j$ is the collagen fibril orientation value stored at node j of the grid element in which the growth tip resides. Nj is the value of the shape function for node j

at the position of the active growth tip, $\boldsymbol{x}$. The shape functions, $N(\boldsymbol{x})$, provide an interpolation scheme in which the value of the field variable at a point in the grid element is a weighted average of contributions from each node.

Branching, the sprouting of a new neovessel from an existing vessel, was modeled as a random process as per our previous publication [22]. During a time step, each segment generated a random number between 0 and 1. If the random number exceeded the branching probability, b_0, then that segment would form a branch. Similarly, the growth rule for anastomosis, the fusing of two vessels into one, followed our previous approach [22]. If a growth tip was within 25 μm of another vessel, anastomosis was simulated by creating a new line segment connecting the two points. Subsequently, all growth tips involved with the anastomosis were inactivated and stopped growing.

To introduce a sensitivity of vessel growth to matrix density, a scaling factor was calculated from experimental data by taking the average total vascular length for each culture condition (2.0, 3.0, and 4.0 mg/ml) and normalizing by the average total vascular length measured in the 3.0 mg/ml constructs. Values of the scaling factor v were then fit to a three-parameter exponential function that described how the factor changed with collagen density:

$$v = v_0 + a_0 e^{-a_1 c},\ a_1 > 0. \tag{4.3}$$

Here, v was the scaling factor, c was the collagen concentration (mg/ml), and v_0, a_0, and a_1 were parameters determined by the curve fit. An additional data point of c = 10.0 mg/ml, v = 0.0 was added to ensure that the scaling function eventually reached zero. The collagen concentration of the matrix was an input parameter to the computational model and the corresponding scaling factor was calculated using

Equation 4.3. The scaling factor was used to proportionally scale two growth mechanisms. As the density of the matrix increased, the scaling factor reduced the length of new line segments and probability of each segment forming a branch.

Simulations of the *in vitro* experiments were performed in order validate the computational framework (4 simulations per culture condition, 12 simulations total). The number of initial fragments in the simulations (N_{frag} = 70) was determined from the volume of the domain and the seeding density (35,000 fragments per ml). Growth was simulated for 6 days. The branching probability was set at 0.1, determined by minimizing the RMS error between the number of branch points in simulations and experiments at 3.0 mg/ml using methods previously described [22]. The collagen concentration used to prepare the gel experiment being simulated (2.0, 3.0, or 4.0 mg/ml) was set as an input parameter and read in by the model during initialization. For each culture condition, morphometric data from the computational simulations (total vessel length, network interconnectivity, number of branch points, and number of end points) were compared to values measured from the corresponding experimental cultures.

4.3.4 Statistical analysis

One-way ANOVAs were used to test for the effect of matrix density on all morphometric parameters for both experimental and simulation data (α = 0.05). A two-tailed Student's t-test with unequal variance (Welch's t-test) was then performed between experimental and computational morphometric data for each matrix density to detect any statistical difference (α = 0.05). If a statistical difference could not be

detected, a TOST-test (two one-sided t-test [31]) was performed to test for statistical equivalence ($\alpha = 0.05$, $\Theta = 0.3$).

4.3.5 Predictive simulations

Single cell experiments involving micropatterned ECM have been useful in studying the role of haptotaxis (guidance by ligand availability) and durotaxis (guidance by substrate stiffness/deformability) in cell migration. Similar experiments involving tailored ECM density fields would prove useful in studying the mechanical regulation of angiogenesis. However, our organ culture method involves encapsulating microvessel fragments within a collagen gel, preventing us from growing these vessels in 3D prefabricated matrices. However, our computational framework can be used to predict the results of the type of experiments that we cannot perform using our current culture method. As a final demonstration of utility of the modeling framework, we used our growth model to predict several scenarios of practical interest that could not be investigated experimentally.

In the first predictive simulation, a density gradient was created within the simulation domain (7.6 × 5.1 × 0.4 mm). The gradient ran along the longest axis of the domain (x-axis) from 1.0 mg/ml at the left edge to 10.0 mg/ml at the right edge. Matrix density was uniform along the other two directions. This simulation demonstrates how angiogenic growth changes as neovessel grow up or down a stiffness gradient. In the second predictive simulation, a cylindrical plug (radius = 1.5 mm) composed of acellular 10.0 mg/ml collagen was placed in the center of the domain. The remaining domain was initialized at 3.0 mg/ml and seeded with vessels. This simulation

demonstrates how neovessels respond to a stiff interface as they encounter the acellular plug. The final predictive simulation demonstrates how vasculature can be aligned along a chosen direction by growing neovessels within two 1000 μm channels of 3.0 mg/ml collagen running along the x-axis of the domain. The density outside the channels was set to 8.0 mg/ml. Vessels were seeded within the channels only. In all three of the predictive simulations, vessels were seeded at a density of 10,000 fragments per ml and growth was simulated until Day 6.

4.4 Results

4.4.1 Experimental results

Angiogenic sprouting and neovessel outgrowth was consistent across all microvessel cultures. A well-established microvasculature was observed at Day 6 for all matrix density conditions. The circular gels experienced significant contraction during the 6-day culture period, with construct diameters reduced by an average of 40.0 ± 5.0%, 20.0 ± 5.0%, and 7.0 ± 1.0% for 2.0, 3.0, and 4.0 mg/ml gels, respectively (average ± std dev). Qualitatively, the highest levels of angiogenic growth occurred in the 2.0 mg/ml constructs, while growth within the 4.0 mg/ml constructs appeared considerably reduced (Figure 4.3 A-C).

Measurements of total vascular length within the vascularized constructs indicated a reduction in overall neovessel outgrowth as the density of the matrix was increased (Figure 4.4 A black) (ANOVA, $p < 0.05$). Although we did not measure the initial total vascular length in these experiments, data from a previously published study [32] allows us to approximate the initial total vascular length for these cultures at 2.7 cm.

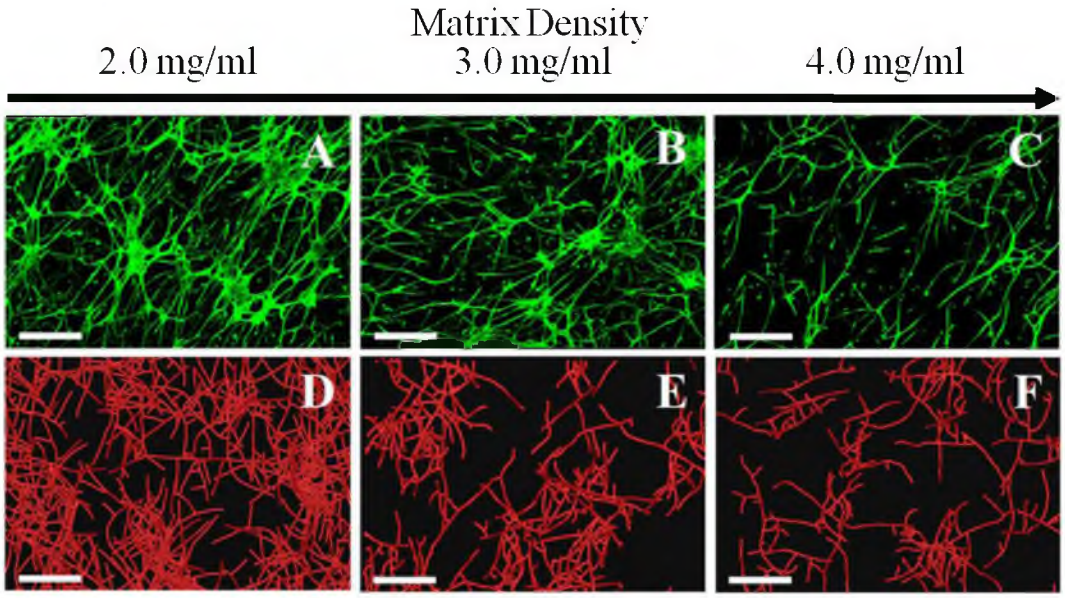

Figure 4.3: Microvasculatures observed at different levels of collagen density. Increasing the density of the ECM reduced neovascularization in both the experiments and computational simulations. Top Row: Z-projection mosaic of 3D confocal image data showing vascularized collagen gels taken at Day 6 of growth. Bottom Row: Results of the comparable computational simulations, presented as 3D volume-renderings of the line segment data. The three levels of collagen density assessed in this study were: 2.0 mg/ml (A, D), 3.0 mg/ml (B, E), and 4.0 mg/ml (C, F). (Scale bar = 350 μm).

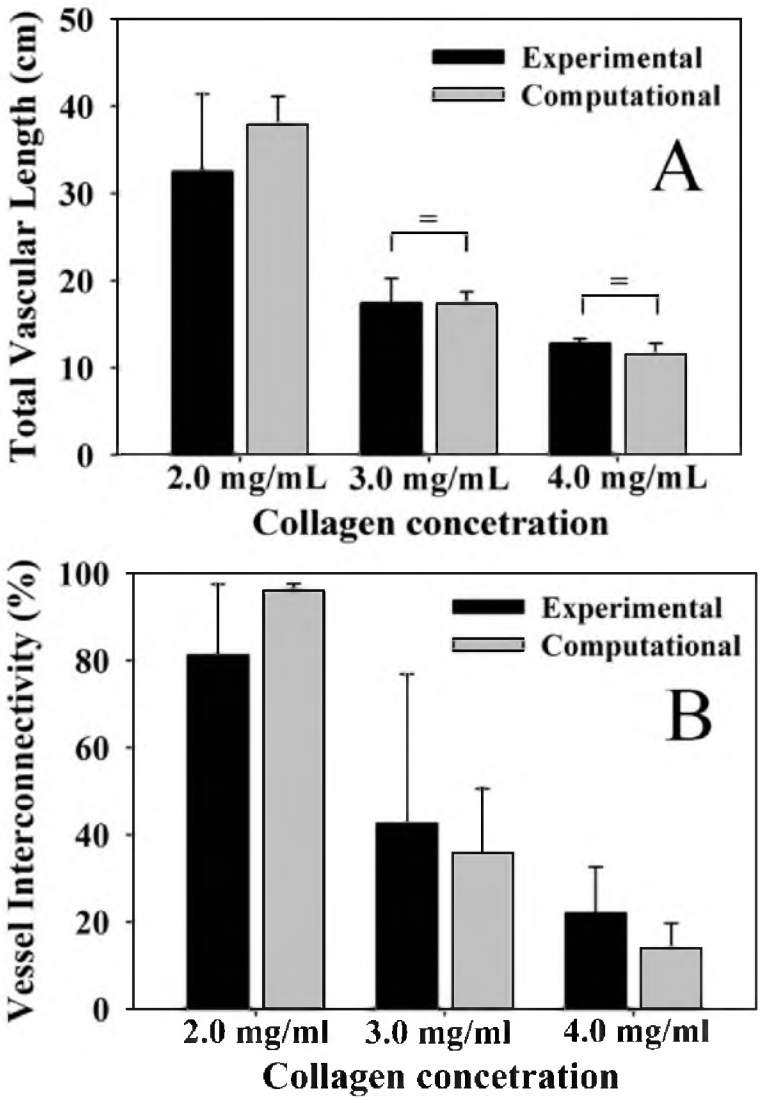

Figure 4.4: Total vascular length and network interconnectivity. (A) The total vascular length decreased as matrix density increased. Measurements from the experimental cultures are presented in black and predictions from the computational model are presented in gray. (B) Vessel interconnectivity, a measure of the percentage of microvessels within the domain that are connected into the largest continuous vascular network, decreased as a function of matrix density, indicating a reduction in network formation. No statistical difference was detected between any experimental and computational morphometric at each matrix density level by T-test. Statistical equivalence as detected by a TOST-test is indicated by the bracket and equal sign.

This allows us to determine that over the 6 days of culture, total vascular length experienced roughly an 11-fold, a 6-fold, and a 4-fold increase in the 2.0, 3.0, and 4.0 mg/ml gel experiments, respectively. There was a significant decrease in network connectivity as the matrix density increased (Figure 4.4 B black) (ANOVA, $p < 0.05$), indicating that increased density of the matrix results in a more discontinuous vascular network.

Other angiogenic neovessel behaviors, such as branching and anastomosis, were characterized by measuring the number of branch points and end points within the vascularized constructs. At Day 6 of culture, there was a significant decrease in the number of branch points and end points as the collagen density increased (data not shown). Since increased contraction of low-density gels could lead to increased branch points and end points within an imaged volume, branch point and end point data were normalized by total vascular length to express these measurements per unit length of growth. As the density of the matrix increased, microvessels formed significantly less branch points per unit length of growth (Figure 4.5 A black) (ANOVA, $p < 0.05$). The amount of free ends per unit length increased significantly as matrix density increased (Figure 4.5 B black) (ANOVA, $P < 0.05$).

4.4.2 Computational results

Qualitative comparison of 3D volumetric confocal image data with the 3D renderings of simulated microvessel growth demonstrated that the computational growth model provided reasonable and realistic descriptions of the experimental data for all matrix densities (Figure 4.3 D-F). The three-parameter exponential function

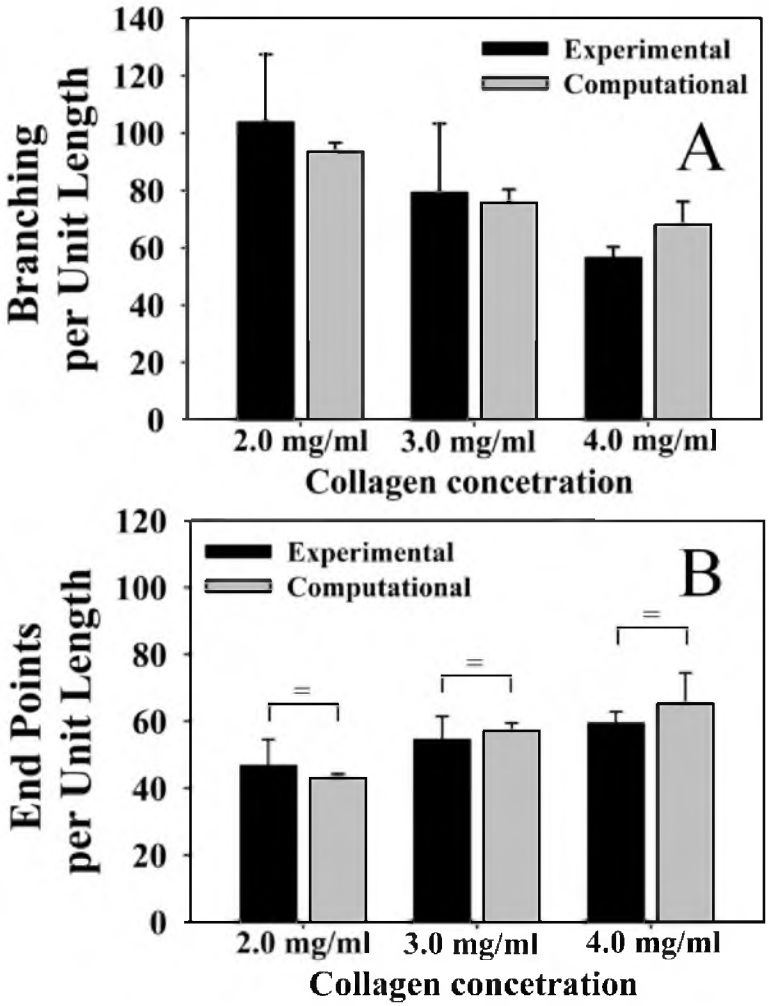

Figure 4.5: Branch points and free ends per unit length. A branching point was defined as any node that connected to three or more vessel segments. Branching points were created by either a new vessel sprout (branching) or two separate vessels fusing into one (anastomosis). Measurements from the experimental cultures are presented in black and predictions from the computational model are presented in gray. (A) The number of branch points was normalized by the total vascular length in order to isolate the tendency of microvessels to form a branch point per unit length of growth. Branching per unit length was observed to decrease as matrix density was increased. An end point was defined as a node that was associated with only one vessel segment and represents the terminal end of a vessel. Measurements from the experimental cultures are presented in black and predictions from the computational model are presented in gray. (B) Normalizing the number of end points by the total vascular length revealed that the number of free ends per unit length increased along with matrix density. No statistical difference was detected between any experimental and computational morphometric at each matrix density level by T-test. Statistical equivalence as detected by a TOST-test is indicated by the bracket and equal sign.

(Equation 4.3) provided an excellent fit of the experimental data (R^2 = 0.99) (Figure 4.6). The parameters determined by this curve fit were v_0 = -0.16, a_0 = 5.1605, and a_1 = 0.5112. Thus, the inclusion of density-dependent growth and branching resulted in distinct qualitative differences for simulations of angiogenesis across the different matrix density conditions.

The computational model accurately predicted the quantitative morphometric measurements of the vascularized constructs as a function of matrix density. As with the experimental results, simulations predicted a significant reduction in total vascular length as density of the matrix increased (Figure 4.4 A grey) (ANOVA, $p < 0.05$). Microvasculature predicted by the growth model became increasingly discontinuous as matrix density increased, similar to the trend seen *in vitro* (Figure 4.4 B grey) (ANOVA, $p < 0.05$). As the density of the matrix increased, the computational simulations predicted reduced branching per unit length (Figure 4.5 A grey) (ANOVA, $p < 0.05$). Measurements of end points per unit length increased along with matrix density in the simulations (Figure 4.5 B grey). No statistical difference was detected between any experimental and computational morphometric at each matrix density level by T-test. Additionally, 8 out of the 18 combinations of morphometrics and matrix density passed a TOST-test for statistical equivalence between experimental and computational data: total length at 3.0 and 4.0 mg/ml, branch points at 4.0 mg/ml, end points at 3.0 and 4.0 mg/ml, and normalized end points at 2.0, 3.0, and 4.0 mg/ml ($p < 0.05$).

In the predictive simulation involving the density gradient, there were high amounts of neovascularization within the low density portions of the gel while growth within the

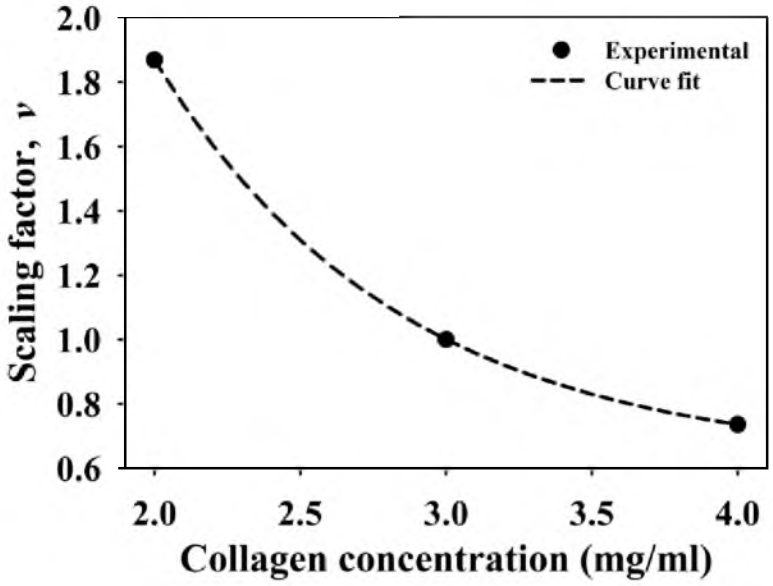

Figure 4.6: Matrix density scaling factor. A scaling factor was calculated from experimental data and used to scale growth rate and branching probability within the computational model based on local ECM density. The factor was calculated by taking the average total vascular length measured for the 2.0, 3.0, and 4.0 mg/ml vascularized constructs and normalizing by the total vascular length for the 3.0 mg/ml construct. Experimental data is presented as the solid points on the graph. These data were then fit to the exponential function described in Equation 3.3 ($R^2 = 1.0$). The fitted function is presented as the dashed line on the graph.

higher density regions was severely reduced (Figure 4.7). Neovessels growing down the density gradient (i.e., towards the 1.0 mg/ml region) experienced an increased growth rate and were able to vascularize the gel more effectively. The growth rate of vessels growing up the density gradient (i.e., towards the 10.0 mg/ml region) was severely reduced compared to vessels growing the other direction, and there was very little neovascularization in the high density portion of the gel. In the density plug simulation, vessels were not able to grow into the high density plug, leaving this region of the domain vessel-free while the remainder of the domain became highly vascularized (Figure 4.8). The results were similar in the microchannel simulation. The 3.0 mg/ml microchannels were highly vascularized, but very little growth occurred within the regions outside the channels (Figure 4.9). Due to the narrow aspect ratio of the microchannels, the resulting microvasculature was aligned along the direction of the channels.

4.5 Discussion

In our experiments, we found that increases in matrix density significantly limited angiogenesis (Figure 4.3). Networks cultured in high density matrix had a shorter contour length after the 6 day culture period (Figure 4.4 A black), suggesting that increased matrix density decreases neovessel growth rate. Additionally, networks cultured in high density matrix were less divergent than their lower-density counterparts as indicated by a reduction in the number of branch points formed per unit length of growth (Figure 4.5 A black), suggesting that new sprouts were forming at a slower rate. Finally, an increase in matrix density also resulted in an increase in the number of free

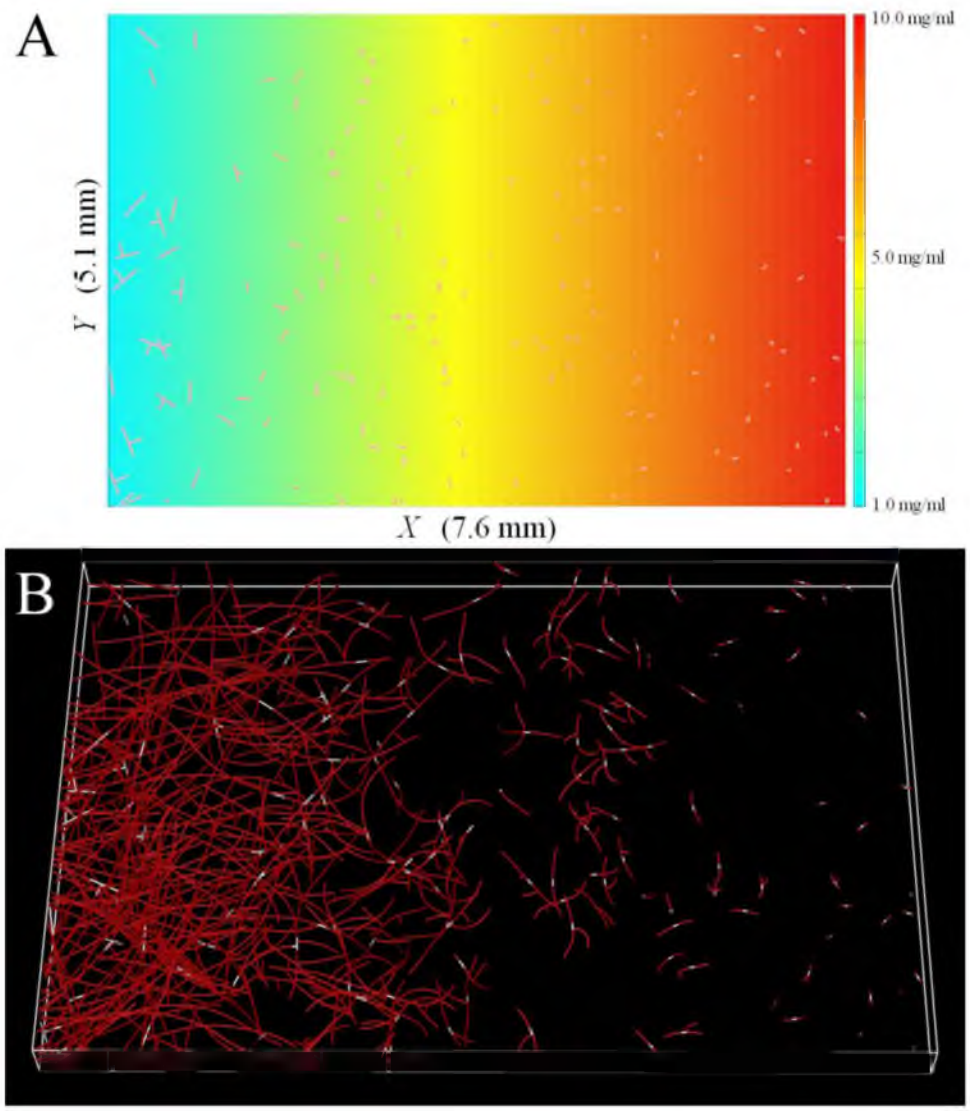

Figure 4.7: Predictive simulation of angiogenesis within a density gradient. In this simulation, matrix density runs from 1.0 mg/ml to 10.0 mg/ml along the horizontal axis (x-axis) while remaining uniform along the other two directions. (A) Z-projection of the matrix density field and the initial microvessel fragments. (B) Growth at Day 6. Initial microvessel fragments are shown in white. The computational framework predicted high amounts of neovascularization in the low density portion of the domain. Growth significantly reduced as density increased along the *x*-axis. Additionally, vessels that grew towards the low density regions grew at a faster rate than vessels growing towards the high density regions.

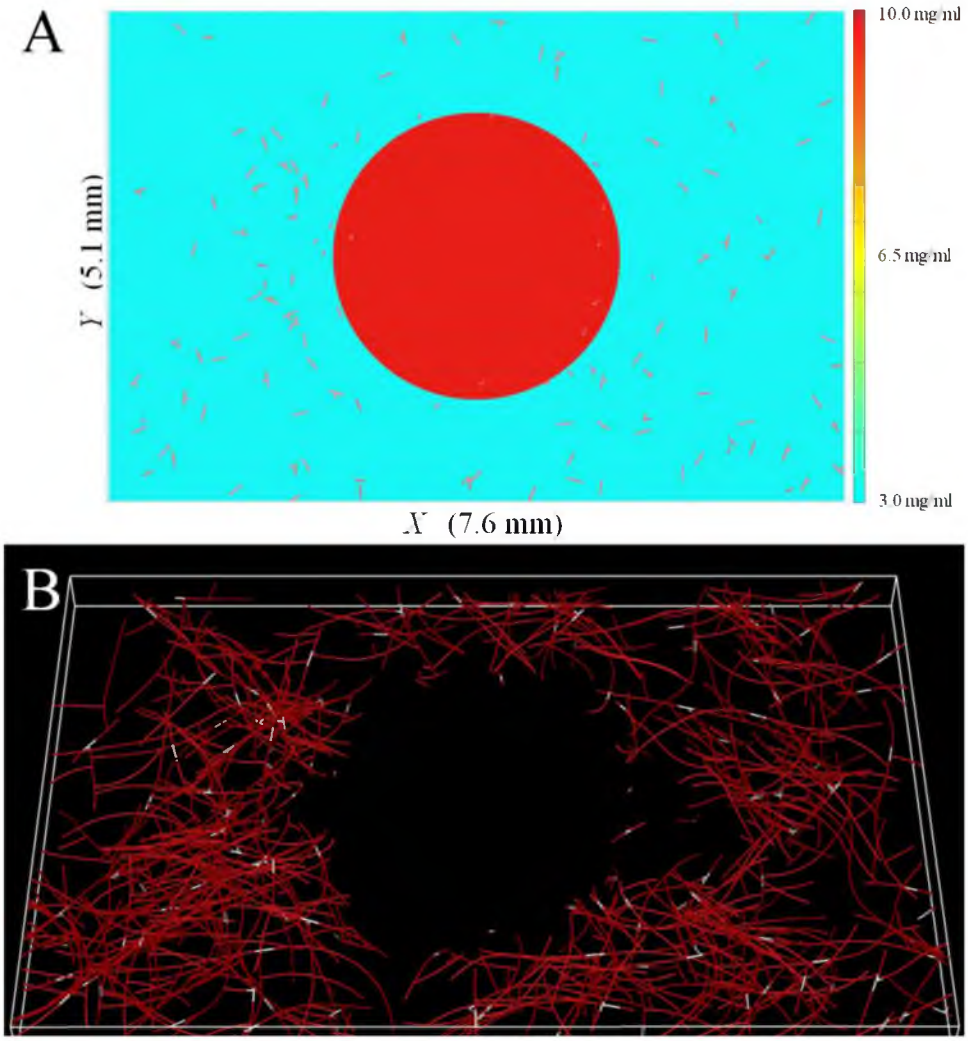

Figure 4.8: Predictive simulation: High-density cylindrical plug. (A) Z-projection of the matrix density field and the initial microvessel fragments. In this simulation, a 1.5 mm radius plug of 10.0 mg/ml acellular collagen was placed at the center of the domain. Vessels were seeded within the 3.0 mg/ml region outside of the plug. (B) Growth at Day 6. Initial microvessel fragments are shown in white. There were high amounts of neovascularization within the regions surrounding the plug, but vessels that encountered the high-density plug were unable to grow any further. As a result, the plug region remained vessel-free.

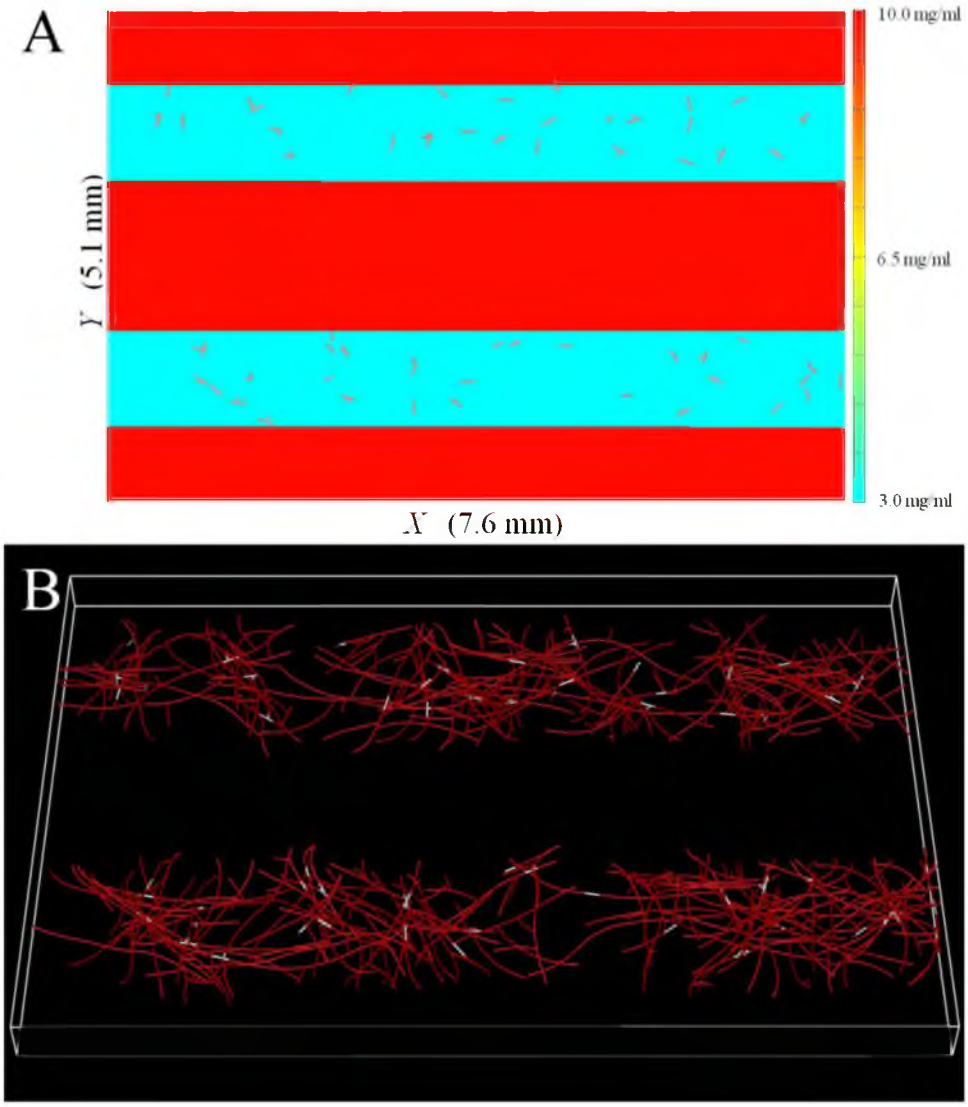

Figure 4.9: Predictive simulation: Vascularized microchannels. (A) Z-projection of the matrix density field and the initial microvessel fragments. (B) Growth at Day 6. Initial microvessel fragments are shown in white. In this simulation, two 1000 μm microchannels of 3.0 mg/ml collagen seeded with vessels were set up along the *x*-axis. During the simulation, the microchannels became highly vascularized but little growth occurred once the vessels left the channel. As a result, vasculature became aligned along channels as vessels growing along the channel grew at an increased rate.

ends per unit length (Figure 4.5 B black). Thus, as the density of the matrix increased, the observation of increased free ends despite a decreased amount of branching suggests that anastomosis occurred less frequently. This may be due to the fact that a slower growth rate reduces the chance of a neovessel finding a potential vessel for anastomosis, resulting in poor network formation (Figure 4.4 B black). Orientation data from simulations of the anisotropic ECM condition correlated well with microvessel orientation observed in the fixed-edge vascularized constructs. However, angle data from the simulations tended to favor the acute angle bins more than the corresponding experimental data. Approximately 90% of microvessels from the simulations were found orientated between 0° and 45° off of the constrained axis. Only 80% of microvessels within the fixed-edge constructs fell within this same range. Although this difference is seemingly trivial, it is important to account for all inconsistencies between the model and *in vitro* findings. This particular inconsistency is important since the cornerstone assumption for this simulation framework is that microvessel growth follows collagen fiber orientation.

Our computational model was capable of accurately predicting microvascular network topology as a function of initial ECM density. As the density of the matrix was increased, the computational model predicted neovasculatures with shorter contour lengths, reduced branching per unit length, more free ends per unit length, and reduced connectivity (Figures 4.4, 4.5). For all cases, no statistical difference could be detected between morphometric data from the experiments and computational simulations at a given level of matrix density by t-test. Almost half of the morphometric-matrix density combinations tested positive for statistical equivalence, and many of the p-values were

under 10% even if equivalence was not found. Additionally, in almost all cases, the computational mean was within one standard deviation of the experimental mean. These results demonstrate that the computational model was capable of making similar predictions when compared to the experiments across matrix density for all morphometrics, even if statistical equivalence was not found in each case. It should be noted that although our sample number produced high statistical power for the ANOVA tests, post hoc analysis revealed that the power of the T-tests at this sample number was low (less than 80%) and the number of experiments required to reach a power of 80% is very high in most cases and outside the practical limitations of the study. However, despite these limitations in the statistical analysis, the level of similarity between experimental and computational data presented here satisfies the objectives of the study.

It is instructive to examine the results of this study using an organ culture model of angiogenesis in the context of other studies that have examined the effect of changes in matrix density on morphogenesis of endothelial cell culture models. These cell culture models included HUVECs (human umbilical vein endothelial cells) within a type-I collagen matrix [18], HUVEC-coated microbeads within a fibrin matrix [15-17], BPMECs (bovine pulmonary microvascular endothelial cells) cultured on a collagen substrate [19], and BAECs (bovine aortic endothelial cells) cultured on compliant polyacrylamide substrates functionalized with type-I collagen [20]. In all of these studies, increasing the density of the matrix significantly reduced outgrowth and network formation. The organ culture model used in our study differs from the experimental models in previous studies. Microvessel fragments consisting of endothelial cells, pericytes, and basement membrane where cultured in a collagen

matrix as opposed to isolated endothelial cells. An advantage of our *in vitro* organ culture model is that it includes multicellular signaling and organization and neovessels with stromal cells. However, a weakness of this system is that it is more complicated, which makes it more difficult to isolate contributing factors compared to single cell models. We found similar results to studies with cell culture models in that increasing matrix density reduced angiogenic outgrowth and neovascularization. Vessel fragments are able to form continuous vascular networks resembling *in vivo* microvasculature during culture. This allowed us to analyze the relationship between matrix density and morphometric features of vascular networks during angiogenesis that not typically analyzed in simpler cell culture models, such as branch points and free ends per unit length of growth and network interconnectivity. We also designed and implemented a computational model capable at simulating the organ culture experiments, and we applied this modeling framework to predict other experiments. For example, the method of encapsulating vessel fragments within a collagen matrix would not allow us to culture angiogenic microvessels within a prefabricated gradient of matrix density, but we can simulate that experiment (Figure 4.7). This simulation predicted a large amount of neovascularization in the low density portions of the domain, and vascularization decreased as density increased along the direction of the gradient.

Our computational results obtained by scaling the rate of growth and branch formation suggests that matrix density alone can regulate the topology of the vascular network by controlling these two aspects of angiogenesis. As we increased the concentration of collagen monomer in our experiments, we created matrices with increased fibril density, more inter-fibril cross-links, and greater mechanical stiffness

[30,33-36]. This increase in stiffness renders the matrix more difficult for endothelial cells to deform, degrade and remodel. There are numerous studies that suggest that growth during angiogenesis depends on the cells ability to deform, degrade and remodel the ECM. Increasing the matrix resistance to deformation *in vitro*, either by increasing mechanical stiffness through the structure and composition of the ECM [17,18,20,37] or by imposing boundary conditions to prevent contraction of the gel [19,27,33], results in a decrease in angiogenic growth. These results have been observed using both cell and organ culture models of angiogenesis, and suggest that the rate of angiogenic outgrowth is regulated by the stiffness of the matrix. Califano and Reinhart-King used BAECs (bovine aortic endothelial cells) in compliant polyacrylamide substrates functionalized with type-I collagen to demonstrate that stiffness alone regulates angiogenic growth, independent of the density of ligands available for integrin binding [20]. Additionally, Kniazeva et al. demonstrated that increased fibrin density *in vivo* despite the presence of both endothelial and stromal cells [38]. VEGF signaling leads to increased stress fibers and focal adhesions within endothelial cells, mediated through the receptor VEGFR2 and activity of Rho and ROCK (Rho-Kinase) [39-41]. These results suggest that angiogenic endothelial cells within the sprout tip may receive positive feedback that promotes the angiogenic phenotype and growth when the cells detect a compliant matrix that they can deform and condition. We were able to simulate this behavior in our growth model by scaling the length of new segments creating during the growth step (i.e., the amount of net growth that occurred over the time step) with respect to local matrix density.

Increasing the matrix density also reduced the rate of branch formation during

angiogenesis. Ghajar et al. reported similar observations of reduced sprouting upon increasing the density of the matrix using HUVECs cultured on microspheres within a fibrin matrix [15,16]. A feeder layer of fibroblasts was cultured on top of the matrix to serve as a source of growth factors. Ghajar et al. proposed that increasing matrix density reduced sprouting by decreasing the porosity of matrix and hindering the diffusion of soluble growth factors [16]. This conclusion was supported by the observation that co-culturing fibroblasts within the matrix along with endothelial cells improved sprouting [16]. In the co-culture model, the fibroblasts acted as pseudo-stroma cells and the length over which growth factors had to diffuse over to reach the endothelial cells was drastically reduced. In our experiments, an organ culture model of microvessels within collagen gel exhibited a similar trend of reduced angiogenesis across increases in matrix density. Endothelial cells within this culture model remain intact as microvessel fragments and retain their association with stroma cells (pericytes) and the basement membrane. Therefore, the diffusive length between neovessel sprouts and the stroma was small. Additionally, the growth media in our cultures was supplemented with VEGF in order to ensure a uniform presence of growth factor throughout the gel, although we did not measure diffusivity in our gels as a function of collagen concentration Nevertheless, the inverse relationship between neovessel sprouting and matrix density observed in the present study suggests the existence of an additional mechanism, independent from chemotaxis, which is responsible for the effects of matrix density on angiogenic sprouting.

Endothelial cells within nonsprouting microvessels are subjected to the combined loading of intercellular tractions from neighboring endothelial cells and pericytes and

extra-cellular forces from the ECM. The results of several studies suggest that the angiogenic sprouting phenotype of endothelial cells is regulated by a balance between intercellular and extracellular forces [12,42-47]. For example, Ingber proposed that if traction applied to a vessel was large enough to cause a shift in this balance, then endothelial cells change to an angiogenic sprouting phenotype and begin the formation of a new sprout [44]. Additionally, a previous computational study predicted that steep gradients in matrix density would lead to increased stress along the neovessel, resulting in sprouting [45]. Cells can mechanically communicate with each other through compliant, deformable substrates [8-10]. As angiogenic sprouts grow, they apply traction along protrusions attached to the ECM through integrins at focal adhesions, which causes local deformation and remodeling. The deformation can be detected by other cells if they are within range of the sprout. A strong deformation signal could cause endothelial cells within other vessels to adopt the angiogenic phenotype and form a new sprout, similar to how deformation signals promote growth as discussed earlier. The amount of deformation that sprouts can generate as well as the range over which cell-generated forces travel depends on the stiffness of the ECM. In stiffer matrix, sprouts produce less deformation, forces are not transmitted as far, and as a result, cells within other microvessels experience less extracellular loading and are less prone to adopt the angiogenic phenotype and sprout into a new branch. Although we use a random-based mechanism for branching in our growth model rather than a deterministic approach, we were able to capture this behavior by scaling the probability of branch formation with respect to local matrix density.

The model outlined in this study incorporated a number of simplifying assumptions,

and made use of random processes rather than mechanistic and/or deterministic approaches to represent certain aspects of angiogenesis. These limitations are in part due to the fact that the exact mechanisms as to how the mechanical interaction between neovessels and the ECM affect all the different aspects of angiogenesis and neovasculaturization are not well understood. To describe these mechanisms, additional data are needed on both the deformations experienced by cells locally as well as how cells integrate those signals and respond. It is our hope that we can continue to expand the model incrementally, adding complexity as we gain additional experimental insight. For example, matrix density and fibril orientation were assumed to be constant over the growth period, which does not accurately represent changes in the ECM that are known to occur during angiogenesis. Angiogenic neovessels within our organ culture model extensively alter and condense the matrix via traction forces [12,48]. However, our current framework does not update physical and material properties of the ECM during the growth period in response to deformation caused by cellular traction forces. As a result, the function for calculating the scaling factor in Equation 4.3 is based on initial matrix density rather than current matrix density. Our goal when implementing the scaling factor was to obtain realistic representation of the growth and branching rate as matrix density change. The valid predictions of morphometric data in simulations at different matrix density levels indicate that the assumptions used in our approach were sufficient for our level of analysis even though it was calibrated using initial collagen concentration yet was applied to all time points during the simulation. In future work, coupling the growth model with the field theories of continuum mechanics will provide a simulation framework for studying how mechanical forces and ECM structure at the

microscale influence the topology of the vascular network. Such a framework could be extended to other morphogenic processes and would allow investigators to establish cause-and-effect relationships between cell-generated forces, matrix deformation and remodeling, the subsequent cellular response, and the morphology of the emerging tissue.

In summary, increasing the density of the ECM significantly reduced angiogenesis and network formation within a 3D organ culture model of angiogenesis. The computational framework outlined in this study was capable of predicting this observed experimental behavior by adjusting neovessel growth rate and branching probability according to local ECM density, demonstrating that these changes in neovessel behavior are responsible for the differences in vascular topology we found. In future studies, this computational framework could be extended in the future by coupling vessel growth with matrix deformation, enabling advanced study of the mechanics of angiogenesis and other morphogenic processes.

4.6 References

[1] Fisher, C., Gilbertson-Beadling, S., Powers, E.A., Petzold, G., Poorman, R. and Mitchell, M.A. (1994) "Interstitial collagenase is required for angiogenesis in vitro," Dev Biol 162:499-510.

[2] Haas, T.L., Davis, S.J. and Madri, J.A. (1998) "Three-dimensional type I collagen lattices induce coordinate expression of matrix metalloproteinases MT1-MMP and MMP-2 in microvascular endothelial cells," J Biol Chem 273:3604-3610.

[3] Vernon, R.B. and Sage, E.H. (1999) "A novel, quantitative model for study of endothelial cell migration and sprout formation within three-dimensional collagen matrices," Microvasc Res 57:118-133.

[4] Rivilis, I., Milkiewicz, M., Boyd, P., Goldstein, J., Brown, M.D., Egginton, S., Hansen, F.M., Hudlicka, O. and Haas, T.L. (2002) "Differential involvement of MMP-2 and VEGF during muscle stretch- versus shear stress-induced angiogenesis," Am J Physiol Heart Circ Physiol 283:H1430-H1438.

[5] Tranqui, L. and Tracqui, P. (2000) "Mechanical signalling and angiogenesis. The integration of cell- extracellular matrix couplings," CR Acad Sci Paris Life Sci 323:31-47.

[6] Vailhe, B., Ronot, X., Tracqui, P., Usson, Y. and Tranqui, L. (1997) "In vitro angiogenesis is modulated by the mechanical properties of fibrin gels and is related to alpha(v)beta3 integrin localization," In Vitro Cell Dev Biol Anim 33:763-73.

[7] Vernon, R.B. and Sage, E.H. (1996) "Contraction of fibrillar type I collagen by endothelial cells: A study in vitro," J Cell Biochem 60:185-197.

[8] Hur, S.S., Zhao, Y., Li, Y.S., Botvinick, E. and Chen, S. (2009) "Live cells exert 3-dimensional traction forces on their substrata," Cell Mole Bioeng 2:425-436.

[9] Lopez, J.I., Mouw, J.K. and Weaver, V.M. (2008) "Biomechanical regulation of cell orientation and fate," Ocogene 27:6981-6993.

[10] Reinhart-King, C.A., Dembo, M. and Hammer, D.A. (2008) "Cell-cell mechanical communication through compliant substrates," Biophys J 95:6044-6051.

[11] Hoying, J.B., Boswell, C.A. and Williams, S.K. (1996) "Angiogenic potential of microvessel fragments established in three-dimensional collagen gels," In Vitro Cell Dev Biol Anim 32:409-19.

[12] Krishnan, L., Hoying, J.B., Nguyen, H., Song, H. and Weiss, J.A. (2007) "Interaction of angiogenic microvessels with the extracellular matrix," Am J Physiol Heart Circ Physiol 293:H3650-8.

[13] Krishnan, L., Underwood, C.J., Maas, S., Ellis, B.J., Kode, T.C., Hoying, J.B. and Weiss, J.A. (2008) "Effect of mechanical boundary conditions on orientation of angiogenic microvessels," Cardiovasc Res 78:324-32.

[14] Underwood , C.J., Edgar, L.T., Maas, S.A., Krishnan, L., Hoying, J.B. and Weiss, J.A. "The effects of geometry and static boundary conditions on microvessel outgrowth in a 3D model of angiogenesis," Proc. ASME Summer Bioengineering Conference 2010. Naples, FL, USA.

[15] Ghajar, C.M., Blevins, K.S., Hughes, C.C., George, S.C. and Putnam, A.J. (2006) "Mesenchymal stem cells enhance angiogenesis in mechanically viable prevascularized tissues via early matrix metalloproteinase upregulation," Tissue Eng 12:2875-2888.

[16] Ghajar, C.M., Chen, X., Harris, J.W., Suresh, V., Hughes, C.C., Jeon, N.L., Putnam, A.J. and George, S.C. (2008) "The effect of matrix density on the regulation of 3-D capillary morphogenesis," Biophys J 94:1930-41.

[17] Kniazeva, E. and Putnam, A.J. (2009) "Endothelial cell traction and ECM density influence both capillary morphogenesis and maintenance in 3-D," Am J Physiol Cell Physiol 297:C179-C187.

[18] Sieminski, A.L., Hebbel, R.P. and Gooch, K.J. (2004) "The relative magnitudes of endothelial force generation and matrix stiffness modulate capillary morphogenesis in vitro," Exp Cell Res 297:574-84.

[19] Yamamura, N., Sudo, R., Ikeda, M. and Tanishita, K. (2007) "Effects of the mechanical properties of collagen gel on the in vitro formation of microvessel networks by endothelial cells," Tissue Eng 13:1443-1453.

[20] Califano, J.P. and Reinhart-King, C.A. (2008) "A balance of substrate mechanics and matrix chemistry regulates endothelial cell network assembly," Cell Mol Bioeng 1:122-132.

[21] Peirce, S.M. (2008) "Computational and mathematical modeling of angiogenesis," Microcirculation 15:739-51.

[22] Chang, C.C., Krishnan, L., Nunes, S.S., Church, K.H., Edgar, L.T., Boland, E.D., Weiss, J.A., Williams, S.K. and Hoying, J.B. (2012) "Determinants of microvascular network topologies in implanted neovasculatures," Arterioscler Thromb Vasc Biol 32:5-14.

[23] B.R., S., Chen, H.Y., Smith, C.M., Gruionu, G., Williams, S.K. and Hoying, J.B. (2004) "Rapid perfusion and network remodeling in a microvascular construct after implantation," Arterioscler Thromb Vasc Biol 24:898-904.

[24] Chang, C.C. and Hoying, J.B. (2006) "Directed three-dimensional growth of microvascular cells and isolated microvessel fragments," Cell Transplant 15:533-540.

[25] Nunes, S.S., Greer, K.A., Stiening, C.M., Chen, H.Y., Kidd, K.R., Schwartz, M.A., Sullivan, C.J., Rekapally, H. and Hoying, J.B. (2010) "Implanted microvessels progress through distinct neovascularization phenotypes,"

Microvasc Res 79:10-20.

[26] Chang, C.C., Nunes, S.S., Sibole, S.C., Krishnan, L., Williams, S.K., Weiss, J.A. and Hoying, J.B. (2010) "Angiogenesis in a microvascular construct for transplantation depends on the method of chamber circulation," Tissue Eng Part A 16:795-805.

[27] Nunes, S.S., Krishnan, L., Gerard, C.S., Dale, J.R., Maddie, M.A., Benton, R.L. and Hoying, J.B. (2010) "Angiogenic potential of microvessel fragments is independent of the tissue of origin and can be influenced by the cellular composition of the implants," Microcirculation 17:557-567.

[28] Bottenstein, J.E. and Sato, G.H. (1979) "Growth of a rat neuroblastoma cell line in serum-free supplemented medium," Proc Natl Acad Sci USA 76:514-7.

[29] Liu, Y., Griffith, M., Watsky, M.A., Forrester, J.V., Kuffova, L., Grant, D., Merrett, K. and Carlsson, D.J. (2006) "Properties of porcine and recombinant human collagen matrices for optically clear tissue engineering applications," Biomacromolecules 7:1819-28.

[30] Wood, G.C. and Keech, M.K. (1960) "The formation of fibrils from collagen solutions. 1. The effect of experimental conditions: Kinetic and electron-microscope studies," Biochem J 75:588-98.

[31] Richter, S.J. and Richter, C. (2012) "A method for determining equivalence in industrial applications," Quality Engng 14:375-380.

[32] Edgar, L.T., Sibole, S.C., Underwood, C.J., Guilkey, J. and Weiss, J.A. (2013) "A computational model of in vitro angiogenesis based on extracellular matrix fiber orientation," Comp Meth Biomech Biomed Eng 16:790-801.

[33] Nicosia, R.F. and Ottinetti, A. (1990) "Modulation of microvascular growth and morphogenesis by reconstituted basement membrane gel in three-dimensional cultures of rat aorta: A comparative study of angiogenesis in matrigel, collagen, fibrin, and plasma clot," In Vitro Cell Dev Biol 26:119-28.

[34] Nicosia, R.F. and Ottinetti, A. (1990) "Growth of microvessels in serum-free matrix culture of rat aorta. A quantitative assay of angiogenesis in vitro," Lab Invest 63:115-22.

[35] Krishnan, L., Weiss, J.A., Wessman, M.D. and Hoying, J.B. (2004) "Design and application of a test system for viscoelastic characterization of collagen gels," Tissue Eng 10:241-52.

[36] Roeder, B.A., Kokini, K., Sturgis, J.E., Robinson, J.P. and Voytik- Harbin, S.L.

(2002) "Tensile mechanical properties of three-dimensional type I collagen extracellular matrices with varied microstructure," J Biomech Eng 124:214-22.

[37] Rao, R.R., Peterson, A.W., Ceccarelli, J., Putnam, A.J. and Stegemann, J.P. (2012) "Matrix composition regulates three-dimensional network formation by endothelial cells and mesenchymal stem cells in collagen/fibrin materials," Angiogenesis 15:253-264.

[38] Kniazeva, E., Kachgal, S. and Putnam, A.J. (2011) "Effects of extracellular matrix density and mesenchymal stem cells on neovascularization in vivo," Tissue engng. Part A 17:905-14.

[39] Huot, J., Houle, F., Rousseau, S., Deschesnes, R.G., Shah, G.M. and Landry, J. (1998) "SAPK2/p38-dependent F-actin reorganization regulates early membrane blebbing during stress-induced apoptosis," J Cell Biol 143:1361-73.

[40] van Nieuw Amerongen, G.P., Koolwijk, P., Versteilen, A. and van Hinsbergh, V.W. (2003) "Involvement of RhoA/Rho kinase signaling in VEGF-induced endothelial cell migration and angiogenesis in vitro," Arterioscler Thromb Vasc Biol 23:211-7.

[41] Yang, M.T., Reich, D.H. and Chen, C.S. (2011) "Measurement and analysis of traction force dynamics in response to vasoactive agonists," Integr Biol 3:663-74.

[42] Shiu, Y.T., Weiss, J.A., Hoying, J.B., Iwamoto, M.N., Joung, I.S. and Quam, C.T. (2005) "The role of mechanical stresses in angiogenesis," Crit Rev Biomed Eng 33:431-510.

[43] Korff, T. and Augustin, H. (1999) "Tensional forces in fibrillar extracellular matrices control directional capillary sprouting," J Cell Sci 112:3249-3258.

[44] Ingber, D. (2002) "Mechanical signaling and the cellular response to extracellular matrix in angiogenesis and cardiovascular physiology," Circ Res 91:877-887.

[45] Bauer, A., Jackson, T.L. and Jiang, Y. (2009) "Topography of extracellular matrix mediates vascular morphogenesis and migration speeds in angiogenesis," PLOS Comp Biol 5.

[46] Guo, W.H., Frey, M.T., Burnham, N.A. and Wang, Y.L. (2006) "Substrate rigidity regulates the formation and maintenance of tissues," Biophys J 90:2213-20.

[47] Parker, K.K., Brock, A.L., Brangwynne, C., Mannix, R.J., Wang, N., Ostuni, E.,

Geisse, N.A., Adams, J.C., Whitesides, G.M. and Ingber, D.E. (2002) "Directional control of lamellipodia extension by constraining cell shape and orienting cell tractional forces," FASEB J 16:1195-204.

[48] Kirkpatrick, N.D., Andreou, S., Hoying, J.B. and Utzinger, U. (2007) "Live imaging of collagen remodeling during angiogenesis," Am J Physiol Heart Circ Physiol 292:H3198-206.

CHAPTER 5

A COUPLED MODEL OF NEOVESSEL GROWTH AND MATRIX MECHANICS DESCRIBES AND PREDICTS ANGIOGENESIS IN VITRO

5.1 Abstract

During angiogenesis, sprouting microvessels interact with the extracellular matrix (ECM) by degrading and reorganizing the matrix, applying traction forces and producing deformation. Morphometric features of the resulting microvascular network are affected by the interaction between the matrix and angiogenic microvessels. The objective of this study was to develop a continuous-discrete modeling approach to simulate mechanical interactions between growing neovessels and the deformation of the matrix *in vitro*. This was accomplished by coupling an existing angiogenesis growth model which uses properties of the ECM to regulate angiogenic growth with the nonlinear finite element software FEBio (www.febio.org). FEBio solves for the deformation and remodeling of the matrix caused by active stress generated by neovessel sprouts, and this deformation was used to update the ECM into the current configuration. After mesh resolution and parameter sensitivity studies, the model was used to accurately predict vascular alignment for various gel boundary conditions.

Alignment primarily arises passively as microvessels convect with the deformation of the matrix, but active alignment along collagen fibrils plays a role as well. Predictions of alignment were most sensitive to the range over which active stresses were applied and the viscoelastic time constant in the material model. The computational framework provides a flexible platform for interpreting *in vitro* investigations of vessel-matrix interactions, predicting new experiments, and simulating conditions that are outside current experimental capabilities.

5.2 Introduction

New vasculature arises from existing vasculature by the process of angiogenesis. A number of challenges within medical and bioengineering research are associated with angiogenesis and the expansion of the microvasculature. In normal tissue, angiogenesis is involved with exercise, reproduction, and development of the embryo [1-3]. In pathological tissue, angiogenesis is associated with cancer and atherosclerosis causing uncontrolled vessel growth, while ischemia, scar formation, and poor wound healing involve insufficient vessel growth and perfusion [4-8]. Bioengineering challenges concerning angiogenesis involve promoting neovascularization of scaffolds for engineering tissue implants [9-11]. Angiogenesis is highly sensitive to both the local chemical and mechanical microenvironment [7, 12-14], and although extensive research has been performed regarding the chemical regulation of angiogenesis, the mechanical factors that regulate angiogenesis remain poorly understood.

Neovessels expand the vascular bed through the extracellular space via extension and mitosis, applying traction and migrating along components of the extracellular

matrix (ECM) [15]. Successful tissue neovascularization requires that the topology of the new network meets the perfusion and metabolic requirements for that tissue [16]. Mechanical interactions during angiogenesis, i.e., traction applied by neovessels to the ECM and the corresponding deformation, are important regulators of growth and neovascularization. Mechanical aspects of the ECM including material properties, density and boundary conditions modulate these mechanical interactions. For example, using a 3D *in vitro* organ culture model of microvessel fragments within a type-I collagen gel, we have demonstrated that changing the matrix boundary conditions drastically affects the topology and rate of growth of the new vascular network (Figure 5.1) [17-22]. Microvessels within free-floating, unconstrained constructs grew into a microvascular network with no preferred orientation (Figure 5.1 C). When the long-axis of the hexahedral constructs was constrained, microvessels aligned along this constrained axis [19, 20, 22] (Figure 5.1 D). However, this alignment did not correlate with stress within the gel, as constraining the short-axis of the gel did not lead to alignment along that direction [22] (Figure 5.1 E). Additionally, when the density of the matrix was increased, the rate of angiogenic growth and branching decreased and neovascularization was reduced [18]. In all of these experiments, we found that restricting cells from deforming and remodeling the matrix (i.e., increasing the apparent stiffness, either through increasing density or adding a boundary constraint) reduced angiogenesis. However, the dynamic relationship between cell-generated forces, the deformation of the ECM, and angiogenic growth and neovascularization requires further characterization and study. Morphogenic processes such as angiogenesis occur across different physical scales. Individual cellular behavior within neovessel sprouts at

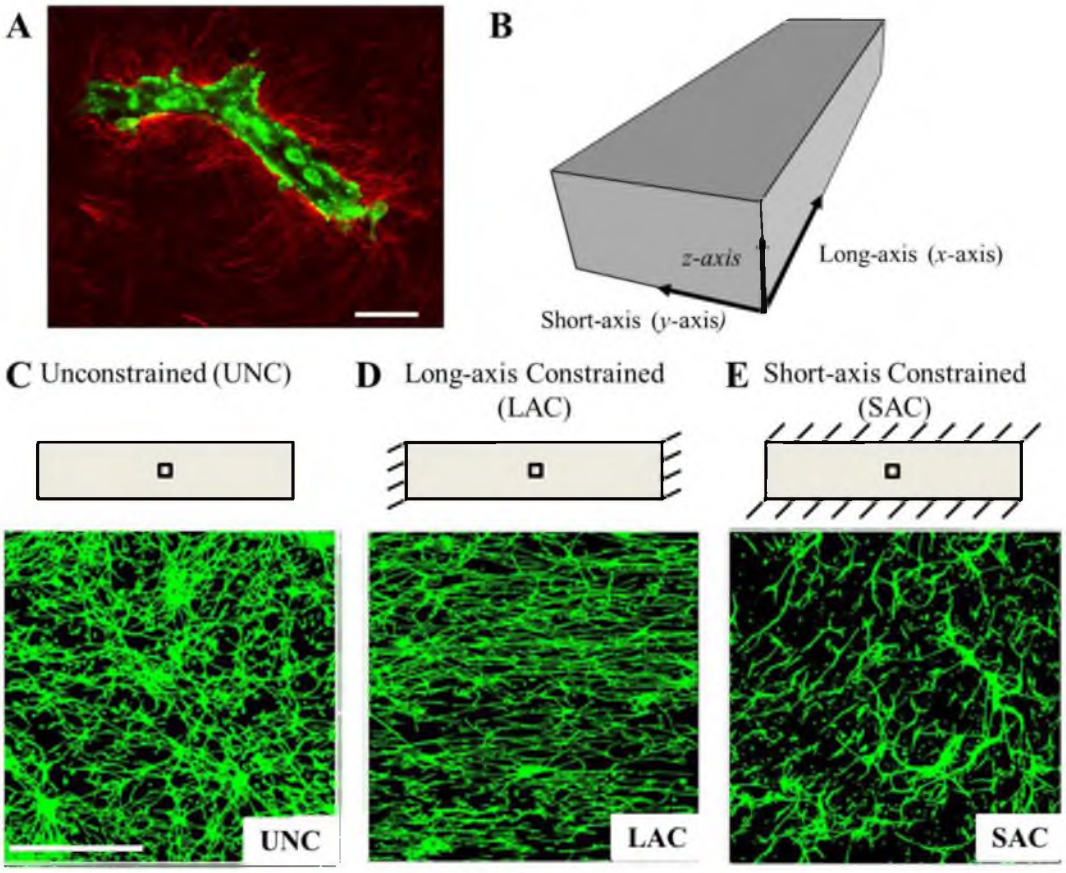

Figure 5.1: Boundary constraints induce alignment during *in vitro* culture of angiogenic microvessel fragments in 3D collagen gels. Microvessel fragments were harvested from rat fat pads and cultured in a type-I collagen matrix. (A) A parent microvessel fragment in 3D collagen gel imaged using two-photon microscopy. Endothelial cells and pericytes were imaged using autofluoresence (green), collagen fibrils were imaged using second-harmonic generation (red). Scale bar 20 μm. (B) Schematic of a hexahedral vascularized construct subjected to various boundary conditions. The long-axis of the gels was defined as the x-axis, the short-axis as the y-axis, and the thickness of the gel as the z-axis. (C) Schematic (top) and confocal image (bottom) of unconstrained vascularized construct. The interior black box in the schematic indicates the location of image acquisition using confocal microscopy. Microvessel growing in the free-floating unconstrained gels had no preferred orientation. Scale bar 500 μm. (D) When the long-axis of the gel was constrained, microvessels were highly aligned along the constrained axis. (E) In contrast, constraining the short-axis of the constructs resulted in random microvessel alignment, demonstrating that alignment does not correlate with stress in the matrix due to an imposed boundary constraint. Rather, transverse matrix deformation produces the alignment, and this deformation depends on the local effective stiffness of the ECM.

the microscale (< 1 mm) regulates the emergent properties of the new vascular network at the tissue macroscale (> 1 mm), such as vascular perfusion, branching, and orientation. *In vitro* cell and organ culture models typically do not permit the manipulation of experimental conditions and observation of the response across length scales (i.e., changing properties at the macroscale while observing behavior at the microscale and vice versa), providing insufficient information on how individual neovessel sprouts react in response to macroscopic changes to the ECM such as the addition of a boundary constraint. Additionally, data from these experiments are often limited to a single time point and do not provide information into dynamic regulation of angiogenic growth. Therefore, we designed and implemented a computational model of angiogenesis in order to supplement our experimental efforts. This growth model uses information about the local ECM to determine neovessel growth and branching and is capable of accurately describing angiogenesis across changes in matrix fibril orientation and density [18, 23]. However, in these past studies the properties of the matrix remained constant during simulations and did not include changes that occur as a result of matrix deformation. Neovessels change the properties that regulate their growth as they deform and remodel the matrix, creating a dynamic feedback loop in which growth is coupled to matrix deformation. To the best of our knowledge, no existing model of angiogenesis includes the capability to study the dynamic biomechanical regulation of growth with regards to macroscopic tissue morphology.

The objective of this research was to expand our existing growth model to include these dynamic mechanical interactions between neovessels and the matrix, and to demonstrate the ability of the computational framework to describe and predict

experimental morphometric and geometric measurements of angiogenesis. We coupled our discrete computational model of angiogenesis with the nonlinear finite element (FE) software FEBio [24]. FEBio was used to solve for the deformation caused by cell-generated forces applied to the ECM, and this solution was used to update the biophysical properties of the ECM, creating a dynamic feedback between matrix mechanics and angiogenic growth. The framework was calibrated using simulations of long-axis constrained gels with the goal of describing the results for vascular alignment seen in the experiments. The model was then used to predict vascular alignment in the other two experimental boundary conditions (unconstrained, short-axis constrained) to demonstrate how these individual mechanical interactions produce global vascular alignment in a general sense. The resulting modeling framework provides a flexible and robust platform for investigating the dynamic biomechanical regulation of complex cellular processes such as angiogenesis. Many morphogenic processes involve a similar biomechanical regulation of cellular behavior over time, and in the future these methods could be extended to study similar processes such as neurogenesis and lymphangiogenesis as well as tumor formation and metastasis.

5.3 Methods

5.3.1 Culture of vascularized constructs

Collagen-based vascularized constructs were used as a 3D *in vitro* model of sprouting angiogenesis. Microvessel fragments were isolated and cultured using methods described previously [18-20, 22, 25]. All components were obtained through Invitrogen (Carlsbad, CA) unless otherwise noted. Epididymal fat pads were harvested

from male Sprague-Dawley rats in accordance to the University of Utah Institutional Animal Care and Use Committee and then minced and subjected to limited digestion with collagenase (Worthington Biochemical, Lakewood, NJ). Fragments were then washed twice and resuspended in L-15 media. The solution was sequentially filtered through 350 and 30 μm sterile nylon filters to remove both large clumps of tissue and single cells. The remaining microvessels were resuspended in 3.0 mg/ml liquid collagen at 50,000 fragments/ml and poured into Teflon molds to cast the vascularized constructs into a hexahedral shape (20.5 × 5.5 × 3.0 mm). Unconstrained (UNC) constructs were left free-floating in media during culture (Figure 5.1 C). Long-axis constrained (LAC) constructs were created by inserting a stainless steel mesh into the liquid collagen solution prior to polymerization in order to prevent contraction along the long-axis (x-axis) during growth [20, 22] (Figure 5.1 D). Short-axis constrained (SAC) constructs were similarly constrained along the short-axis (y-axis) using a stainless steel mesh [22] (Figure 5.1 E). Microvessel constructs were cultured for 6 days in serum-free culture media [26] supplemented with rhVEGF (Peprotech, Rocky Hill, NJ). A total of 7 constructs were cultured for each boundary condition (N_{exp} = 7). Gel contraction was defined as the negative of axial engineering strain along each direction (ε_{xx}, ε_{yy}, and ε_{zz}) and was calculated by collecting digital images of the vascularized constructs and measuring the final dimensions at the geometric center. Acellular controls were used to obtain measurements in the reference configuration.

5.3.2 Imaging and quantification of microvessel alignment

After 6 days of culture, constructs were fixed in paraformaldehyde and stained with Isolectin GS-IB4 conjugated to Alexa 488 to fluorescently label endothelial cells. 3D image datasets of vascular networks within the collagen gels were obtained using laser scanning confocal microscopy. The constructs were oriented within the long-axis parallel to the horizontal imaging axis (*x*-axis) and imaging was performed at the geometric center of each construct. Each volumetric image dataset consisted of 4 adjacent (2 × 2) 10× stacks with a 2.5 μm step size through the thickness (*z*-direction) covering a depth of 300 μm. The assembled mosaic datasets had dimensions of 2548 × 2548 × 300 μm (1024 × 1024 × 120 voxels). Datasets were processed and skeletonized using the AMIRATM software (Visage Imaging, San Diego, CA), as described previously [19, 20, 22]. To quantify vascular alignment in the 3D image data, a custom software application WinFiber3D [27] was used to measure the angle that each microvessel formed relative to the long-axis (*x*-axis) of the construct.

5.3.3 Finite element mesh

The vascularized constructs were discretized using a rectilinear hexahedral FE mesh. To reduce computational cost, a 1/8th symmetry model was created. Symmetry planes were defined in the *xy*-, *xz*-, and *yz*-planes at the geometric center of the construct (Figure 5.2). Nodes along the *xy*-, *xz*-, and *yz*- symmetry planes were constrained in the *z*, *y*, and *x* directions, respectively. When simulating a LAC gel, nodes along the face of the mesh normal to the –*x* direction were fully constrained representing the boundary condition imposed by the stainless steel mesh. In the SAC

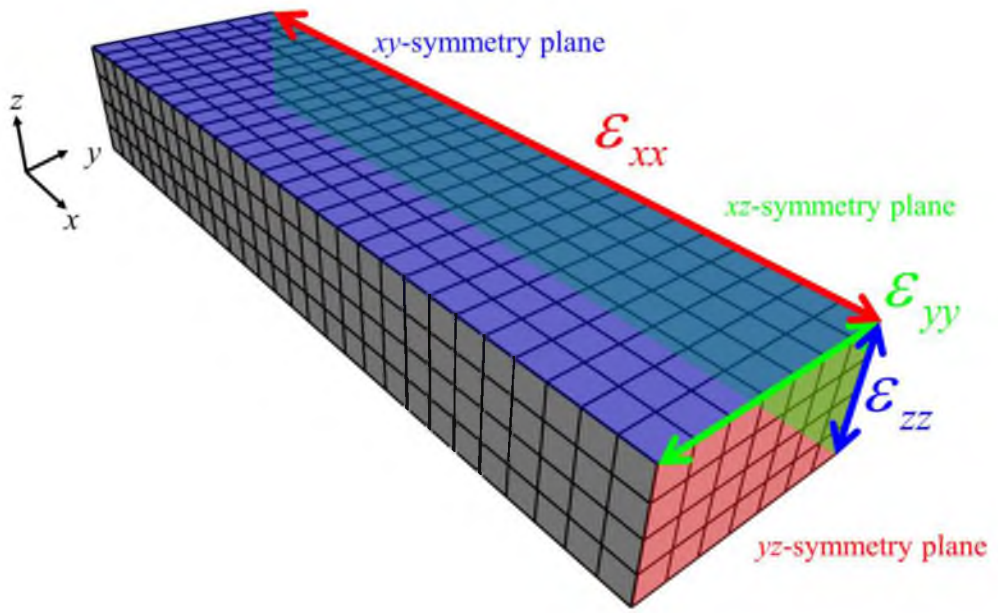

Figure 5.2: FE representation of vascularized collagen gels. Symmetry was applied when constructing the mesh, creating an 1/8th symmetry model. Nodes along the *xy*-, *xz*-, and *yz*- symmetry planes were constrained in the *z*, *y*, and *x* directions, respectively. At the conclusion of each simulation, the gel contraction (ε_{xx}, ε_{yy}, and ε_{zz}) was measured along where the symmetry planes intersect, corresponding to the geometric center of the construct.

simulations, nodes along the face of the mesh normal to the $-y$ direction were fully constrained. Simulations of the UNC constructs included no additional nodal constraints beyond the symmetry constraints. At the conclusion of each simulation, the gel contraction (ε_{xx}, ε_{yy}, and ε_{zz}) was measured along where the symmetry planes intersect, corresponding to the geometric center of the construct, in order to compare to experimental data.

5.3.4 Discrete computational model of microvessel growth

Microvessel geometry was predicted by angio3d, a computational growth model of microvessel fragments during spontaneous angiogenesis [18, 23]. The model predicts the direction and rate of microvessel growth based on physical properties of the ECM, including collagen fibril orientation and matrix density, and the model has been validated against experimental measurements of angiogenic growth within vascularized constructs with both randomly orientated and aligned ECM [23] and for various levels of matrix density [18].

Matrix density and fibril orientation were specified at each node of the FE mesh. During initialization, a random collagen fibril unit vector, θ, was generated for each node, as collagen fibrils are randomly aligned in both acellular and vascularized constructs at Day 0 [20]. The initial collagen density ρ_0 was also prescribed at each node, based on the 3.0 mg/ml density in the experiments. Microvessels were represented as a discrete collection of end-to-end line segments. The model was initialized by seeded initial line segments throughout the mesh at random position and orientation. Both ends of each segment were designated active growth tips, and any

segment with an active growth tip was referred to as a sprout. At each discrete time step, neovessel elongation (i.e., growth) was simulated by the addition of a new line segment $\boldsymbol{v}$ at each active tip location (Figure 5.3 A). Local ECM information was used to determine the orientation of the new segment, described by the unit vector $\hat{\boldsymbol{v}}$, and the length of the new segment, described by the magnitude $\|v\|$. The FE trilinear shape functions were used to interpolate nodal values of fibril orientation and matrix density to the location of the sprout:

$$\boldsymbol{\theta}(\boldsymbol{x}_s) = \sum_{j=1}^{8} \boldsymbol{\theta}_j N_j(\boldsymbol{x}_s) \,, \tag{5.1}$$

$$\rho(\boldsymbol{x}_s) = \sum_{j=1}^{8} \rho_j N_j(\boldsymbol{x}_s) \,. \tag{5.2}$$

In these equations, $\boldsymbol{x}_s$ is the position of the active sprout tip, $\boldsymbol{\theta}_j$ and ρ_j are the fibril orientation vector and matrix density at node j, and N_j is the value of the shape function for node j evaluated at the sprout position. The direction of a new neovessel segment ($\hat{\boldsymbol{v}}$, the net direction of growth over the time step) was determined by a weighted average of the parent sprout's direction and the local collagen fibril orientation [18]. The length of a new segment, $\|v\|$, representing the net amount of growth that occurred over the time step, was calculated from experimental data and scaled relative to local matrix density as described previously [18]. After each elongation step, the active sprout tip was transferred from the parent segment to the new segment accordingly.

Branching, the spontaneous formation of a new sprout along an existing vessel, was modeled as a random process. At each time step, a random number between 0 and 1

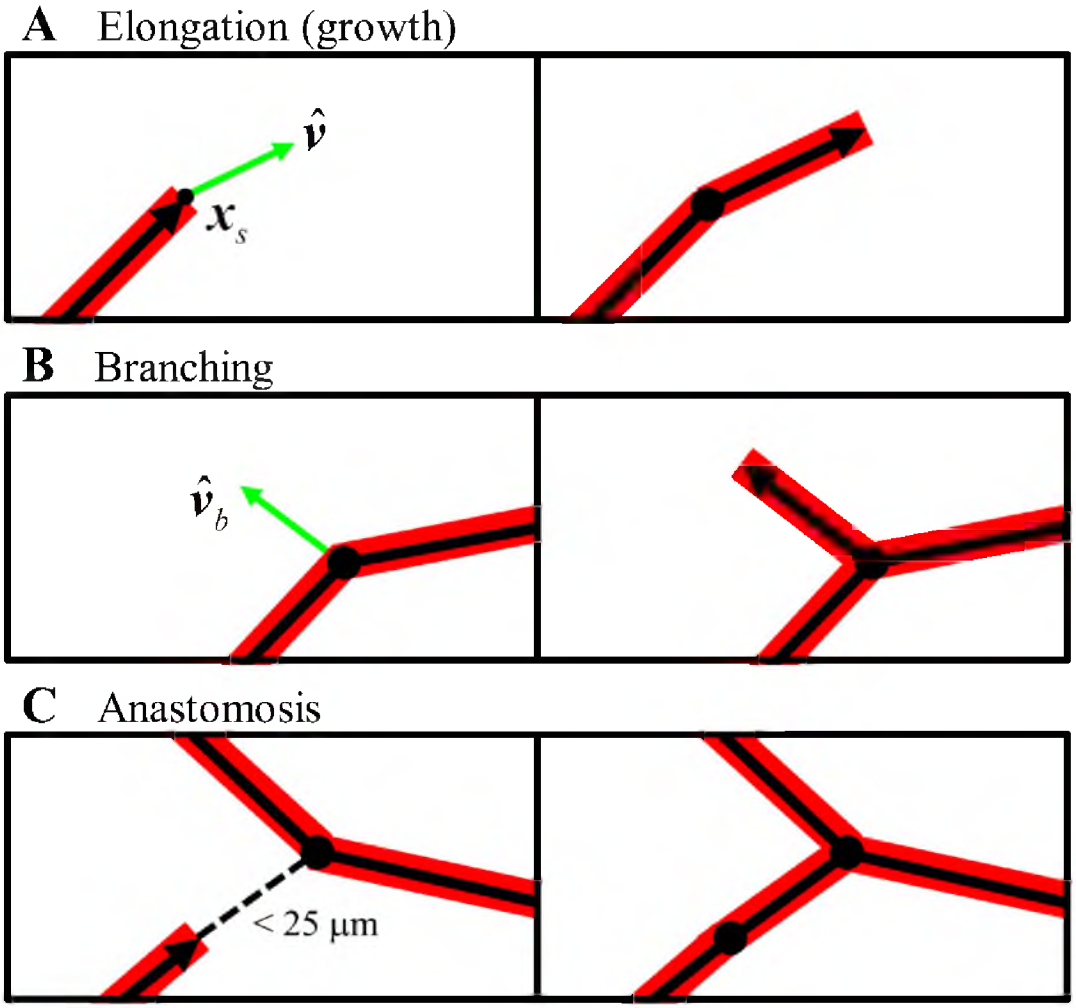

Figure 5.3: Angiogenesis was simulated using a discrete growth model. Microvessels were represented as a collection end-to-end line segments. Segments with an active growth tips were defined as sprouts, indicated by the segments with an arrowhead. (A) Neovessel elongation (i.e., growth) was simulated by creating new line segments at all active sprout tips. The direction of the new segment, $\hat{v}$, was determined by local collagen fibril orientation and the direction of the parent segment. After the growth step, the active tip was transferred to the new segment from the parent segment. (B) Branching was modeled as a random process. During each time step, all segments in the simulation generated a random number. If this number was less than the branching probability b_0, then that segment was allowed to branch and a new active sprout was created along the direction of $\hat{v}_b$. (C) Anastomosis, the fusing of two microvessels, was permitted for any active sprout within 25 μm of another vessel. This was simulated by creating a new line segment connecting the two vessels and disabling all growth tips.

was generated for all segments. If the number exceeded a branching probability, b_0, then a branch was formed and a new segment was created (Figure 5.3 B). The direction of the new branch, $\hat{\boldsymbol{v}}_b$, was determined by local collagen orientation and the projector formed by the outer product of the direction of parent segment , $\hat{\boldsymbol{v}}$, with itself such that

$$\hat{\boldsymbol{v}}_b = \left(\boldsymbol{I} - \frac{1}{2}\hat{\boldsymbol{v}} \otimes \hat{\boldsymbol{v}} \right) \cdot \boldsymbol{\theta} \ , \tag{5.3}$$

where $\boldsymbol{\theta}$ is the collagen fibril orientation at the position of the new branch point as determined by Equation 5.1 and $\boldsymbol{I}$ is the second-order identity tensor. The branching probability for each segment was scaled according to local matrix density such that the probability of forming a branch decreased as density increased, as described previously [18]. The formation of new vascular connection within the emerging network via anastomosis was permitted for all active sprouts within close proximity of another vessel. If a sprout was within 25 μm of another segment, the vessels anastomose by creating a line segment connecting the active sprout and intersection point (Figure 5.3 C). After anastomosis, any active growth tips involved in the event were inactivated. This method of simulating anastomosis provides accurate predictions of morphometric data describing the vascular network such as number of branch points, number of free ends, and network interconnectivity [18].

5.3.5 Vessel boundary conditions

If a new segment crossed the boundaries of the simulation domain, the segment was divided into a portion inside the mesh, $\boldsymbol{v}_i$, and a portion outside the mesh, $\boldsymbol{v}_o$ (Figure 5.4 A, B):

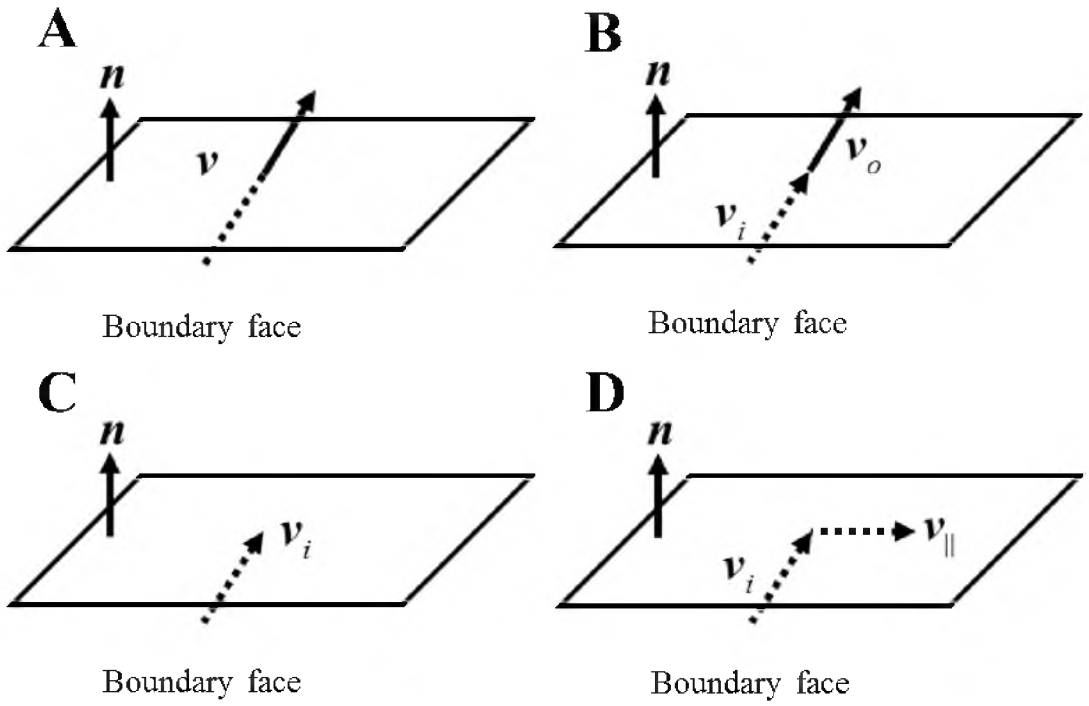

Figure 5.4: Vessel boundary conditions in the growth model. Vectors inside the mesh are dashed, vectors outside are solid. (A) When a segment was found to grow outside the mesh and through a boundary face, the segment was split into an inside component, v_i, and an outside component, v_o (B). There were two different types of boundary conditions enforced on microvessels during growth. (C) Mesh boundary: The faces of the mesh at the symmetry planes and any fully constrained face representing the stainless steel mesh were considered mesh boundaries. When a vessel encountered one of these boundaries, the outside component was disregarded and growth ended at the point where the segment intersected the boundary face. (D) Gel boundary: Unconstrained faces of the mesh were considered gel boundaries and represent the external surface of the gel that contacts the growth media. When a vessel encountered this type of boundary, its outside component was projected into the plane of the boundary face. The outside component was replaced with this projection, $v_{||}$, causing the vessel to change direction and start growing within the plane of the boundary.

$$\boldsymbol{v} = \boldsymbol{v}_i + \boldsymbol{v}_o . \tag{5.4}$$

Two types of boundaries were considered. The faces of the mesh that did not correspond to the edge of the gel space (i.e., where the gel contacts the stainless steel mesh or at symmetry planes) were considered mesh boundaries. When a new segment penetrated one of these faces while simulating growth, $\boldsymbol{v}_o$ was simply discarded (i.e., set to $\boldsymbol{0}$) and $\boldsymbol{v}$ was replaced by $\boldsymbol{v}_i$ and the growth tip was deactivated (Figure 5.4 C). The other faces of the mesh represent the edges of the construct. When a new segment was found to grow beyond one of these faces (construct boundaries), the portion of the new segment outside of the mesh, $\boldsymbol{v}_o$, was decomposed into a component that laid within the boundary face, $\boldsymbol{v}_{\|}$, and a component normal to the boundary face, $\boldsymbol{v}_{\perp}$,

$$\boldsymbol{v}_{\|} = \left(\boldsymbol{I} - \boldsymbol{n} \otimes \boldsymbol{n}\right) \cdot \boldsymbol{v}_o , \tag{5.5}$$

$$\boldsymbol{v}_{\perp} = \boldsymbol{v}_o - \boldsymbol{v}_{\|} , \tag{5.6}$$

where $\boldsymbol{n}$ is the unit normal of the boundary face. A new line segment was set to $\boldsymbol{v}_{\|}$ and this became the new growth tip of the neovessel (Figure 5.4 D). This caused vessels that encountered a construct boundary to change direction and grow along the boundary face, as it was observed that vessels exhibit this behavior upon encountering the edge of the matrix during culture [22].

5.3.6 Representation of active stress produced by microvessels

Each active sprout was assigned an active stress field $\boldsymbol{\sigma}_s$ to represent the stress generated by the sprout tip on the ECM as cells in the neovessel sprout apply traction.

To calculate the active stress at a position $\boldsymbol{x}$ inside the mesh due to a particular sprout located at $\boldsymbol{x}_s$, a distance vector $\boldsymbol{r}$ was drawn such that

$$\boldsymbol{r} = \|r\|\hat{\boldsymbol{r}} = \boldsymbol{x}_s - \boldsymbol{x}\,. \tag{5.7}$$

The active stress produced on the ECM by the sprout tip was then calculated based on the length ($\|r\|$) and orientation ($\hat{\boldsymbol{r}}$) of this vector:

$$\boldsymbol{\sigma}_s(\boldsymbol{x}) = ae^{-b\|r\|}\cos^N\left(\frac{\psi}{2}\right)\hat{\boldsymbol{r}}\otimes\hat{\boldsymbol{r}}\,. \tag{5.8}$$

This mathematical representation of the sprout stress was chosen to mimic the "fan" deformation pattern of collagen fibrils that has been observed around sprout tips during angiogenic growth [28]. The exponential term in Equation 5.8 caused sprout stresses to be localized around the sprout tip. The cosine power term, which is a function of the angle ψ, gives the stress field directionality. The angle ψ was measured between the sprout orientation vector, $\boldsymbol{v}$, and the vector $\boldsymbol{r}$ (Figure 5.5 A). The parameters a, b, and N were adjustable parameters: a scaled the magnitude of the sprout stress, b determined the range over which the sprout acts, and N controlled the width of the stress field (Figure 5.5 B, C).

5.3.7 Symmetry of sprout stress fields

Each sprout stress field was mirrored across symmetry planes to account for the influence of microvessels in the portions of the construct that were not represented by the FE mesh. The total active stress contribution from a single sprout, $\boldsymbol{\sigma}_A$, was determined by a sum of the sprout stress, $\boldsymbol{\sigma}_s$, defined by Equation 5.8 and the 7

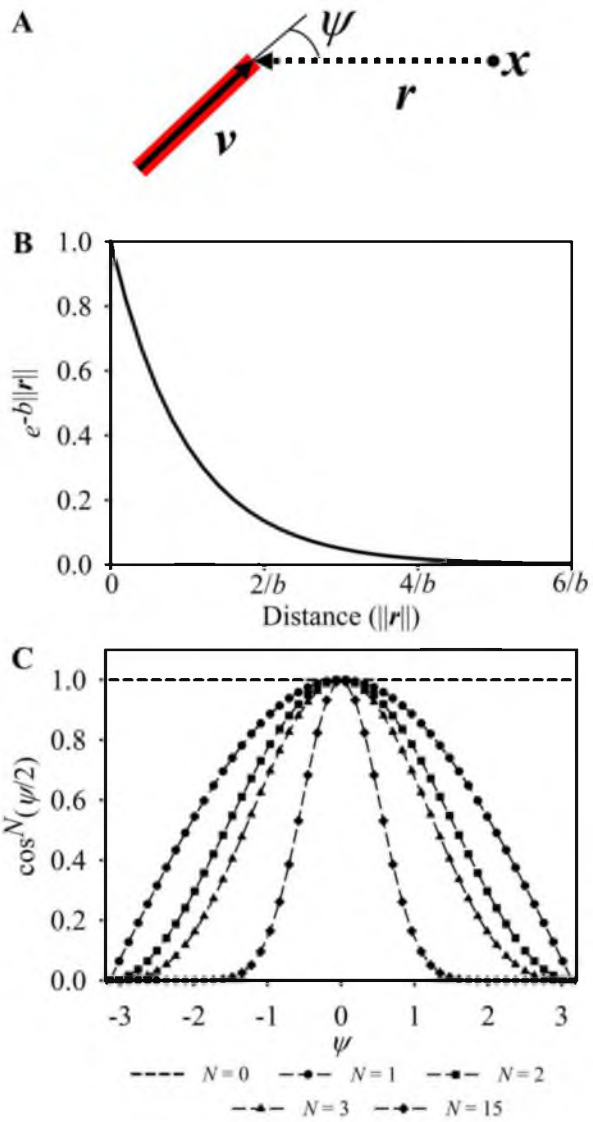

Figure 5.5: Each active sprout tip was assigned an active sprout stress field. (A) When calculating stress at a point $\boldsymbol{x}$, a vector $\boldsymbol{r}$ was drawn from $\boldsymbol{x}$ to the location of the sprout tip. The active stress applied to the mesh was calculated using Equation 5.8 and was a function of the distance away from the sprout, $\|r\|$, and ψ, the angle formed between $\boldsymbol{r}$ and the direction of the sprout, $\boldsymbol{v}$. (B) The exponential component of Equation 5.8 caused stress to exponential decrease as the distance away from the sprout increased, localizing stress around the sprout tip. By a distance of $5/b$, stress essentially drops to zero. (C) The width of the sprout stress field was controlled by N, the exponent in the cosine power term. If N was set to 0, then the stress field was isotropic and had no preferred orientation (dashed line, no markers). Setting N greater than or equal to 1 caused the majority of force to be directed into the regions directly in front of the neovessel tip, and the width of the sprout force field decreased for larger values of N.

mirrored sprout stress fields such that

$$\boldsymbol{\sigma}_A = \boldsymbol{\sigma}_s + \sum_{k=1}^{7} \boldsymbol{\sigma}'_k \,. \tag{5.9}$$

Each mirrored sprout stress field was calculated using Equation 5.8 at a mirrored sprout position, $\boldsymbol{x}'_s$. Each of the 7 mirrored sprout positions for a sprout at $\boldsymbol{x}'_s$ was calculated by the equation

$$\boldsymbol{x}'_s = \boldsymbol{x}_s + \boldsymbol{A} \cdot \boldsymbol{s}, \tag{5.10}$$

where $\boldsymbol{s}$ was a vector that contained the x-, y-, and z-coordinates of the geometric cent of the construct ($[s] = [10.25 \quad 2.75 \quad 1.5]^{\mathrm{T}}$ mm). The contents of the matrix $\boldsymbol{A}$ were dependent on which symmetry planes were being considered when calculating $\boldsymbol{x}'_s$,

$$A_{ij} = \begin{cases} A_{11} = 1 \text{ if mirroring across } yz \text{ symmetry plane, otherwise } A_{11} = 0. \\ A_{22} = 1 \text{ if mirroring across } xz \text{ symmetry plane, otherwise } A_{22} = 0. \\ A_{33} = 1 \text{ if mirroring across } xy \text{ symmetry plane, otherwise } A_{33} = 0. \\ A_{ij} = 0 \text{ if } i \neq j \end{cases} . \tag{5.11}$$

Each of the 7 mirrored stress fields was calculated by determining a mirrored sprout position based on Equation 5.10, drawing a mirrored distance vector $\boldsymbol{r}'$ using Equation 5.7, and calculating the mirrored stress using Equation 5.8.

5.3.8 Constitutive model

At any time during the simulation, the total stress at a location in the construct was determined by the sum of the active stress component $\boldsymbol{\sigma}_A$ and the passive stress response $\boldsymbol{\sigma}_P$, governed by the constitutive model, such that

$$\boldsymbol{\sigma} = \boldsymbol{\sigma}_A + \boldsymbol{\sigma}_P \,. \tag{5.12}$$

The material behavior of construct was represented with a composite constitutive model based on mixture theory [29] in order to account for the time-varying properties of the constructs as the gels were gradually vascularized during angiogenesis. The passive stress $\boldsymbol{\sigma}_P$ was defined as a weighted sum of the material behavior of the microvessels, $\boldsymbol{\sigma}_V$, and the ECM, $\boldsymbol{\sigma}_{ECM}$,

$$\boldsymbol{\sigma}_P = \phi\boldsymbol{\sigma}_V + (1-\phi)\boldsymbol{\sigma}_{ECM}, \tag{5.13}$$

where ϕ is the volume fraction of the element that is occupied by microvessels. At the beginning of culture, $\phi << 1$ and the acellular ECM component dominates the total material response. As growth progresses, ϕ increases and the total material response shifts towards the properties of the vascularized construct.

An isotropic neo-Hookean constitutive model was used to represent the material properties of the vascularized construct (modulus E_{vess}, ν = 0.0). The stress in this material due to deformation was calculated as

$$\boldsymbol{\sigma}_V = \frac{E_{vess}}{2J}(\boldsymbol{B}-\boldsymbol{I}), \tag{5.14}$$

where J is the Jacobian and $\boldsymbol{B}$ is the left Cauchy deformation tensor. A hyperelastic constitutive model based on a uniform continuous fiber distribution was used to represent the ECM [30]. This model captures the equilibrium material behavior of collagen gels including nonlinear elasticity, strain-induced anisotropy, low modulus in compression, and a strain-dependent Poisson's ratio [31]. This model consists of a fiber component that only acts in tension (with a nonlinear fiber modulus E_{fib}) embedded within a ground matrix material. The ground matrix was set as an isotropic neo-

Hookean material with modulus E_M and Poisson's ratio ν = 0.0, as water was free to leave the gel during deformation due to the slow rate of cellular loading. The total stress in this material due to deformation, $\boldsymbol{\sigma}_{ECM}$, was calculated as a sum of the stress in the ground substance and fiber components, such that

$$\boldsymbol{\sigma}_{ECM} = \boldsymbol{\sigma}_M + \boldsymbol{\sigma}_{fib}, \tag{5.15}$$

$$\boldsymbol{\sigma}_M = \frac{E_M}{2J}(\boldsymbol{B} - \boldsymbol{I}), \tag{5.16}$$

$$\boldsymbol{\sigma}_{fib} = \int_a 4E_{fib}\frac{I_n}{J}(I_n - 1)H(I_n - 1)\boldsymbol{n}\otimes\boldsymbol{n}da, \tag{5.17}$$

$$I_n = \boldsymbol{n}\cdot\boldsymbol{n} = \boldsymbol{N}\cdot\boldsymbol{B}\cdot\boldsymbol{N} \tag{5.18}$$

In these equations, I_n is the fiber invariant of the deformation and $\boldsymbol{N}$ and $\boldsymbol{n}$ are the vectors along the fiber orientation in the reference and current configuration respectively, and $H(\bullet)$ is the Heaviside step function used to ensure that these fibers only contribute stress under tension. The stress contribution from the fiber components σ_{fib} is calculated by the surface integration of a unit sphere spanned by all directions of $\boldsymbol{n}$. To accurately represent the material behavior of the native collagen gels, this constitutive model needed to represent a large disparity in stiffness in tension and compression. The two constitutive models used in this framework exhibit drastically different behavior in compression vs. tension (Figure 5.6 A, B). Experimental data obtained during uniaxial extension of hexahedral acellular collagen gels were used to calibrate the material model parameters (Figure 5.6 C) [32]. Values of the material coefficients can be found in Table 5.1.

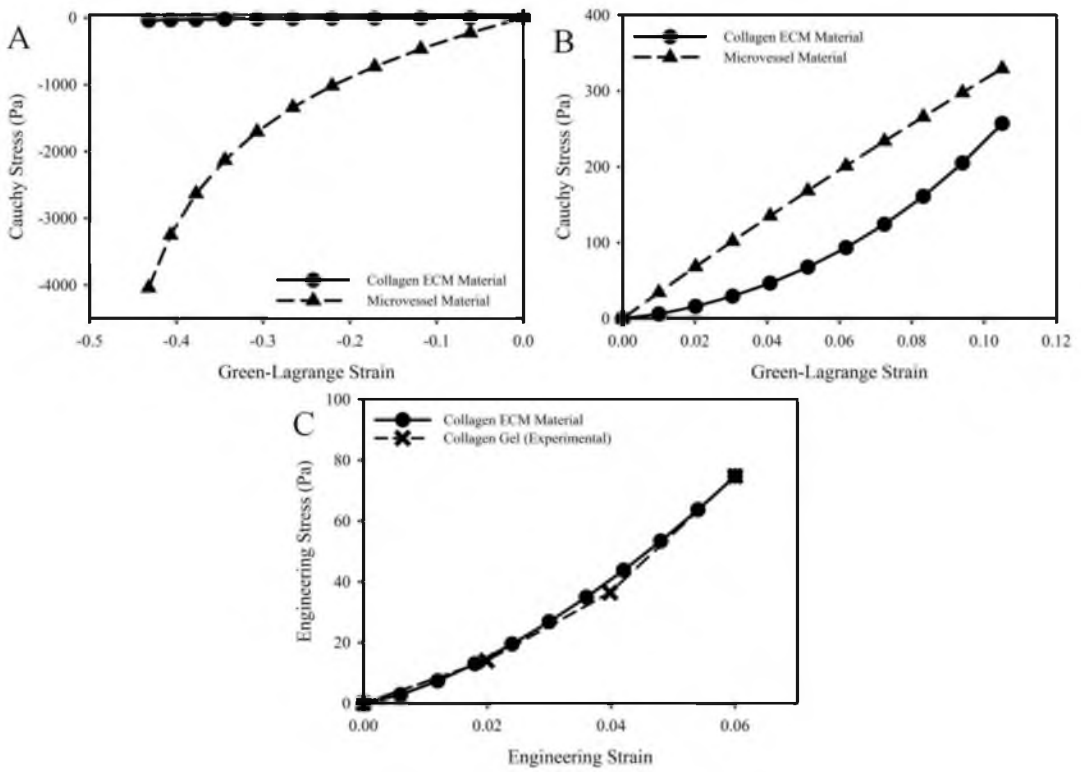

Figure 5.6: Stress-strain plots for the material model used in the simulation. A composite material was used to account for the properties of both the acellular ECM and the microvessel network. This material uses a weighted average of the ECM and microvessel stress response to determine the stress for the composite as a whole. (A) Cauchy stress vs. Green-Lagrange strain for the ECM and microvessel materials in compression. Minimum principal strain within the simulations reached -0.4. The ECM material offers very little stress to resist compression compared to the microvessel material. (B) Cauchy stress vs. Green-Lagrange strain for the ECM and microvessel materials in tension. Maximum principal strain within the simulations reached 0.1. The ECM material acts much stiffer in tension than in compression, demonstrating the tension-compression nonlinear for this material. (C) Engineering stress vs. engineering strain for the ECM material. Data from uniaxial extension of 3.0 mg/ml collagen gels were used to set the modulus of the ECM material in tension, E_{fib}. Experimental data are presented as the dashed line with "x" markers, while the material fit is presented as the solid line with circular markers. Our material model was able to produce excellent agreement with the experimental data within the range of data tested during the experiment.

Table 5.1: Baseline values for all parameters within the model. These values were used in all simulations except for during the parameter sensitivity analysis, in which the parameters were varied with respect to the baseline values listed here. The percentage that each parameter was varied during the parameter sensitivity study is listed in the column on the far right.

Parameter	Description	Value	Vary
N_{frag}	Number of initial neovessel parent fragments	2114	--
b_0	Branching probability	0.1	--
a	Sprout stress magnitude (per single sprout)	3.72 μPa	50%
b	Sprout stress range	250 μm	25%
N	Sprout stress width (cosine exponent)	2	50%
E_M	ECM constitutive model: Stiffness of ground matrix (governs compressive response)	34.52 Pa	50%
E_{fib}	ECM constitutive model: Nonlinear fiber stiffness (governs tensile response)	345.2 Pa	50%
E_{vess}	Microvessel constitutive model: Modulus	3.452 kPa	50%
τ	Viscoelastic time constant	1.08 seconds	25%

Previous research has demonstrated that stress within vascularized constructs is dissipated over a time scale of seconds [22]. This behavior is most likely due to the large water content within collagen gels. To include this behavior within the material model, viscoelastic behavior akin to a Maxwell fluid model was added. The time-varying second Piola-Kirchhoff stress, $\boldsymbol{S}(t)$, was defined as

$$\boldsymbol{S}(t) = \int_0^t G(t-s)\frac{d\boldsymbol{S}_P}{ds}ds, \tag{5.19}$$

$$G(t) = e^{-\frac{t}{\tau}}, \tag{5.20}$$

where the passive elastic stress $\boldsymbol{S}_P$ was the pull-back of the passive Cauchy stress $\boldsymbol{\sigma}_P$ as determined by Equation 5.13, $G(t)$ was the reduced relaxation function, and τ was the relaxation time constant.

5.3.9 Coupling the discrete growth model with ECM mechanics

FEBio, a nonlinear FE software, was used to solve for the deformation of the ECM in response to cellular loading [24]. The coupling between angio3d and FEBio was accomplished through AngioFE, a "plugin" file for FEBio. A plugin is a precompiled, dynamically linked library that can be associated with an executable at run-time. The AngioFE is available online for download at http://febio.org/plugins/angiofe/. AngioFE has access to all the base classes in the FEBio and angio3d libraries, allowing it to perform all the computations required for the simulation, including simulating microvessel growth, applying active stress to the mesh, and calling the nonlinear FE solver. FEBio loads the plugin file at startup and executes all tasks within AngioFE.

This framework allows users to include new functionality into their FE analysis without the need to edit and rebuild the entire FEBio source code. First, angio3d simulated a growth step using fibril orientation and matrix density information in the ECM field at time step n (Figure 5.7 A). Then, sprout stresses were applied to the mesh (Figure 5.7 B). Next, FEBio was called to solve for the deformation field using the cell-generated loading scenario (Figure 5.7 C). Finally, the deformation field predicted by FEBio was used to update microvessel position and orientation, as well as fibril orientation and density in the ECM field for the next time step n+1 (Figure 5.7 D). The next growth step in angio3d used this updated ECM field.

Microvessels were updated to the deformed configuration by interpolating nodal displacement to the location of each segment position, $\boldsymbol{x}_s$, using the shape functions within the mesh. At time step n, the current position of a segment was calculated as

$$\boldsymbol{x}_s^n = \sum_{j=1}^{8} \boldsymbol{u}_j^n N_j\left(\boldsymbol{x}_s^{n-1}\right), \tag{5.21}$$

where $\boldsymbol{u}_j^n$ was the displacement vector for node j at time n, and N_j was the shape function for node j evaluated at the previous position of the segment, $\boldsymbol{x}_s^{n-1}$. Nodal displacement $\boldsymbol{u}_j^n$ was defined as the change in position of node j between time points n and n-1. This method of updating microvessel positions meant that microvessel deformation was compatible with the deformation of the ECM.

The biophysical properties of the ECM that regulated growth were updated to the current configuration as well. Free vectors representing collagen fibril orientation were updated to the current configuration using the deformation gradient tensor, $\boldsymbol{F}$,

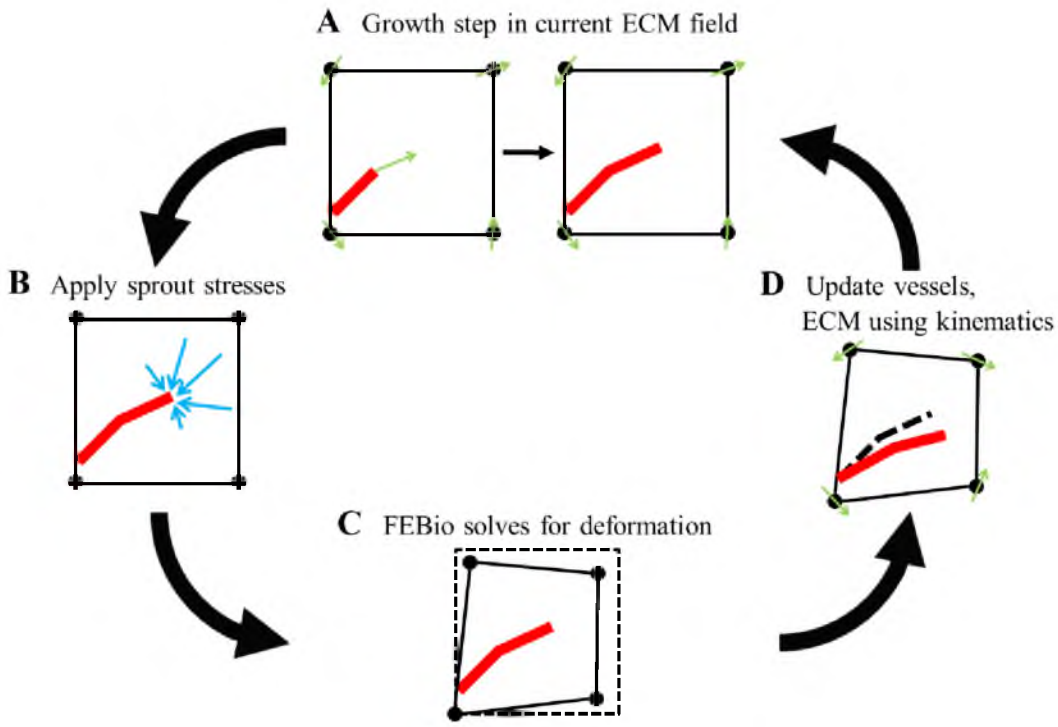

Figure 5.7: Schematic of the coupling between the discrete growth model angio3d and the nonlinear FE software FEBio. (A) First, angio3d simulated a growth step using fibril orientation and matrix density information in the ECM field at time step *n*. (B) Then, a sprout stress field was applied to the mesh at each active sprout tip location. (C) FEBio was then used to solve for the deformation caused by the sprout loading scenario. (D) Lastly, the kinematic information predicted by FEBio was used to update the growth model for the next time step *n*+1. This process included displacing and re-orientating microvessels, re-orientating collagen fibrils, and updating matrix density. The next growth step in angio3d took place in this updated ECM field.

$$\boldsymbol{\theta}_j^n = \boldsymbol{F}_j^{n-1} \cdot \boldsymbol{\theta}_j^0, \tag{5.22}$$

where $\boldsymbol{\theta}_j^n$ was the collagen fibril orientation vector for node j at time n, $\boldsymbol{F}_j^{n-1}$ was the deformation gradient tensor for node j at time n-1, and $\boldsymbol{\theta}_j^0$ was the initial fibril orientation vector for node j. Fibril orientation vectors were normalized after each update to ensure these vectors remained unit vectors. Matrix density was updated into the current configuration using the conservation of mass. Assuming the total mass of matrix within each element does not change through the simulation, but matrix density changes as the element changes volume during the deformation. The volume change is measured through the Jacobian of the deformation, $J = \det(\boldsymbol{F})$. The matrix density for node j at time n was calculated as

$$\rho_j^n = J_j^{n-1}\rho_j^0 = \det \boldsymbol{F}_j^{n-1}\rho_j^0, \tag{5.23}$$

where J_j^{n-1} was the Jacobian for node j at time n-1 and ρ_j^0 was the initial matrix density for node j. After this update, AngioFE then began the next time step n+1 and called angio3d to calculate the next growth step within the updated ECM field.

5.3.10 Simulation of angiogenesis within rectangular constructs

Initial microvessel fragments were seeded in a random distribution within the simulation domain based on the seeding density in the experiments. Unless otherwise noted, parameters were prescribed at the values listed in Table 5.1. The ECM material coefficients were fit to experimental testing of acellular collagen gels and the vessel material coefficient was scaled relative to this experimentally determined value [32]. The value for the branching probability b_0 was determined in a previous study [18].

The sprout stress magnitude a was determined by matching gel contraction in the LAC simulations to measurements from the experiments. The other sprout stress parameters b and N were prescribed in order to re-create the "fan-shape" deformation patterns seen in collagen fibrils using live two-photon imaging of angiogenic neovessels [28].

In the first study, we performed a mesh convergence study by running simulations at various levels of mesh resolution. Convergence was based on the contractile strains predicted by the simulations. Three simulations were run at each mesh resolution with different seedings of the random number generator. Contraction was considered converged once the difference between predictions of contraction for the next mesh resolution level dropped below a predetermined threshold (ε = 1e-3). After the required mesh resolution was determined, microvessel alignment was measured at the geometric center of the gel, corresponding to the region that was imaged during the experiments. Then, a parameter sensitivity study was performed on the model. The three sprout stress parameters (a, b, N) and four material coefficients (E_M, E_{fib}, E_{vess}, τ) were all increased and decreased by 50% (25% in the case of some parameters due to high sensitivity) of their baseline values in Table 5.1. Three simulations were performed for each parameter variation at the same random seeds used for the mesh resolution determined in the convergence study. Sensitivity was quantified by normalizing the percent change in contraction by the percent change in the parameter.

After the mesh convergence study and parameter sensitivity studies were completed using the LAC geometry and boundary conditions, the modeling framework was used to predict growth in two additional rectangular boundary conditions: unconstrained (UNC), and short-axis constrained (SAC). The converged mesh from the LAC

simulations was used and the boundary conditions were modified accordingly. Contraction and microvessel alignment were measured at the geometric center of the construct from each simulation and the data were compared to data from the constrained construct experiments. A two-tailed Student's t-test with unequal variance (Welch's t-test) was performed between experimental and computational gel contraction data to detect any statistical difference (α = 0.05). If a statistical difference could not be detected, a TOST-test (Two One-Sided T-test [33]) was performed to test for statistical equivalence (α = 0.05, Θ= 0.3).

5.3.11 Simulation of angiogenesis within circular constructs

Angiogenesis was also simulated in circular constructs in order to further demonstrate the capabilities of the framework using alternative matrix geometry and boundary conditions. We have previously cultured circular vascularized constructs, both unconstrained and constrained, in previous experimental efforts [18, 22]. The circular constructs had a diameter of 15.0 mm and a thickness of 2.8 mm in the *z* direction to match the dimensions of circular vascularized constructs in previous experiments (see Chapter 4). The $1/8^{th}$ symmetry model of the circular constructs were used and nodes along the *xy*-, *xz*-, and *yz*- symmetry planes were constrained in the *z*, *y*, and *x* directions, respectively. The unconstrained (CU) constructs had no additional boundary conditions, while the circular constrained (CC) had displacement fully constrained along the circumference. The parameter set for these simulations was identical to the rectangular construct simulations listed in Table 5.1. At the conclusion of each simulation, the deformed radius of the construct was measured at an angle of

45° with respect to the x and y axes and used the calculate radial gel contraction (ε_{rr}) and the deformed thickness was used to calculate gel contraction in the z direction (ε_{zz}).

5.4 Results

Growth in the vascularized constructs was consistent throughout all experiments. Neovessels sprouts from parent vessel fragments were evident at Days 2-3, and each experiment resulted in a well-established microvascular network within the construct by Day 6. Gel contraction and microvessel alignment data from the experiments resembled data from previous studies [22]. In the LAC simulations, the free faces of the construct contracted inward forming a "neck" shape, with the most contraction occurring at the right side of the mesh corresponding to the center of the construct (Figure 5.8). Each simulation resulted in a deformed mesh that closely resembled the shape of the constrained constructs at Day 6.

In order to determine a mesh resolution for which contraction in y and z was fully converged, we ran simulations with increasing mesh resolution. As mesh resolution was increased, contraction along the y and z axes converged toward ~0.36 and ~0.30, respectively (Figure 5.9 A). Contraction in y (ε_{yy}) and contraction in z (ε_{zz}) were both converged at a mesh resolution of 784 elements. Contraction results from the 784-element simulations were within one standard deviation of contraction measured in the experiments (Figure 5.9 B). Microvessels within the experiments were highly aligned along the long-axis of the construct (i.e., the constrained axis) at Day 6 of growth, and the computational model predicted similarly aligned microvasculature in the simulation of a LAC gel (Figure 5.10).

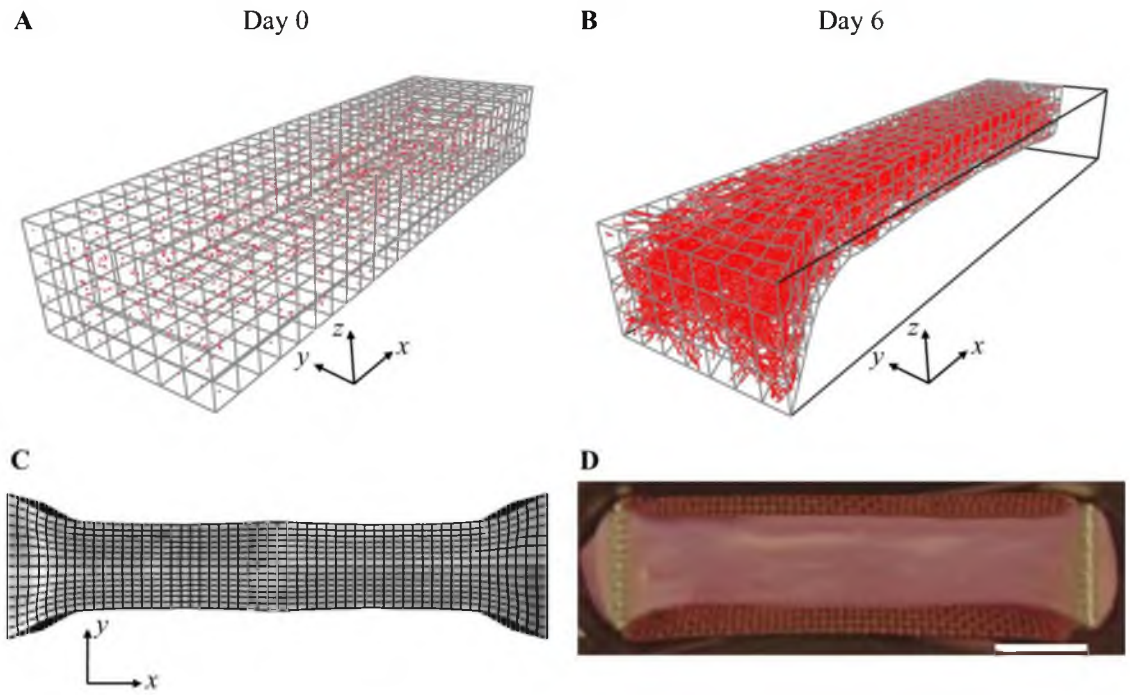

Figure 5.8: Simulation of a long-axis constrained (LAC) vascularized gel. These results used the converged mesh resolution determined during convergence study. (A) At Day 0, the mesh was seeded with initial microvessel fragments. (B) At Day 6, the gel has become highly perfused by microvessels and has deformed into a "neck" shape as seen in the LAC experiments. (C) Full-geometry construction of the gel as predicted by the deformed FE mesh. (D) The deformed gel geometry predicted in the simulation closely resembled the shape of long-axis constrained vascularized gels at Day 6. Scale bar 2 mm.

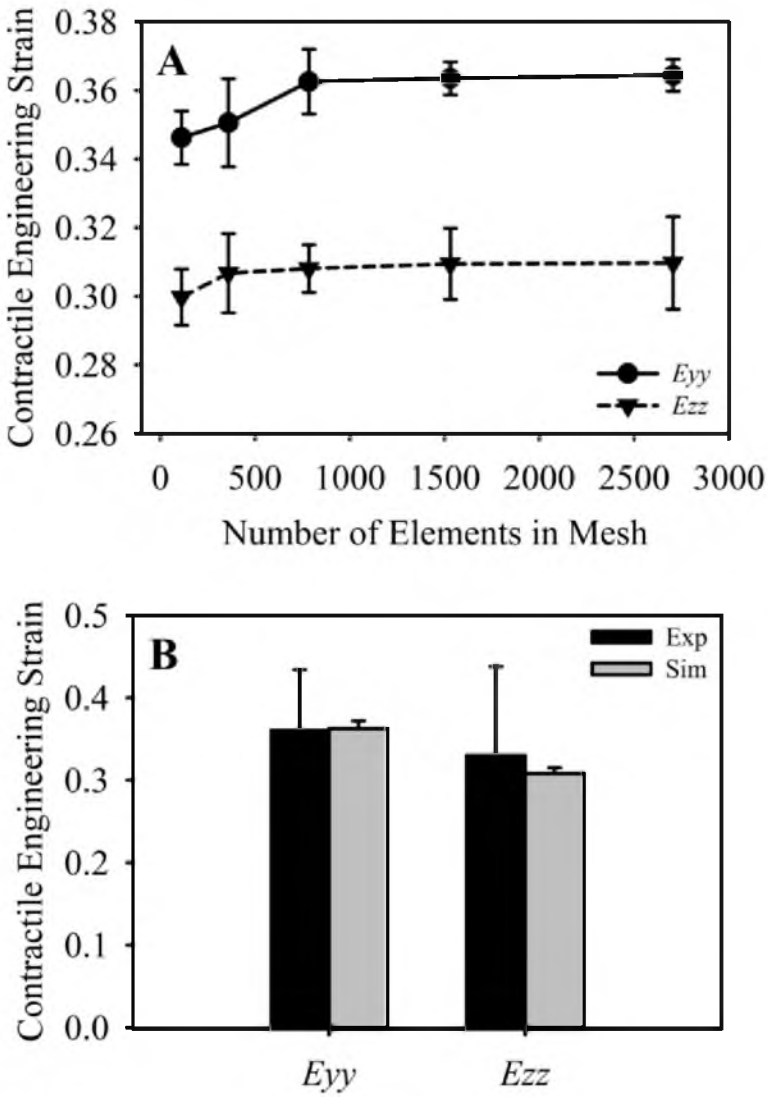

Figure 5.9: Mesh convergence and gel contraction. (A) Mesh convergence was determined by running simulations with increasing levels of mesh refinement. Convergence was determined when predictions of contraction differed less than 1e-3 from results using the next mesh refinement level. Contraction in *y* and *z* were both converged at a resolution of 784 elements. (B) Engineering strain (gel contraction) from the experiments, shown in black, and the 784-element simulations, shown in gray. The model was able to produce good predictions of gel contraction, as values of ε_{yy} and ε_{zz} where both within one standard deviation of contraction measured in the experiments.

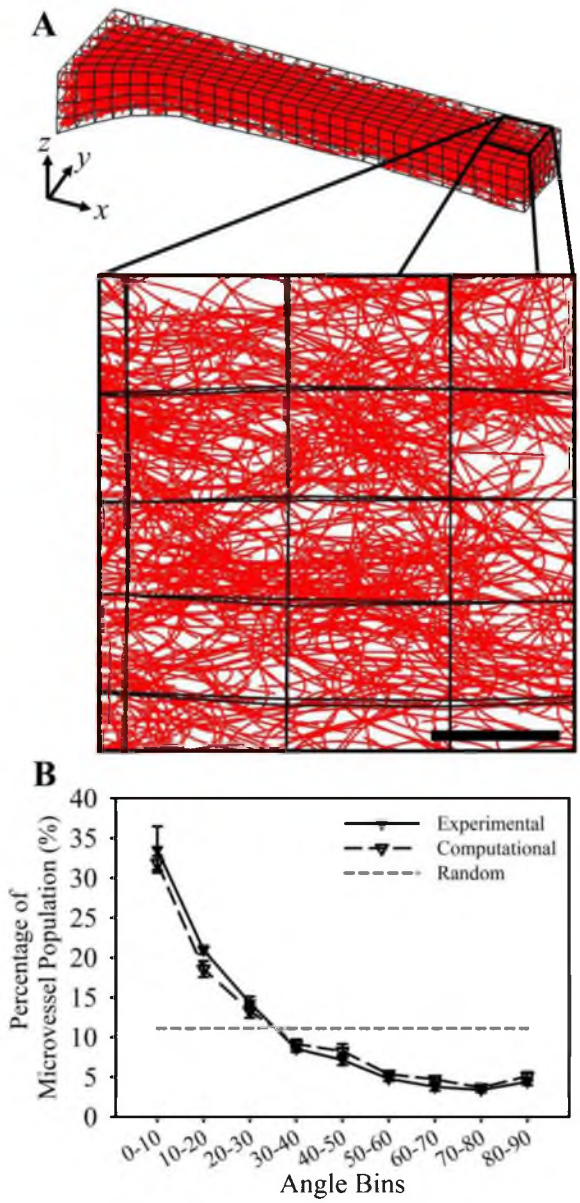

Figure 5.10: Microvessel alignment. (A) The computational model predictions of aligned microvessels within a LAC gel. The subset of microvessels shown below is a z-projection of microvessels at the geometric center of the gel (the right side of the mesh) and corresponds to the region of that was imaged using confocal microscopy. Scale bar 300 μm. (B) The computational model predicted a distribution of microvessel alignment that was in excellent agreement with experimental measurements. Measurements were obtained by measuring the angle that each vessel formed with respect to the long-axis (*x*-axis) of the gel. Microvessels within the experiments and simulations were both highly aligned along the long-axis as seen in the large amount of vessels within the more acute angle bins. The gray dashed line illustrates expected data for a random network.

The sensitivity analysis of the sprout stress parameters demonstrated that the model was most sensitive to *b*, the parameter controlling the sprout stress range, while changes in the magnitude *a* and the width of the stress field, controlled by *N*, had much less of an effect (Figure 5.11 A). There was little to no difference in sensitivity between ε_{yy} and ε_{zz}. Increasing the sprout stress range by decreasing the parameter *b* caused a more pronounced change in gel contraction than increasing *b*. The model predictions were sensitive to changes in the viscoelasticity relaxation time constant, τ, while contraction was relatively insensitive to changes in the other parameters of the constitutive models (Figure 5.11 B). Decreasing the time constant sped up the rate of stress dissipation within the simulations, and the model was more sensitive to decreases in the time constant than increases. Additionally, the model was more sensitive to changes in the compressive modulus of the ECM material E_M than the tensile modulus E_{fib} and showed roughly the same preference for E_{vess} as E_M .

Simulations of each construct boundary condition (UNC, LAC, SAC) predicted a deformed construct geometry and vascular alignment that closely resembled data from the constrained gel experiments (Figure 5.12). Contraction measured for each boundary condition was statistically indistinguishable from experimental data via Student's t-test. Additionally, a statistical equivalence was detected between experimental and computational data via TOST-test for the following datasets: ε_{xx} and ε_{yy} for the UNC gels, ε_{yy} for the LAC gels, and ε_{xx} for the SAC gels. Deformation in the UNC case was essentially isotropic (Figure 5.12 A), while the LAC constructs deformed only along the

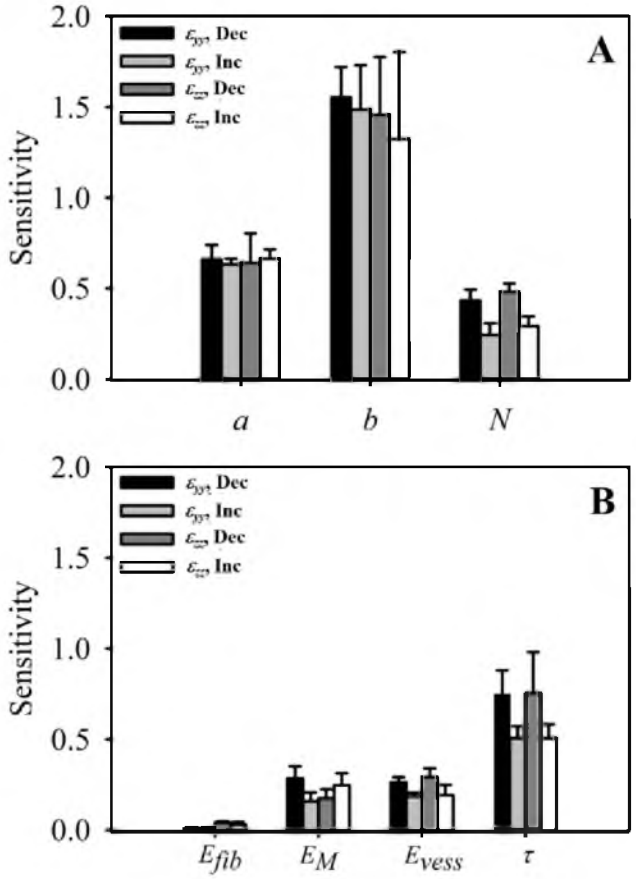

Figure 5.11: Sensitivity analysis of the model parameters associated with the sprout stress field and material model. Numerous simulations were run as each parameter was increased or decreased. The percent change in contraction that occurred in response to the variation in the parameter was collected. We normalized this value by the percent change in the parameter to quantify sensitivity. Variation in ε_{yy} as each parameter decreases or increases can be seen in black and light gray, respectively. Variation in ε_{zz} as each parameter decreases or increases can be seen in dark gray and white, respectively. (A) Sensitivity analysis of the sprout stress parameters: *a* (magnitude), *b* (range), and *N* (controls the width of the stress field). The model was highly sensitive to changes in *b*, and was more sensitive to decreases in this parameter rather than increases. The model was relatively insensitive to the other two sprout stress parameters. (B) Sensitivity analysis for the material model parameters: E_{fib} (tensile modulus of ECM material), E_M (compressive modulus of ECM material), E_{vess} (modulus of the microvessel material, and τ (time constant for viscoelastic relaxation). Gel contraction was most sensitive to changes in the viscoelastic relaxation time, while relatively insensitive to the other parameters. Contraction was also more sensitive to variations in the compressive modulus for the ECM material (E_M) compared to changes in the tensile modulus (E_{fib}).

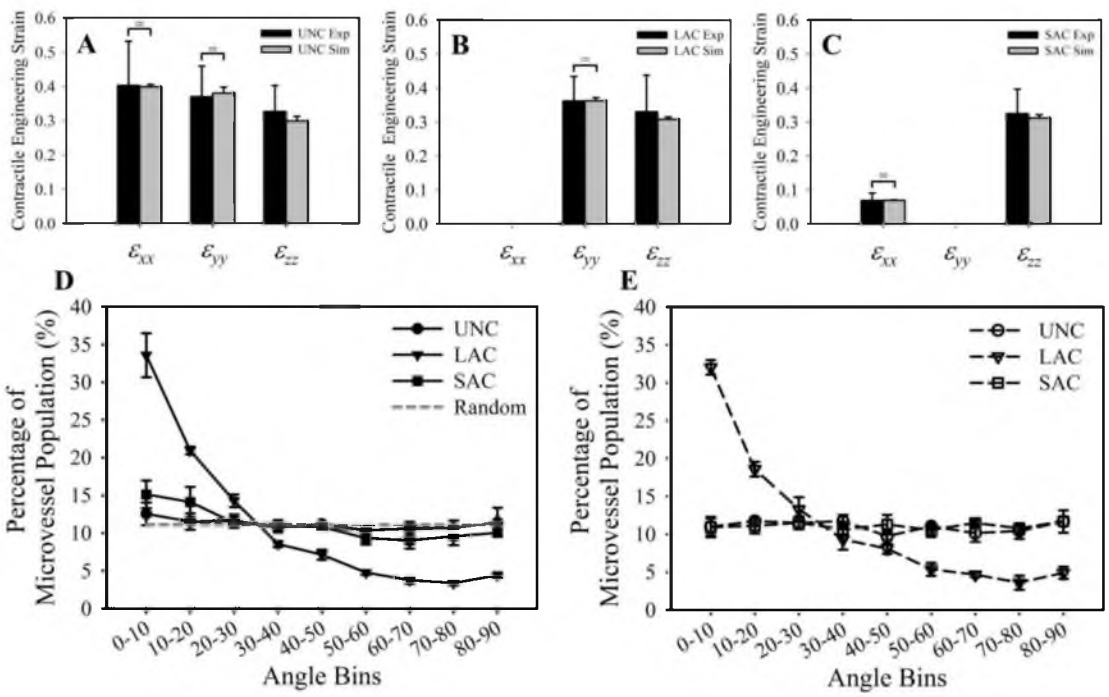

Figure 5.12: Gel contraction and microvessel alignment for each of the three boundary conditions. (A-C) Engineering strain (gel contraction) was measured at the geometric center of each construct for the unconstrained (A), long-axis constrained (B), and short-axis constrained (C) constructs. Experimental measurements are shown in black, computational predictions of gel contraction are in gray. Statistical equivalence as detected by TOST-test is indicated by the bracket and equal sign. (D, E) Distributions of microvessel alignment with respect to the long-axis (*x*-axis) of the gel measured from the experiments (D) and predicted by the simulations (E). Microvessels in the LAC experiments were highly aligned along the long-axis, while randomly oriented in the UNC and SAC conditions. The computational simulations accurately predicted microvessel alignment in each of the three boundary conditions.

y and *z* directions due to the boundary constraint (Figure 5.12 B). In the SAC constructs, the long-axis was unconstrained but still effectively stiff along this direction due to the long aspect ratio of the construct resulting in very little contraction along *x* (Figure 5.12 C). Vascular alignment predicted in simulations of each boundary condition closely resembled alignment data measured in the experiments (Figure 5.12 D, E). The simulation accurately predicted randomly aligned microvessel in the UNC and SAC constructs and vessels aligned along the long-axis in the LAC constructs (Figure 5.12 E).

Angiogenesis was simulated within circular constructs as well (Figure 5.13). Circular unconstrained (CU) constructs contracted inwards towards the geometric center of the mesh, contracting radially (and circumferentially) by $\varepsilon_{rr} = \varepsilon_{\theta\theta} = 0.195$ and through the thickness by $\varepsilon_{zz} = 0.135$ (Figure 5.13 C, F). Microvessels were aligned perpendicular to the radial contraction (i.e., circumferentially aligned) in the contracted regions of the gel near the deformed edge, while vessels within the center of the gel were randomly aligned within the *xy*-plane. These contraction and microvessel alignment results are similar to what we have found in previous experiments [18, 22], although contraction was more pronounced in our experiments than in these simulations. In the simulation of a circular constrained (CC) construct, radial and circumferential contraction was constrained but the gel was still free to contract through the thickness by $\varepsilon_{zz} = 0.209$ (Figure 5.13 D, G). Microvessels within this construct were randomly aligned with the *xy*-plane, similar to what we have found in previous circular constrained gel experiments [22].

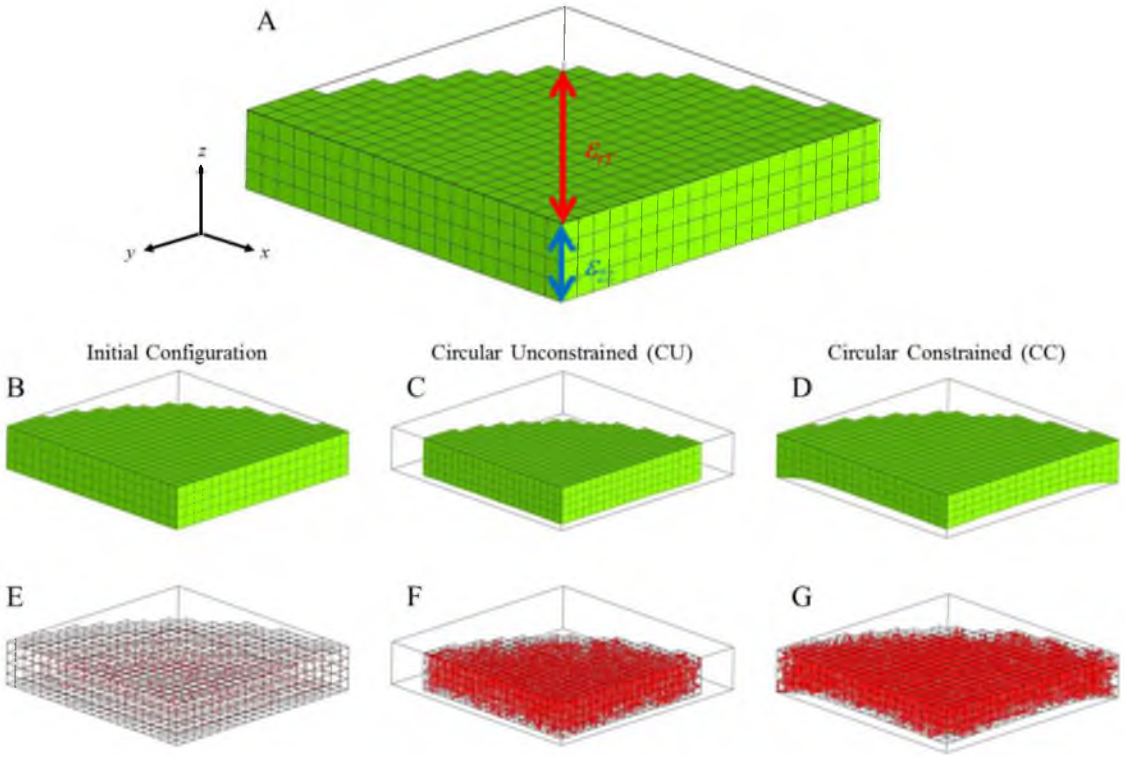

Figure 5.13: Simulation of angiogenesis within a circular construct. (A) Initial geometry of the circular construct. A 1/8th symmetry model was used to reduce computational cost. Gel contraction along the radial direction (ε_{rr}) was measured along the top surface at an angle of 45° with respect to the x and y axes (red line). Gel contraction through the thickness (ε_{zz}) was measured at the geometric center of the construct (blue line). (B) Initial geometry of the circular construct at Day 0, (C) deformed geometry of the CU construct at Day 6, (D) deformed geometry of the CC construct at Day 6. The CU construct contracted inward towards the geometric center during the simulation, while the CC construct only contracted along the thickness of the construct. (E) Initial microvessel fragments at Day 0, (F) microvessels in the CU construct at Day 6, (G) microvessels in the CC construct at Day 6.

5.5 Discussion

We developed, implemented and performed a global validation of a computational framework that simulated angiogenic growth coupled to matrix deformation. The coupled growth model accurately predicted gel contraction and microvessel alignment during simulations of each of the rectangular boundary conditions. The model predicted random alignment within the UNC and SAC simulations and aligned microvasculature when simulating the LAC constructs, similar to what we found in the vascularized construct experiments. There are two mechanisms in the modeling framework that regulate microvessel alignment. The first mechanism for alignment occurs as microvessels convect with the anisotropic deformation of the matrix. This mechanism results from interpolating nodal displacement predicted by FEBio to the microvessel and can be interpreted as passive alignment. If the deformation field generated by sprout forces was isotropic, microvessels grew and deformed equally in all directions with no preferred orientation, as was the case for UNC constructs. However, in the LAC case the presence of the boundary constraint caused the construct to undergo anisotropic deformation. In the LAC constructs the length of the construct was fixed along the constrained axis as the construct contracted laterally. This displacement caused vessels to move inward along the y and z directions as these dimensions of the construct contracted, leaving the microvessels oriented along the x-axis. In the SAC case, the high effective stiffness prevented the construct from deforming along the long-axis, so ε_{xx} was considerably reduced. However, ε_{zz} was unaffected in this case so microvessels were contracted along z and randomly aligned within the xy-plane, similar to the UNC case.

The second alignment mechanism occurs as microvessels grow along collagen fibrils, which themselves become aligned passively. This is often referred to as contact guidance. As the construct contracted, the orientation of collagen fibrils was updated by the deformation gradient. In the LAC case, the deformation of the construct caused fibril orientation vectors to contract along the y and z direction, leaving these vectors aligned along the x-axis. This further caused neovessels to align along the constrained axis as the vessels received directional cues from the collagen fibrils through contact guidance. This can be interpreted as an active alignment mechanism, as it results from neovessels receiving information from the ECM, integrating these signals, and then growing along a certain direction based on this signal. For example, such a signal could be available binding sites along the length of aligned collagen fibrils. A distinct advantage of this modeling framework is that the mechanisms for passive and alignment can be deactivated individually. In doing so, we observed that passive alignment is the predominate mechanism governing microvessel alignment in these cultures. The addition of active alignment improved the accuracy of predictions, but the results were much more sensitive to the passive alignment mechanism. Additionally, alignment results were sensitive to the angle formed by new sprouts during branching. Previous formulations of the model enforced perpendicular sprouts when calculating branching, but we found that this reduced vascular alignment in the simulations as vessels sprouting from aligned microvessels in the later stages of the simulation were formed perpendicular to the preferred alignment direction and could not align quickly due to the persistence growth component. Scaling the projector tensor formed by the outer product of $\boldsymbol{v}$ in Equation 5.3 by one-half ensured that new sprouts still grew divergent

from the parent sprout but facilitated better alignment of new vessels along collagen fibrils, improving alignment results in the simulations.

The model presented here presents a unique approach to modeling angiogenesis and tissue morphogenesis. The deformation of the macroscale was driven by cellular biomechanical activity at the microscale. The coupling of the discrete angiogenic growth model to FEBio allowed the model to track information at the small scale while resolving deformation at the macroscale. Individual neovessel sprouts generated localized stress fields that change position as the matrix deformed and neovessels grew. New stress fields were added when a new branch point emerged, stress fields were removed due to an anastomosis. By using a continuous field to represent each sprout stress field, we did not have to homogenize stress over the mesh; rather, stress could be calculated at any required location (see Equations 5.7, 5.8). The use of the FE method provided the means to homogenize the various discrete microscale aspects within the model across the continuum. Shape functions within the mesh were used to interpolate ECM fibril orientation, matrix density, and nodal displacement to the microscale. The material properties of the vascular network were homogenized using the volume fraction ϕ within the composite material model (see Equation 5.13). The microvascular network was represented using a simple isotropic material, but the framework could be expanded to include an orthotropic material to represent the anisotropy induced by vascular alignment. The use of the dynamic discrete growth model to simulate angiogenesis allowed our framework to include the path-dependent aspects of angiogenesis as well. Growth was applied over discrete time steps using current information from the vascular network and ECM field. At the end of each time step,

both the vascular components and the ECM field was updated using the kinematics information predicted by FEBio (i.e., displacing and re-orientating sprouts, re-orientating collagen fibrils, and updating density). This created the dynamic link between cellular biomechanical activity and the matrix that exists during angiogenesis. Due to these features, we believe that this modeling framework presents a unique framework to investigate the complex biomechanical regulation of morphogenic processes such as angiogenesis that have often proven difficult to study in the past.

ECM contraction was sensitive to changes in the stress field that neovessels applied to the ECM during growth. This result was expected. In our model, the sprout force field represented the force applied directly at the focal adhesions and how these forces were transmitted through the ECM, as the fibrillar structure of the matrix was not represented explicitly. Contraction was particularly sensitive to the range over which these sprout force fields acted, controlled by the parameter b. Microvessels in our constructs were cultured in growth media supplemented with VEGF, an important growth factor during angiogenesis. VEGF binding to the receptor VEGFR2 in endothelial cells leads to the production of stress fibers and focal adhesions, the motility and contractility machinery of the cell, through the Rho-ROCK (Rho Kinase) pathway [34, 35]. As endothelial cells apply traction at focal adhesions attached to the ECM, collagen fibrils are pulled toward the sprout tip, condensing and re-orienting towards the sprout in a characteristic "fan" pattern [28]. The deformation generated by neovessel sprouts extended up to 1000 μm from the sprout tip [28]. Using this information, we set the b to 1/250 μm-1, which caused the exponential function in Equation 5.8 to effectively drop to zero at a distance of 1000 μm. The parameter a

controlled the magnitude of the sprout force field and was optimized to match the contraction results from the LAC construct experiments. The width of the "fan" shape was controlled by N, the exponent on cosine in Equation 5.8. We used a cosine power term as the exponent on the cosine term caused force to be directed in front to the vessel, and we estimated the value of N from data from Kirkpatrick et al. [28]. Additionally, we found that making the sprout force field too narrow by choosing a high value of N caused unequal contraction along y and z. In the experiments, contraction was essentially equal along y and z, and the ratio of ε_{zz} to ε_{yy} was ~0.9. The simulations predicted a ratio ε_{zz} to ε_{yy} of ~0.8 for values of $N = 0$ (isotropic) up to $N = 3$, at which point the ratio began to decrease. At $N = 15$, the ratio of ε_{zz} to ε_{yy} dropped below 0.6, indicating that making the sprout force fields too narrow produced unrealistic contraction.

In these initial simulations, materials were represented using relatively simple constitutive models. The constitutive model used in the simulations can be interpreted as a simple spring and dashpot connected in series with an active contractile element connected in parallel. The sprout stress parameters controlled the load applied to the system by active contraction, the elastic material parameters E_{fib}, E_M and E_{vess} controlled the response of the spring, while the time constant τ controlled the response of the dashpot. When choosing the constitutive models and setting values for the parameters, we had to account for the changes that occurred in the vascularized constructs during culture. The tensile modulus of the ECM material, E_{fib}, was determined to fitting the material to experimental data from uniaxial testing of 3.0

mg/ml collagen gels (Figure 5.6 C) [32]. We prescribed the other two moduli, E_M and E_{vess}, relative to this experimentally-determined value. During the development of the model, we found that a large discrepancy between stiffness in tension and compression was required in order for the constructs to deform realistically. For example, if a standard neo-Hookean material was set at the modulus determined from the uniaxial testing data, the constructs would tend to twist and buckle rather than contract inward as seen in the experiments, as the neo-Hookean material has the same modulus in tension and compression. In order to ensure sufficient tension-compression nonlinearity and realistic deformation of the type-I collagen gel during our simulations, we set the compressive modulus of the ECM material, E_M, to by 10× less than the tensile modulus E_{fib}.

We found that model predictions were more sensitive to the compressive modulus than the tensile modulus, as the deformation of the construct primarily involves contraction. In the LAC simulations, E_{fib} only scales the magnitude of tension that develops along the constrained axis while E_M controls how the construct deforms at the beginning of the simulation while the construct is primarily acellular. The microvessel material model exerts its control on contraction as the construct becomes increasingly vascularized and the microvessel volume fraction increases. Contraction in simulations involving variations in E_{vess} only deviate from the baseline simulations at ~Day 4. We have found through mechanical testing that the vascularized constructs become ~1.5× more stiff during culture as angiogenic neovessels apply traction, secrete proteases, and generate new cell-matrix adhesions [19]. In our simulations, the volume fraction of

microvessels was used to weight the stress response from the microvessel material model, and this volume fraction on average reached a maximum of about ~0.015 by Day 6. Therefore, we set the microvessel material modulus E_{vess} to be 100× the stiffness of the ECM compressive modulus, E_M, in order to cause this increase in stiffness. Note that the microvessel material is meant to actually represent the properties of the vascularized construct as a whole. The composite material model is designed to slowly transition from properties of an acellular collagen construct to a mature vascularized construct as the volume fraction of microvessels slowly increases during growth.

Of the material parameters within the model, contraction and thus vascular alignment was most sensitive to changes in τ, the viscoelastic relaxation time constant. In previous research, we observed that constrained vascularized constructs treated with Cytochalasin-D to prevent cell-generated contraction did not retract after being cut away from the constraint [22]. These results led us to postulate that stress is dissipative rather than accumulative in these constructs, and that stress relaxation occurs within several seconds. Therefore, we set τ to 1.09 seconds, causing the reduced relaxation function to reach near complete relaxation in ~4-5 seconds. In the simplified version of the material model, the viscoelastic component acts as a dashpot. The force in the dashpot is proportional to the time constant τ and the rate of deformation, therefore decreasing τ while keeping the amount of cell-generated loading unchanged causes the rate of deformation to increase. Contraction vs. time in the simulations with a decreased τ had a steeper slope than baseline simulations with larger values of τ.

Although we were able to prescribe a value of τ based on the experiments involving Cytochalasin-D, future experiments could track construct deformation over time, allowing us to confirm that the rate of deformation and the time constant within our model are truly valid. Additionally, the amount of viscous stress dissipation may not stay constant over the culture. The rate of dissipation could change as neovessels contract, remodel, and expunge water from the fibrillar structure of the matrix, and adding a time-varying time constant to our simulations would allow us to include this behavior.

Other theoretical and computational approaches have been utilized to study the role of mechanical interactions between cells and the ECM during tissue growth [36-40]. Although numerous mathematical and computational approaches have been utilized to study angiogenesis [41, 42], to our knowledge no computational models have ever been proposed to study the coupling between mechanical interactions with the ECM and neovessel growth during angiogenesis. The most relevant study demonstrated that cell-generated traction forces produce alignment perpendicular to gel contraction by modeling the fibroblast-mediated compaction of collagen gels [38]. Matrix compaction was driven by an active stress that depended on cell concentration and orientation. The active stress parameter in their study was 1.4×10-7 N•cm/cell. For comparison, active stress in our model based on the initial seeding concentration of fragments was 7.44×10-15 N•cm/fragment. However, differences between approaches prevent a direct comparison. Parameters reported by Barocas and Tranquillo were normalized per cell, cells were treated as a continuous component of a biphasic material, and their formulation for active stress was homogenous and applied to the entire domain.

Nevertheless, the similarity of predictions related to the effects of cell-generated traction forces is encouraging, and suggests that our approach could be extended to other biological processes that involve discrete cellular structures that mechanically interact with the ECM in three-dimensions including mechanotaxis, tumor growth, neurogenesis, wound healing, embryonic development, and tissue morphogenesis. Our approach accommodates the extension to include other physics such as solute transport, convection, reaction and diffusion, and many of these capabilities have been added to the FEBio framework recently [43, 44].

5.6 References

[1] Chung, A.S. and Ferrara N. (2011) "Developmental and pathological angiogenesis," Ann Rev Cell Develop Biol 27:563-84.

[2] Egginton, S., Hudlicka, O., Brown, M.D., Walter, H., Weiss, J.B., and Bate, A. (1998) "Capillary growth in relation to blood flow and performance in overloaded rat skeletal muscle," J App Physiol 85:2025-32.

[3] Jaffe, R.B. (2000) "Importance of angiogenesis in reproductive physiology," Seminars in Perinatology 24:79-81.

[4] Annex, B.H. (2013) "Therapeutic angiogenesis for critical limb ischaemia," Nature Revs Cardiol 10:387-96.

[5] Carmeliet, P. (2004) "Manipulating angiogenesis in medicine," J Intern Med 255:538-61.

[6] Ellis, L.M., Rosen, L., and Gordon, M.S. (2006) "Overview of anti-VEGF therapy and angiogenesis. Part 1: Angiogenesis inhibition in solid tumor malignancies," Clinic Advs Heatol Oncol 4:suppl 1-10; quz 1-2.

[7] Folkman, J. (1997) "Angiogenesis and angiogenesis inhibition: An overview," EXS 79:1-8.

[8] Peirce, S.M. and Skalak, T.C. (2003) "Microvascular remodeling: A complex continuum spanning angiogenesis to arteriogenesis," Microcirc 10:99-111.

[9] Bouhadir, K.H. and Mooney, D.J. (2001) "Promoting angiogenesis in engineered tissues," J Drug Targeting 9:397-406.

[10] Novosel, E.C., Kleinhans, C., and Kluger, P.J. (2011) "Vascularization is the key challenge in tissue engineering," Adv Drug Deliv Revs. 63:300-11.

[11] Phelps, E.A. and Garcia, A.J. (2010) "Engineering more than a cell: Vascularization strategies in tissue engineering," Curr Opin Biotechnol 21:704-9.

[12] Conway, E.M., Collen, D., and Carmeliet, P. (2001) "Molecular mechanisms of blood vessel growth," Cardiovasc Res 49:507-21.

[13] Ingber, D.E. (2002) "Mechanical signaling and the cellular response to extracellular matrix in angiogenesis and cardiovascular physiology," Circ Res 91:877-87.

[14] Shiu, Y.T., Weiss, J.A., Hoying, J.B., Iwamoto, M.N., Joung, I.S., and Quam, C.T. (2005) "The role of mechanical stresses in angiogenesis," Crit Revs Biomed Engng 33:431-510.

[15] Vernon, R.B. and Sage, E.H. (1999) "A novel, quantitative model for study of endothelial cell migration and sprout formation within three-dimensional collagen matrices," Microvasc Res 57:118-33.

[16] Pries, A.R. and Secomb, T.W. (2005) "Control of blood vessel structure: Insights from theoretical models," Am J Physiol Heart Circ Physiol 288:H1010-5.

[17] Chang, C.C., Krishnan, L., Nunes, S.S., Church, K.H., Edgar, L.T., Boland, E.D., Weiss, J.A., Williams, S.K., and Joying, J.B. (2012) "Determinants of microvascular network topologies in implanted neovasculatures," Arterioscler Thromb Vasc Biol 32:5-14.

[18] Edgar, L.T., Underwood, C.J., Guilkey, J.E., Hoying, J.B., and Weiss, J.A. (2014) "Extracellular matrix density regulates the rate of neovessel growth and branching in sprouting angiogenesis," PloS One 9:e85178.

[19] Krishnan, L., Hoying, J.B., Nguyen, H., Song, H., and Weiss, J.A. (2007) "Interaction of angiogenic microvessels with the extracellular matrix," Am J Physiol Heart Circ Physiol 293:H3650-8.

[20] Krishnan, L., Underwood, C.J., Maas, S., Ellis, B.J., Kode, T.C., and Weiss, J.A. (2008) "Effect of mechanical boundary conditions on orientation of angiogenic microvessels," Cardiovasc Res. 78:324-32.

[21] Nunes, S.S., Krishnan, L., Gerard, C.S., Dale, J.R., Maddie, M.A., and Hoying, J.B. (2010) "Angiogenic potential of microvessel fragments is independent of the tissue of origin and can be influenced by the cellular composition of the implants," Microcirc 17:557-67.

[22] Underwood, C.J., Edgar, L.T., Hoying, J.B., and Weiss, J.A. (2014) "Cell-generated traction forces and the resulting matrix deformation modulate microvascular alignment and growth during angiogenesis," Am J Physiol Heart Circ Physiol, 307: H152-64.

[23] Edgar, L.T., Sibole, S.C., Underwood, C.J., Guilkey, J.E., and Weiss, J.A. (2013) "A computational model of in vitro angiogenesis based on extracellular matrix fibre orientation," Comp Meths Biomech Biomed Engng 16:790-801.

[24] Maas, S.A., Ellis, B.J., Ateshian, G.A., and Weiss, J.A. (2012) "FEBio: Finite elements for biomechanics," J Biomech Engng 134:011005.

[25] Hoying, J.B., Boswell, C.A., and Williams, S.K. (1996) "Angiogenic potential of microvessel fragments established in three-dimensional collagen gels," In vitro Cell Develop Biol Anim 32:409-19.

[26] Bottenstein, J.E. and Sato, G.H.. (1979) "Growth of a rat neuroblastoma cell line in serum-free supplemented medium," Proceed Nat Acad Sci USA 76:514-7.

[27] Maas, S.A. (2007-2011) WinFiber3D. Musculoskeletal Research Laboratories, University of Utah. (http://mrl.sci.utah.edu/software/winfiber3d).

[28] Kirkpatrick, N.D., Andreou, S., Hoying, J.B., and Utzinger, U. (2007) "Live imaging of collagen remodeling during angiogenesis," Am J Physiol Heart Circ Physiol 292:H3198-206.

[29] Bowen, R.M. (1976) "Theory of mixtures," New York: Academic Press.

[30] Ateshian, G.A., Rajan, V., Chahine, N.O., Canal, C.E., and Hung, C.T. (2009) "Modeling the matrix of articular cartilage using a continuous fiber angular distribution predicts many observed phenomena," J Biomech Eng 131:061003.

[31] Roeder, B.A., Kokini, K., and Voytik-Harbin, S.L. (2009) "Fibril microstructure affects strain transmission within collagen extracellular matrices," J Biomech Engng 131:031004.

[32] Krishnan, L., Weiss, J.A., Wessman, M.D., and Hoying, J.B. (2004) "Design and application of a test system for viscoelastic characterization of collagen gels," Tiss Engng. 10:241-52.

[33] Richter, S.J. and Richter, C. (2012) "A method for determining equivalence in

industrial applications," Quality Engng. 14:375-80.

[34] van Nieuw Amerongen, G.P., Koolwijk, P., Versteilen, A., and van Hinsbergh, V.W. (2004) "Involvement of RhoA/Rho kinase signaling in VEGF-induced endothelial cell migration and angiogenesis in vitro," Arterioscler Thromb Vasc Biol 23:211-7.

[35] Yang, M.T., Reich, D.H., and Chen, C.S. (2011) "Measurement and analysis of traction force dynamics in response to vasoactive agonists," Integ Biol. 3:663-74.

[36] Ateshian, G.A. and Humphrey, J.D. (2012) "Continuum mixture models of biological growth and remodeling: Past successes and future opportunities," Ann Rev Biomed Engng 14:97-111.

[37] Barocas, V.H., Moon, A.G., and Tranquillo, R.T. (1995) "The fibroblast-populated collagen microsphere assay of cell traction force--Part 2: Measurement of the cell traction parameter," J Biomech Engng 117:161-70.

[38] Barocas, V.H. and Tranquillo, R.T. (1997) "An anisotropic biphasic theory of tissue-equivalent mechanics: The interplay among cell traction, fibrillar network deformation, fibril alignment and cell contact guidance," J Biomech Engng 119:137-45.

[39] Rausch, M.K., Dam, A., Goktepe, S., Abilez, O.J., and Kuhl, E. (2011) "Computational modeling of growth: Systemic and pulmonary hypertension in the heart," Biomech Model Mechanobiol 10:799-811.

[40] van Oers, R.F., Rens, E.G., LaValley, D.J., Reinhart-King, C.A., and Merks, R.M. (2014) "Mechanical cell-matrix feedback explains pairwise and collective endothelial cell behavior in vitro," PLoS Comp Biol 10:e1003774.

[41] Peirce, S.M. (2008) "Computational and mathematical modeling of angiogenesis," Microcirc 15:739-51.

[42] Qutub, A.A., Mac Gabhann, F., Karagiannis, E.D., Vempati, P., and Popel, AS. (2009) "Multiscale models of angiogenesis," IEEE Engng Med Biology 28:14-31.

[43] Ateshian, G.A., Maas, S., and Weiss, J.A. (2013) "Multiphasic finite element framework for modeling hydrated mixtures with multiple neutral and charged solutes," J Biomech Engng. 135:111001.

[44] Ateshian, G.A., Nims, R.J., Maas, S., and Weiss, J.A. (2014) "Computational modeling of chemical reactions and interstitial growth and remodeling involving

charged solutes and solid-bound molecules," Biomech Model Mechanobiol 13:1105-20.

CHAPTER 6

DISCUSSION

6.1 Summary

The objective of the research presented in this dissertation was to design, implement, and validate a computational framework that simulates the dynamic mechanical interaction between angiogenic neovessels and the ECM. To accomplish these goals, a novel continuous-discrete FE model with angiogenic growth coupled with matrix deformation was proposed. During angiogenesis, the geometry and structure of the emerging vascular network is regulated by the structure and composition of the ECM [1-21]. Chapters 3 and 4 described the vascular growth model that was used to simulate these phenomena and provide geometry to the FE model using properties of the ECM [20,21]. The important aspects of vascular geometry predicted by the growth model are the position and orientation of the sprout tips, which were used to calculate the sprout force representations applied to the mesh in Chapter 5 [19]. The implementation of the proposed framework was completed in Chapter 5 by coupling the vascular growth model to the nonlinear finite element software FEBio [22]. FEBio was called to solve for the deformation induced by the sprout force representations calculated using the vascular geometry data predicted by the growth model. Vascular

geometry was also required when calculating the microvessels-to-ECM volume fraction for the composite material model used by FEBio. The deformation determined by FEBio was then used to update the mesh representing the ECM, including fibril orientation and density values prescribed at the nodes, and the microvessel population into the current configuration.

Data from vascularized gel experiments were used to both calibrate mechanisms within the model during implementation and compare with computational simulations to assess the validity of the simulations. In Chapter 3, experimental data from unconstrained vascularized gels was used to calculate the length and branching functions used to calculate neovessel growth and branching rate, respectively. Data from these cultures were also used to optimize values for parameters within the growth model including the branching probability and the weight factors for the various directional cues. Finally, the ability of the model to predict vascular alignment in an aligned collagen fibril field was demonstrated by running simulations using fibril information obtained from constrained vascularized gels using confocal reflective microscopy. In Chapter 4, total vascular length data from microvessel cultures performed at different levels of matrix density were used to fit the scaling factor function. This scaling factor was used to scale neovessel growth and branch rate within the growth model relative to local matrix density. The validity of this updated framework was confirmed by comparing various morphometric data from the vascularized gel experiments to predictions from the computational model. In Chapter 5, experimental data were used to prescribe values for the sprout force parameters and constitutive model. Validity of the coupled growth model was demonstrated in

simulations of growth within a long-axis constrained gel, which accurately predicted gel contraction and aligned vasculature as was seen in the experiments.

6.2 Matrix Remodeling and the Mechanical Regulation of Angiogenesis

During sprouting angiogenesis, VEGF signaling causes endothelial cells in parent vessels to adopt the angiogenic phenotype, form sprouts, apply traction along components of the ECM, and extend into to matrix. VEGF signaling at the cell surface leads to increased stress fibers and focal adhesions within endothelial cells, mediated through the receptor VEGFR2 and activity of Rho and ROCK (Rho-Kinase) [23-25]. This increase in contractile activity, in combination with proteolytic MMPs, extensively deforms and remodels the matrix during growth. Neovessels use this traction to pull ECM fibrils towards the sprout, expunging water from between the fibrils and condensing the matrix. Neovessel sprouts also create new cell-matrix adhesions, remodeling the ECM structure and increasing the stiffness the vascularized constructs. Imposing a boundary constraint during these cultures prevents the gels from contracting along the constrained direction. Neovessels displace with the deformation of the matrix, causing them align along the directions of greatest effective stiffness (i.e., less contraction) and perpendicular to the directions of least stiffness (i.e., more contraction). In the LAC experiments, the matrix was constrained along the long-axis (high stiffness) and had low effective stiffness along the other two directions due to the narrow aspect ratio of the gel, causing microvessels to become aligned along the long-axis. However, in the SAC experiments, both the short- and long-axes had high

effective stiffness due to the imposed boundary constraint and gel geometry, respectively. As a result, microvessels did not significantly align with respect to either of these axes. The computational model of angiogenesis in which angiogenic growth was coupled to the matrix deformation using the FE method demonstrated the mechanism behind this alignment. In simulations of a LAC gel using this model, alignment developed as the mesh deformed anisotropically under cell-generated loading. Microvessels were updated by interpolating mesh displacement to the vessels, causing vessels to convect with the deformation of the mesh and align according to this deformation.

The effective stiffness of the matrix and its effect on the ability of cells to deform the matrix regulate angiogenesis in more ways than just determining vascular alignment. There is substantial evidence demonstrating that the angiogenic phenotype within endothelial cells is promoted by ECM deformation and remodeling. Reduced neovessel outgrowth and branching has been observed as the effective stiffness of the matrix was increased, either by imposing boundary constraints or increasing the density of the matrix. Numerous studies utilizing other various models of angiogenesis have found a reduction in angiogenic outgrowth and branching when increasing the effective stiffness of the matrix [1,6,7,12]. Additionally, sensitivity analysis using the FE model of angiogenesis suggest that the range of cell-generated traction during growth as the most important parameter controlling the deformation of the matrix and therefore angiogenic growth and remodeling. Analyses of these studies suggest two priority targets for utilizing the mechanical regulation of angiogenesis to influence growth: the structure and composition of the ECM, and the traction forces applied by neovessel

sprouts. The structure and composition, including boundary conditions, determine the stiffness of the matrix and how cell-generated forces transmit through and deform the fibrillar structure. Local matrix deformation is an important promoter of angiogenic growth at the microscale, and the structure/composition of the matrix can also act on the macroscale to determine vascular alignment in the case of the constrained gel experiments. The other potential way to regulate angiogenesis through the mechanics of growth is to change the way cells remodel the matrix, including their ability to generate force and apply traction, synthesize and release MMPs, and generate new cell-matrix adhesions. Promoting these cellular behaviors promotes matrix remodeling and growth, while inhibiting these activates growth.

6.3 Live Two-Photon Imaging of Angiogenic Neovessels

Although our modeling framework has proven useful in uncovering mechanical mechanisms for alignment during angiogenesis, nondeterministic mechanisms were used to simulate branching and anastomosis within our modeling framework and details into the mechanical mechanisms behind these angiogenic behaviors remain unclear. It is difficult to gain significant insight into the mechanical regulation of this dynamic process using traditional experimental techniques. However, new methodology for live 2P imaging provides the opportunity for live visualization of angiogenic neovessels on a gigavoxel scale using two-photon (2P) four-dimensional (4D, 3D space and time) microscopy [26]. Live 2P imaging provides insight into the dynamics of angiogenesis by allowing direct observation of neovessel sprouting, elongation and anastomosis in real time. 2P microscopy allows researchers to capture the large spatial scale over

which angiogenic network formation occurs while maintaining the viability of exposed angiogenic microvessels over the long time period required. Additionally, the utilization of second-harmonic generation (SHG) allows 4D imaging of the collagen matrix structure during angiogenesis as well, providing valuable information about how the matrix is deformed and remodeled during growth.

Microvessel fragments were obtained from rats expressing green fluorescent protein (GFP) and cultured in a type-I collagen gel. After 48 hours, cultures were moved into an incubation chamber assembled on the stage of a 2P microscope. Perfusion tubes allowed for daily media flushing and removal. The circular gel was circumferentially constrained by a stainless steel mesh to keep the gel from floating away during culture. A 2.0 × 2.0 × 0.9 mm domain at the center of the gel was imaged using mosaicking every 2 hours. Autofluorescence signal from GFP was collected to image the cellular portion of the constructs and SHG data were collected to provide information about the collagen matrix. Since there is no way of predicting the location of spontaneous sprout formation and vessel anastomosis, a large spatial domain had to be imaged. As a result, the 4D dataset for a single experiment was extremely large, consisting of several gigavoxels of volumetric data at each of the 60 time points. After processing, the 4D volumetric-temporal dataset was visualized using a workstation with a graphics processing unit (GPU) and the software FluoRender [27].

Live imaging of angiogenic neovessels demonstrated that the ECM is extensively deformed and remodeled during growth. SHG data from the 4D datasets reveal that mature neovessels are surrounded in a condensed layer of collagen (Figure 6.1). Additionally, collagen was condensed at the sprout tips as tip cells apply traction to the

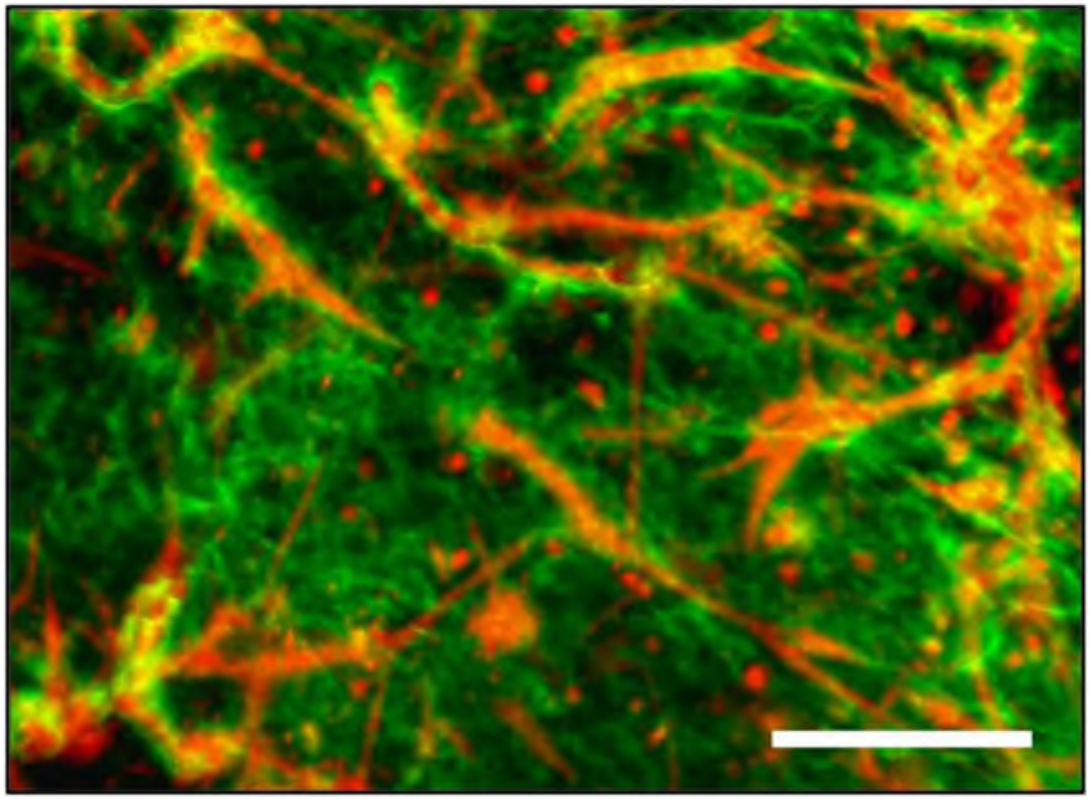

Figure 6.1: Live imaging of angiogenic neovessels and the extracellular matrix using two-photon microscopy. Vessels were imaged using autofluorescence from green-fluorescent protein, shown in red. The collagen matrix was imaged using second-harmonic generation, shown in green. Live imaging has revealed that collagen is condensed into a layer surrounding the angiogenic microvessels, as demonstrated by the high intensity of SHG signal localized around the vessels. Scale bar 100 μm.

Additionally, collagen was condensed at the sprout tips as tip cells apply traction to the matrix (Figure 6.2). The live 2P imaging also allowed researchers to observe many interesting neovessel behaviors that could not be seen in the previous static culture experiments. Neovessel growth in these experiments was episodic, meaning neovessels spontaneously switch between elongation and regression behavior (Figure 6.3 A-C). Elongation typically occurred at a slower rate than regression and usually involved several filpodia within the sprout tip sampling the ECM and probing in multiple directions. It was common to see neovessels regress by up to 100 μm within a few hours, and this regression was usually followed by elongation along a new direction (Figure 6.3 D). Nearby neovessel sprouts also seemed to be able to locate one another, leading to an anastomosis event and the expansion of the vascular network (Figure 6.3 E, F). Each of these neovessel behaviors is accompanied by condensation and remodeling of the ECM structure, as seen in the SHG channel. Although still early in development, these live imaging techniques will allow researchers to gain further insight into the deterministic mechanisms that cause episodic growth, regression and direction change, and local neovessel location in angiogenic neovessels interacting with the ECM.

6.4 Limitations and Future Work

Although the computational framework met the objectives of each study in this dissertation, there are some limitations that should be addressed. The growth model represented neovessels as a collection of end-to-end line segments of the same width (diameter). Neovessels in these organ cultures are much thinner than parent vessel

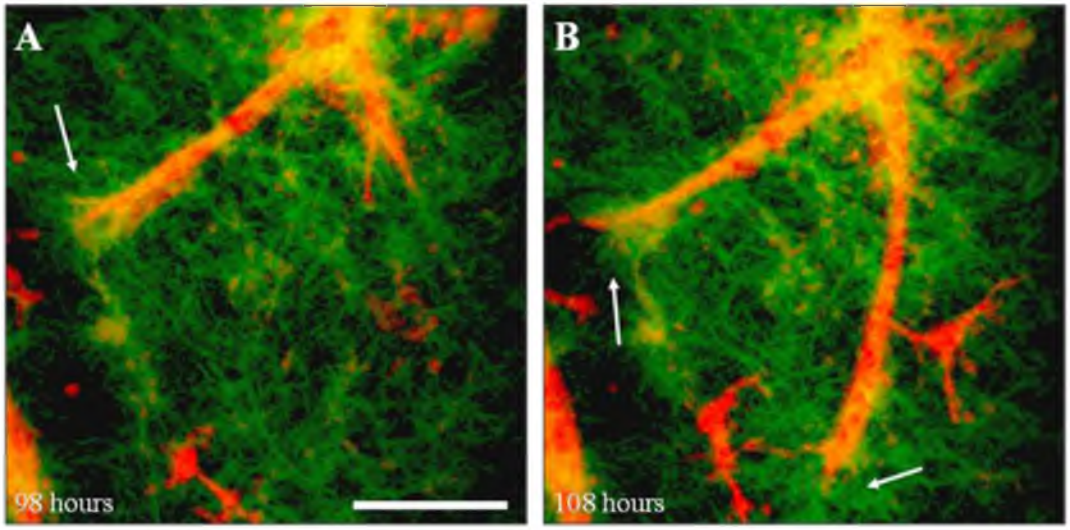

Figure 6.2: Traction applied by neovessel sprouts remodels and condenses collagen during growth. This figure shows two-photon imaging of two neovessel sprouts, indicated by the white arrows, at culture times 98 hours (A) and 108 hours (B). Neovessels are imaged via autofluorescence, shown in red, the collagen matrix is imaged via second harmonic generation and is shown in green. Collagen becomes condensed at the sprouts as neovessels apply traction and deform the matrix, as indicated by the higher collagen signal around the sprouts as time increases. Additionally, this figure demonstrates how most sprouts tend to utilize multiple filapodia tips, but only elongate along a single direction. Scale bar 25 μm.

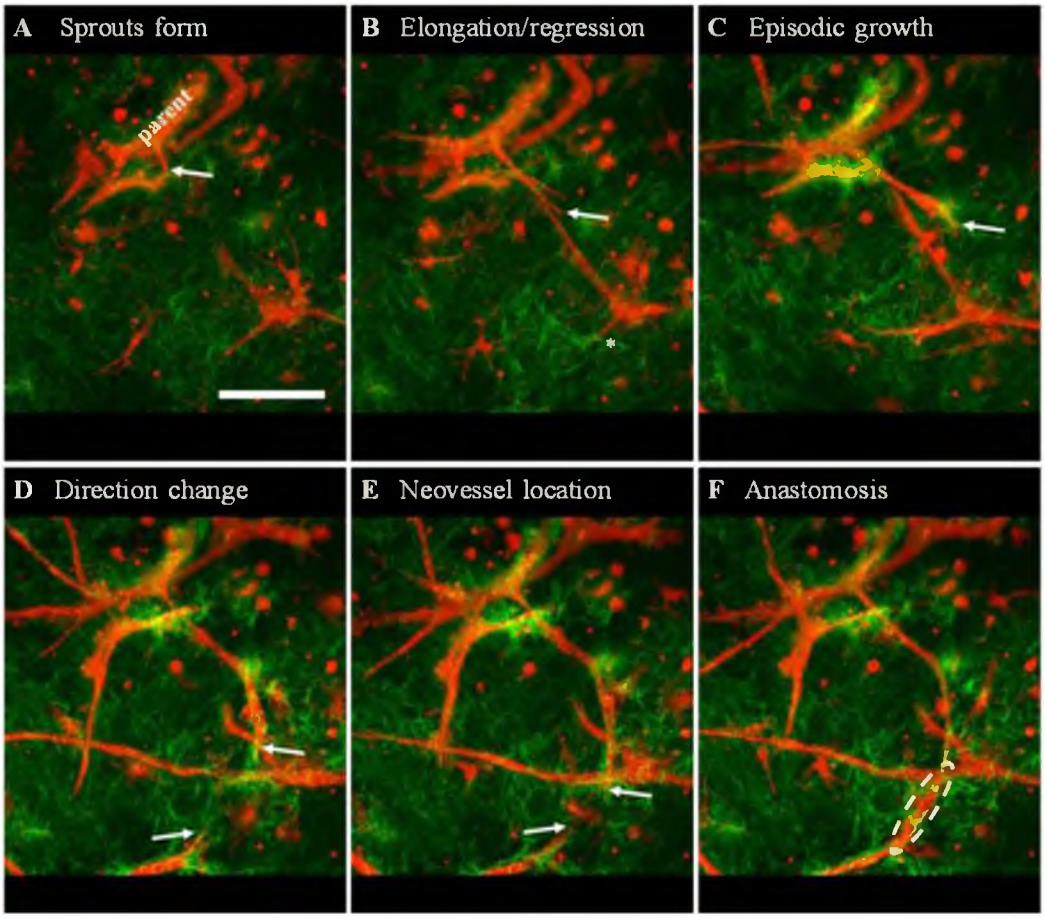

Figure 6.3: Live two-photon imagine reveals neovessel behavior that would be difficult to investigate using traditional static culture experiments. Neovessels imaged using autofluorescence are shown in red, collagen matrix imaged using second-harmonic generation is shown in green. (A) This figure tracks the behavior of a particular neovessel sprout, indicated by the white arrow. The sprout begins by branching off of a parent vessel fragment. (B) The sprout elongates and extends into the matrix, its new position indicated by the arrow. However, sprouts also exhibit regression during which the neovessel collapses backwards towards the original sprouting location. A regressed sprout can be seen in this image, indicated by the asterisk. The sprout can be view in the previous image prior to the regression (A). (C) Sprouts exhibited both elongation and regression, and this spontaneous switching between elongation and regression caused episodic neovessel growth. In this image, the sprout has regressed back and is beginning to elongate in a new direction. (D) Regression event were usually followed by elongation along a new direction, causing the neovessel to change its direction. In this image, a second neovessel sprout appears, indicated by the second white arrow (point to the right). (E, F) Nearby neovessel sprouts seemed able to locate one another, leading to an anastomosis event indicated by the white dashed outline (F). Each of these neovessel behaviors is accompanied by condensation and remodeling of the ECM structure as seen in the second-harmonic generation data. Scale bar 50 μm.

fragments [28], and future development of the model should include this heterogeneous vascular diameter and geometry. Additionally, the growth model included non-deterministic mechanisms to determine branching and anastomosis and should eventually be replaced with deterministic mechanisms. Although the model was able to predict strain and stress within the vascularized constructs, we did not explicitly calculate strain and stress across the neovessel surface, which may be responsible for the mechanisms determined the direction of neovessel growth and the formation of new sprouts during branching. To improve the spatial resolution across the neovessel surfaces to facilitate such calculations, the coupled growth model could be moved from a continuous-discrete representation to a fully continuous model. Instead of using line segments to represent neovessels, in this representation neovessels are represented by elements within the mesh that are assigned a "neovessel" material model while other elements in the mesh are assigned an "ECM" material model. Initial vascular geometry can be obtained from volumetric data from 2P imaging, and growth is represented by converting ECM elements to neovessel elements. Sprout forces can be applied at the locations where filapodia attach to the ECM and the resulting deformation can be obtained using FEBio. Using this framework, we could effectively calculate strain and stress along the neovessel surface and modeling the mechanotransduction and cellular signaling that occurs as a result. Additionally, the implementation of multiphase framework in FEBio will allow for the simulation of transport and reaction kinetics of both soluble and matrix-bound growth factors such as VEGF [29]. This new framework would allow us to calculate the concentration of VEGF and other growth factors along the neovessel surface and would allow the inclusion of additionally signaling factors

within our simulations.

6.5 Conclusions

Morphogenic processes such as angiogenesis are complex, path-dependent phenomena in which the emerging morphology is determined by feedback received by cells from the surrounding environment. This feedback depends on the temporal and spatial distribution of chemical and mechanical properties within the ECM. As morphogenesis progresses, the participating cells remodel their environment and change these regulatory properties. Simulating these processes requires a temporal and spatial representation of regulatory properties as well as a method for updating these properties based on cellular activity. In this dissertation, the regulatory properties that determine angiogenesis included ECM fibril orientation and density, and these properties were updated throughout time using kinematics produced by cell-generated traction calculated using FE method. The framework presented here was capable at simulating experiments using vascularized collagen gels and can be expanded to predict experiments that are difficult or impossible to perform using current techniques. These methods can be expanded to simulate numerous morphogenic processes in such individual cellular agents are regulated by temporal and spatial properties of the ECM such as neurogenesis, lung morphogenesis, and cancerous tumor formation.

6.6 References

[1] Sieminski, A.L., Hebbel, R.P. and Gooch, K.J. (2004) "The relative magnitudes of endothelial force generation and matrix stiffness modulate capillary morphogenesis in vitro," Ex Cell Research 297:574-84.

[2] Nicosia, R.F., Zhu, W.H., Fogel, E., Howson, K.M. and Aplin, A.C. (2005) "A new ex vivo model to study venous angiogenesis and arterio-venous anastomosis formation," J Vasc Res 42:111-9.

[3] Yamamura, N., Sudo, R., Ikeda, M. and Tanishita, K. (2007) "Effects of the mechanical properties of collagen gel on the in vitro formation of microvessel networks by endothelial cells," Tissue Engng 13:1443-53.

[4] Krishnan, L., Hoying, J.B., Nguyen, H., Song, H. and Weiss, J.A. (2007) "Interaction of angiogenic microvessels with the extracellular matrix," Am J Phys: Heart Circ Phys 293:H3650-8.

[5] Krishnan, L., Underwood, C.J., Maas, S., Ellis, B.J., Kode, T.C., Hoying, J.B. and Weiss, J.A. (2008) "Effect of mechanical boundary conditions on orientation of angiogenic microvessels," Cardiovasc Res 78:324-32.

[6] Califano, J.P. and Reinhart-King, C.A. (2008) "A balance of substrate mechanics and matrix chemistry regulates endothelial cell network assembly," Cell Mol Bioeng 1:122-132.

[7] Kniazeva, E. and Putnam, A.J. (2009) "Endothelial cell traction and ECM density influence both capillary morphogenesis and maintenance in 3-D," Am J Phys: Cell Phys 297:C179-87.

[8] Kniazeva, E., Kachgal, S. and Putnam, A.J. (2011) "Effects of extracellular matrix density and mesenchymal stem cells on neovascularization in vivo," Tissue Engng Part A 17:905-14.

[9] Vong, S. and Kalluri, R. (2011) "The role of stromal myofibroblast and extracellular matrix in tumor angiogenesis," Genes Cancer 2:1139-45.

[10] Chang, C.C., Krishnan, L., Nunes, S.S., Church, K.H., Edgar, L.T., Boland, E.D., Weiss, J.A., Williams, S.K. and Hoying, J.B. (2012) "Determinants of microvascular network topologies in implanted neovasculatures," Arterioscler Thromb Vasc Biol 32:5-14.

[11] Hielscher, A.C. and Gerecht, S. (2012) "Engineering approaches for investigating tumor angiogenesis: Exploiting the role of the extracellular matrix," Cancer Res 72:6089-96.

[12] Rao, R.R., Peterson, A.W., Ceccarelli, J., Putnam, A.J. and Stegemann, J.P. (2012) "Matrix composition regulates three-dimensional network formation by endothelial cells and mesenchymal stem cells in collagen/fibrin materials," Angiogenesis 15:253-264.

[13] Underwood, C.J., Edgar, L.T., Hoying, J.B. and Weiss, J.A. (2013) "Cell-generated forces and the resulting matrix deformation cause microvascular alignment in vascularized collagen gels", Am J Physiol Heart Circ Physiol, 307: H152-64.

[14] Mason, B.N. and Reinhart-King, C.A. (2013) "Controlling the mechanical properties of three-dimensional matrices via non-enzymatic collagen glycation," Organogenesis 9:70-5.

[15] Feng, X., Tonnesen, M.G., Mousa, S.A. and Clark, R.A. (2013) "Fibrin and collagen differentially but synergistically regulate sprout angiogenesis of human dermal microvascular endothelial cells in 3-dimensional matrix," Int J Cell Biol 2013:231279.

[16] Chen, P., Cescon, M. and Bonaldo, P. (2013) "Collagen VI in cancer and its biological mechanisms," Trends Mol Med 19:410-7.

[17] Mettouchi, A. (2012) "The role of extracellular matrix in vascular branching morphogenesis," Cell Adh Migr 6:528-34.

[18] Wietecha, M.S., Cerny, W.L. and DiPietro, L.A. (2013) "Mechanisms of vessel regression: Toward an understanding of the resolution of angiogenesis," Curr Top Microbiol Immunol 367:3-32.

[19] Edgar, L.T., Maas, S.A., Guilkey, J.E. and Weiss, J.A. (2013) "A continuous-discrete finite element model of sprouting angiogenesis that couples neovessel growth with matrix deformation," Biomech Model Mechanobiol, in press.

[20] Edgar, L.T., Sibole, S.C., Underwood, C.J., Guilkey, J.E. and Weiss, J.A. (2013) "A computational model of in vitro angiogenesis based on extracellular matrix fibre orientation," Comp Meth Biomech Biomed Engng 16:790-801.

[21] Edgar, L.T., Underwood, C.J., Guilkey, J.E., Hoying, J.B. and Weiss, J.A. (2013) "Extracellular matrix density regulates the rate of neovessel growth and branching in sprouting angiogenesis," PLoS One 9.

[22] Maas, S.A., Ellis, B.J., Ateshian, G.A. and Weiss, J.A. (2012) "FEBio: Finite elements for biomechanics," J Biomech Eng 134:011005.

[23] Huot, J., Houle, F., Rousseau, S., Deschesnes, R.G., Shah, G.M. and Landry, J. (1998) "SAPK2/p38-dependent F-actin reorganization regulates early membrane blebbing during stress-induced apoptosis," J Cell Biol 143:1361-73.

[24] van Nieuw Amerongen, G.P., Koolwijk, P., Versteilen, A. and van Hinsbergh, V.W. (2003) "Involvement of RhoA/Rho kinase signaling in VEGF-induced

endothelial cell migration and angiogenesis in vitro," Arterioscler Thromb Vasc Biol 23:211-7.

[25] Yang, M.T., Reich, D.H. and Chen, C.S. (2011) "Measurement and analysis of traction force dynamics in response to vasoactive agonists," Integr Biol (Camb) 3:663-74.

[26] Utzinger, U., Baggett, B., Weiss, J.A., Hoying, J.B. and Edgar, L.T. (2013) "Large-scale time series microscopy of neovessel growth during angiogenesis," Angiogenesis, in press.

[27] FluoRender: An interactive rendering tool for confocal microscopy data visualization. Scientific Computing and Imaging Institute (SCI). University of Utah, S.L.C., UT, USA. http://www.fluorender.org

[28] Hoying, J.B., Boswell, C.A. and Williams, S.K. (1996) "Angiogenic potential of microvessel fragments established in three-dimensional collagen gels," In Vitro Cell Developal Biol: Anim 32:409-19.

[29] Ateshian, G.A., Nims, R.J., Maas, S.A. and Weiss, J.A. (2013) "Modeling chemical reactions, interstitial growth and remodeling in a finite element framework for biological tissues," Biomech Model Mechanobiol, in press.